POLITECNICO DI MILANO

Facoltà di Ingegneria Industriale e dell'Informazione

Dipartimento di Energia

Dipartimento di Chimica, Materiali e Ingegneria Chimica

"Giulio Natta"

A MULTIREGION OPERATOR-SPLITTING APPROACH FOR COUPLING CFD AND DUSTY GAS MODEL IN HETEROGENEOUS CATALYTIC REACTORS

Relatori: Prof. Matteo MAESTRI

Prof. Alberto CUOCI

Tesi di Laurea in Ing. Chimica di:

Matteo MARSIGLIA Matr. 813526

Gioele TAGLIABUE Matr. 819021

Anno Accademico 2014 - 2015

Abstract

In this thesis work the coupling between the dusty gas diffusion model and computational fluid dynamics for the numerical solution of problems involving mass transport with chemical reaction in catalytic porous media is presented. Using a different model with respect to the Fick model grants the possibility to account for intraporous pressure gradients due to chemical reactions or different diffusion velocities of the species involved, thus resulting in an innovative approach. This aspect is particularly useful on industrial scale as the diffusion lengths in industrial catalysts are much longer than in laboratory catalysts. In fact, pressure variations can boost reaction rates but, on the contrary, cause structural damage on the porous matrix itself. A detailed analysis of the physical foundations of the model is presented and comparisons with the Fick formulation in cases with different stoichiometry and kinetic rates are carried out to highlight the differences in the estimation of catalyst efficiency, mole fractions and pressure inside the solid matrix. The dusty gas model was then implemented in catalyticFOAM, a computation fluid dynamics code for modeling multidimensional, catalytic, reacting systems. The code had never been tested with a diffusion model different from the Fickian formulation. The convergence routine between fluid and solid phase, named PIMPLE loop, has been modified to account for pressure convergence at the interphase surface. In conclusion, this extended version of catalyticFOAM has been tested in simulations of heterogeneous, catalytic reactions.

Sommario

In questo lavoro di tesi viene presentato l'accoppiamento del modello di diffusione dusty gas con la fluidodinamica computazionale per risolvere numericamente problemi di trasporto accoppiato a reazione chimica all'interno di strutture solide catalitiche porose. L'utilizzo di un modello differente da quello di Fick risulta innovativo per la possibilità di modellare la generazione di gradienti di pressione interni al solido, sia dovuti alle stechiometrie di reazione sia dovuti a differenti velocità di diffusione delle specie presenti. L'importanza risulta evidente su scala industriale, a causa delle maggiori lunghezze diffusive dovute alle maggiori grandezze che le particelle di catalizzatore hanno rispetto a casi di laboratorio. Variazioni di pressione possono, infatti, avere notevoli effetti sulle cinetiche di reazione, nonché effetti dannosi per le strutture porose dei catalizzatori stessi. Pertanto, viene presentata un'analisi dettagliata dei fondamenti fisici del modello ed i risultati dei differenti modelli diffusivi, in casi con differente stechiometria e velocità di reazione, vengono messi a confronto con lo scopo di sottolineare le differenze nelle stime dei parametri di efficienza, nei profili di frazione molare e di pressione internamente alla matrice solida. Il modello dusty gas è stato infine implementato in catalyticFOAM, un codice di fluidodinamica computazionale per la simulazione di sistemi catalitici reattivi multidimensionali. Il codice non era mai stato testato prima d'ora con un modello di diffusione differente rispetto a quello di Fick. Il metodo di convergenza tra fase fluida e solida, denominato ciclo PIMPLE, è stato opportunamente modificato per portare a convergenza anche la pressione all'interfaccia tra fase fluida e solida. In conclusione, catalyticFOAM così esteso è stato testato in simulazioni di reazioni catalitiche eterogenee.

Contents

List of Figures

List of Tables

List of Symbols

Greek Symbols

Symbol	Description	Dimensions	Units
ϵ	porosity	–	1
η	catalyst efficiency	–	1
$\hat{\phi}_i$	mixture fugacity coefficient of i^{th} species	–	1
τ	shear stress	L^2T^{-2}	$\mathrm{N\,m\,kg^{-1}}$
μ	dynamic viscosity	$ML^{-1}T^{-1}$	$\mathrm{Pa\,s}$
μ_i	chemical potential of i^{th} species	$ML^2T^{-2}N^{-1}$	$\mathrm{J\,mol^{-1}}$
∇	gradient	L^{-1}	$\mathrm{m^{-1}}$
ω_i	mass fraction of i^{th} species	–	1
ρ_i	density of i^{th} species	ML^{-3}	$\mathrm{kg\,m^{-3}}$
τ	tortuosity	–	1

Roman Symbols

Symbol	Description	Dimensions	Units
$\mathbf{A}$	coefficient matrix of a linear system	–	–
$\mathbf{b}$	known terms vector of a linear system	–	–

B_0	permeability coefficient	L^2	m^2
c_i	concentration	NL^{-3}	$\mathrm{mol\,m^{-3}}$
c_i	concentration of ith species	NL^{-3}	$\mathrm{mol\,m^{-3}}$
$\mathbf{d_i}$	generalized driving force	L^{-1}	m^{-1}
$\mathcal{D}_i^e$	effective Fick diffusivity of ith species	$\mathrm{L}^2\mathrm{T}^{-1}$	$\mathrm{m^2\,s^{-1}}$
$\mathcal{D}_{i,m}^e$	mixture continuum diffusivity of ith species	$\mathrm{L}^2\mathrm{T}^{-1}$	$\mathrm{m^2\,s^{-1}}$
$\mathcal{D}_{i,K}^e$	effective Knudsen diffusivity of ith species	$\mathrm{L}^2\mathrm{T}^{-1}$	$\mathrm{m^2\,s^{-1}}$
$\mathcal{D}_{ij,MS}$	Maxwell-Stefan diffusivity	$\mathrm{L}^2\mathrm{T}^{-1}$	$\mathrm{m^2\,s^{-1}}$
$\mathbf{F}$	force	MLT^{-2}	N
$\widetilde{\mathbf{F}}_\mathbf{i}$	force acting per kg of ith species	MLT^{-2}	$\mathrm{N\,kg^{-1}}$
f_i	fugacity of ith species	$\mathrm{ML}^{-1}\mathrm{T}^{-2}$	Pa
$\hat{f}_i$	mixture fugacity of ith species	$\mathrm{ML}^{-1}\mathrm{T}^{-2}$	Pa
g_i	partial molar Gibbs free energy of ith species	$\mathrm{ML}^2\mathrm{T}^{-2}\mathrm{N}^{-1}$	$\mathrm{J\,mol^{-1}}$
g_i^{R}	residual partial molar Gibbs free energy of ith species	$\mathrm{ML}^2\mathrm{T}^{-2}\mathrm{N}^{-1}$	$\mathrm{J\,mol^{-1}}$
$\mathbf{J_i}$	Fick flux of ith species	$\mathrm{NL}^{-2}\mathrm{T}^{-1}$	$\mathrm{mol\,m^{-2}\,s^{-1}}$
$\mathbf{J_c}$	Correction factor for Fick flux	$\mathrm{NL}^{-2}\mathrm{T}^{-1}$	$\mathrm{mol\,m^{-2}\,s^{-1}}$
$\mathbf{J_{i,visc}}$	Darcy flux of ith species	$\mathrm{NL}^{-2}\mathrm{T}^{-1}$	$\mathrm{mol\,m^{-2}\,s^{-1}}$
M_i	molecular weight of ith species	MN^{-1}	$\mathrm{kg\,mol^{-1}}$
$\mathbf{N_i}$	molar flux of ith species	$\mathrm{NL}^{-2}\mathrm{T}^{-1}$	$\mathrm{mol\,m^{-2}\,s^{-1}}$
p	pressure	$\mathrm{ML}^{-1}\mathrm{T}^{-2}$	Pa

p_i	partial pressure	$\mathrm{ML^{-1}T^{-2}}$	Pa
R	universal gas constant	$\mathrm{ML^2T^{-2}N^{-1}}\theta^{-1}$	$\mathrm{J\,mol^{-1}\,K^{-1}}$
$R_{i,reac}$	reaction rate of ith species	$\mathrm{NL^{-3}T^{-1}}$	$\mathrm{mol\,m^{-3}\,s^{-1}}$
T	absolute temperature	θ	K
$\mathbf{u}$	molar average velocity	$\mathrm{LT^{-1}}$	$\mathrm{m\,s^{-1}}$
$\mathbf{u_i}$	molar average velocity of ith species	$\mathrm{LT^{-1}}$	$\mathrm{m\,s^{-1}}$
$\mathbf{v}$	mass average mixture velocity	$\mathrm{LT^{-1}}$	$\mathrm{m\,s^{-1}}$
$\widetilde{V}_i$	partial molar volume of ith species	$\mathrm{L^3N^{-1}}$	$\mathrm{m^3\,mol^{-1}}$
x_i	mole fraction of ith species	–	1
x, y, z	Cartesian axes	L	m

Chapter 1

Introduction

1.1 Motivation

Catalysis is an important aspect of Chemical Engineering due to its practical effects on the industrial scale. The discovery of an appropriate catalyst for an industrial process grants enourmous benefits in terms of enhanced production and income growth.

A catalytic process involves many physical and chemical steps occurring in a broad range of time and length scales, as shown in Figure (1.1.1) [21]. These steps deal with both transport and reaction phenomena and can be summarized as

1. *film diffusion*: the reactants diffuse from the bulk phase to the boundary layer surrounding the solid phase

2. *pore diffusion*: the reactants diffuse from the boundary layer to the solid phase through the catalyst pores

3. *adsorption on active sites*: the reactants physically or chemically adsorb on the solid surface

4. *surface reaction*: the adsorbed species react between each other or with gas-phase species

5. *desorption from active sites*: the products desorb from the catalytic surface

6. *pores back-diffusion*: the products diffuse from inside the catalyst to the boundary layer around the solid

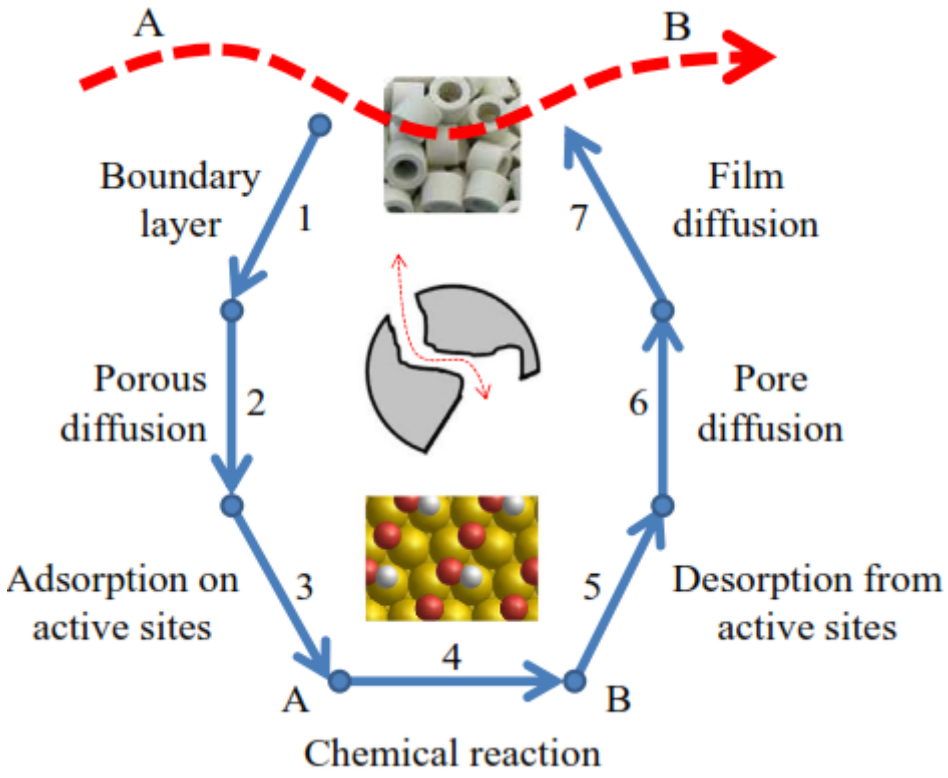

Figure 1.1.1: Main steps involved in a catalytic process

7. *film back-diffusion*: the products diffuse from the boundary layer to the bulk phase.

The simultaneous developments in catalysis and reaction engineering in 1930s and 1940s acted as a driving force for the onset of rational design of catalytic reactors. These rigorous design efforts, supported by firm mathematical principles, in turn triggered the development of several profitable catalytic processes. Several authors have studied the engineering aspects of diffusional mass transport and reaction rate interaction. In particular, Thiele [29] explained the fractional reductions in catalyst particle activity due to intraparticle mass transfer limitations and the concept of the effectiveness factor reflecting the extent of utilization of the catalyst pellet was proposed. His novel approach led to the dimensionless parameter known as the Thiele modulus, crucial for the computation of the effectiveness factor of a catalyst. Based on this concept, rigorous mathematical models developed in the 1950s and the 1960s showed the importance of intraparticle and interparticle diffusion. The advent of the computer era allowed the solution of complex mathematical models with reasonable effort so sophisticated

heterogeneous reactor models were proposed and solved. Today it is possible to study catalysis at the atomic level with detailed microkinetic models, analyze the interaction of surface chemistry with reacting fluids by the means of powerful computational fluid dynamics (CFD) tools and carry out performance assessment and enhancement. In particular, the latter has been receiving attention from industry and academia.

1.2 General overview

The dominant reaction mechanism is thus a multi-scale property of the system [19]. Three main scales, each governed by different equations according to the "first principles" approach, can be distinguished:

- *microscale*, which is associated with making and breaking of chemical bonds between atoms and molecules. At this scale the behavior of the system is described through detailed kinetic models whose parameters are computed via quantum chemistry electronic-structure calculations

- *mesoscale*, where the interplay between all the elementary steps involved in the catalytic process determines the main reaction pathway. At this scale statistical methods give a rigorous representation of mechanisms taking place at the catalytic surface but a common literature approach is the mean field approximation [27]. This approach assumes a perfect and rapid mixing of reactants, products and intermediates on the catalyst surface.

- *macroscale*, where the transport of mass, energy and momentum determines local composition, temperature and pressure. At this scale methods based on the resolution of Navier-Stokes equations via CFD techniques are used.

One of the main difficulties encountered in the numerical modeling of a catalytic system with complex kinetics and geometry is the aforementioned great difference of time and length involved, since the dominant reaction pathway is the result of the interplay between micro, meso and macro-scale phenomena, as shown in Figure (1.2.1).

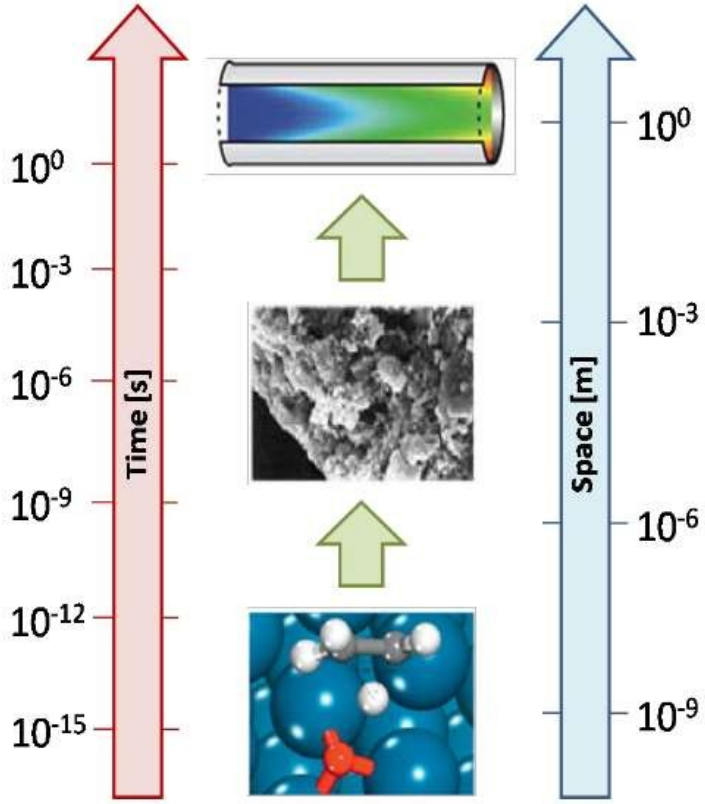

Figure 1.2.1: Time and length scales involved in heterogeneous catalytic processes

Such a fundamental approach implies the development of efficient methodologies to account for all the aspects across all the scales involved and link them in a single multi-scale simulation. Unluckily, the resulting numerical problem places highly computational demands as

- the dimensions of the system are proportional to the number of species involved in the reacting process so a more accurate kinetic scheme requires a higher computational effort
- the discretization of the geometric domain is required to solve the problem. The number of cells in which the volume is divided is proportional to the accuracy and to the dimensions of the problem
- the problem is very stiff because of the difference among the characteristic times of the scales
- the presence of a reacting term implies a strong non-linearity of the governing

equations.

An accurate description of the diffusion-reaction mechanism cannot be decoupled from a characterization of the catalytic phase and the modeling of intra-solid phenomena. This is mandatory especially when dealing with systems where the heat and mass transfer limitations play a major role in determining the conditions holding on the catalytic surface [20]. In these cases, neglecting the catalyst morphology can have a critical impact on the description of the system. Thus, understanding the gas transport is an important step to design more efficient catalytic system [24].

1.3 State of the art

Modeling transport with reaction in porous catalysts is a challenging task. For a precise description of diffusion occurring in pores, an extensive knowledge of the internal structure is required. Several approaches, with different degree of accuracy, are available in literature:

1. *pore-scale modelling*: a *detailed* approach [24] whose main goal is to represent the pore-scale geometry and topology of the real medium and to solve the pore-scale equations within the given domain. Conventional pore-scale models include Lattice-Boltzmann models, smoothed particle hydrodynamics approach, level-set models, percolation models, and pore-network models. The model equations are solved within a given microscopic domain representing pore-space morphology and the output is coupled with macroscopic models to reveal the impact of porous catalyst structure on the reactor performance. Reaction and transport are simulated in a reconstructed mesoporous particle on the nano-scale or in a section of macroporous layer on the micro-scale. The reconstruction of the porous structure is carried out by superposition of 2D images obtained from X-ray, transmission electron tomography or focused ion beam to a 3D virtual model (see Figure (1.3.1) [2]). Alternatively, the generation of the virtual image is carried out by the means of semi-deterministic methods such as simulated annealing and particle packing method. Once the 3D digital image or a porous structure is obtained, structural and

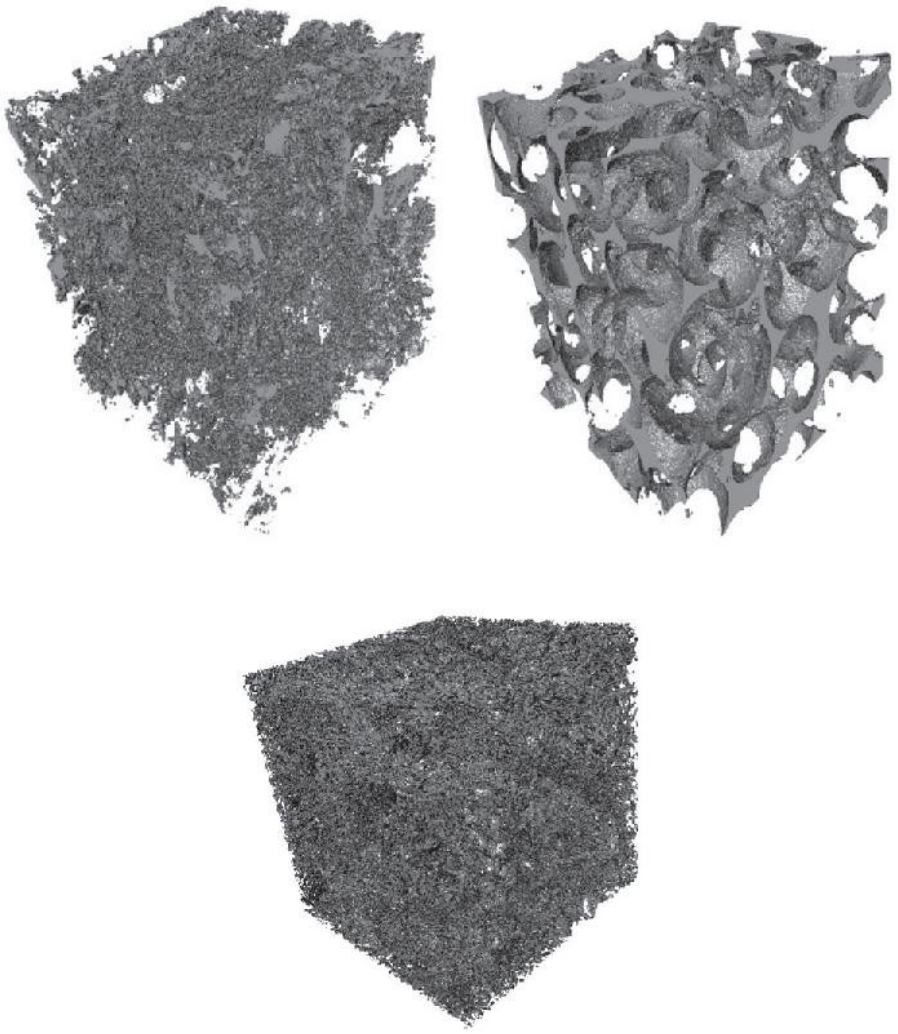

Figure 1.3.1: 3D images of pores obtained by X-Ray techniques

topological properties such as porosity and pore size distribution can be evaluated and the reaction-transport processes simulated. This approach is convenient to screen a virtual space of the structure parameters in order to identify key properties controlling diffusion limitations (macroporosity, mesoporosity, mesopore size *etc.*).

2. *Direct simulation Monte Carlo method*: this approach [9] is based on computational algorithms that rely on repeated random sampling to obtain numerical results. In particular, when used in the simulation of particle based models, the Direct simulation Monte Carlo approach simulates molecule collisions by the solution of the Boltzmann equation, which describes the statistical behaviour of a thermodynamic system not in thermodynamic equilibrium.

3. *DETCHEM*: the DETCHEM (DETailed CHEMistry) approach [14] is based on the coupling between catalytic surface reactivity and computational fluid dynamics. The potential of DETCHEM lies in the use of elementary step reaction mechanisms in modeling surface and/or gas-phase chemistry. The main drawback is the huge number of chemical species and reactions to account for, which makes the simulations a computational intensive task.

4. *classical approach*: this approach [1] proposes a corrected form of Fick's law

$$\mathbf{N_i} = -\frac{\epsilon}{\tau}\mathcal{D}_i \nabla c_i \tag{1.1}$$

combined with pore size distribution information to estimate the void fraction ϵ (usual values 0.3 - 0.8 [1]) and tortuosity τ (usual values 1 - 5 [24]) (an accurate description of the physical significance for each symbol herein used can be found in the **List of Symbols**). One of the pore size model used [1] is the random pore model [4] [33], useful for compressed particle type pellets. The pellet pore-size distribution is broken up into macro and micro values for the pore volume and average pore radius (often a pore radius of 100 Å is used as the dividing point). Based on random placement of the microparticles within the macropellet pores, a probabilistic argument is used to account for the supposed internal structure of the solid.

5. *dusty gas approach*: this approach is based on the Maxwell-Stefan law of diffusion [18] whose physical foundation is the exchange of momentum between gaseous particle and the solid matrix, considered as a "dummy" species. Due to this rigourous basis, the dusty gas model can account for a broader range of contributions to diffusion phenomena (i.e. external forces). Regarding the use of dusty gas model in heterogenous catalysis, the purpose of this work was to study the interaction between a dusty gas approach to mass transfer and computational fluid dynamics, which will be presented in the following.

1.4 Aim of the work

In previous works [12] [13], two CFD solvers (catalyticFOAM and catalyticFOAM multiRegion) have been built up in the OpenFOAM® framework, an open source CFD framework. The focus of this work was the development of the dusty gas model into catalyticFOAM to investigate the effect of intraporous pressure gradients due to non-equimolar chemical reactions on diffusion phenomena in catalytic, solid media.

In the following a short description of the structure of the present thesis is reported.

In **Chapter 2**, the theoretical background of the model is described. In particular the rigorous derivation from momentum balance, in contrast to the axiomatic nature of Fick law, is presented.

In **Chapter 3**, numerical simulations of unsteady diffusion with reaction problems are carried out according to Fickian approaches and a dusty gas approach to express molar fluxes. The effect of reaction stoichiometry, kinetics and diffusion coefficients for every model is investigated.

In **Chapter 4**, the catalyticFOAM framework is shortly presented. The operator-splitting algorithm, which proved to be successful [21] for an efficient coupling of CFD simulations with a microkinetic description of the surface reactivity, is discussed in detail. A C++ object oriented class implementing the dusty gas model and its interaction with catalyticFOAM are described. Furthermore, the pre-existing numerical routine for convergence at the interphase surface had to be changed to include pressure together with temperature and mass fractions.

In **Chapter 5**, a summary of the work and conclusions are presented.

Chapter 2

The theoretical foundations of the dusty gas model

In this chapter, the different models available for the description of diffusion phenomena inside catalytic porous particles are presented. In particular, the physical and mathematical foundations of the dusty gas model are discussed in detail.

2.1 General overview

Catalytic solid media play a fundamental role in heterogeneous, catalytic industrial processes (e.g. CH_3OH synthesis, CH_2O synthesis *etc.*). They consist of metal nanoparticles (*active phase*) distributed throughout a porous support, so the reactants have to diffuse through the layer to reach the active site where the reaction takes place. Although catalysts come in different forms (powders, pellets *etc.*), they all share a complex and irregular internal geometry noticeable when observed at the microscopic scale (see Figure (2.1.1)).

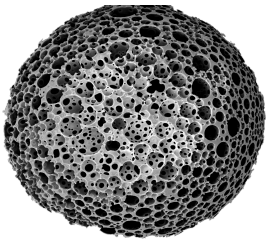

Figure 2.1.1: Internal structure of a catalytic porous particle

Due to this irregular structure, pore diameter is not constant, but follows a wide distribution. A sketch of a typical pore distribution [1] is given in Figure (2.1.2) Three main categories can be distinguished:

1. *micropores*, which have diameters smaller than 2 nm
2. *mesopores*, whose diameters are in the range between 2 nm and 50 nm
3. *macropores*, which have diameters greater than 50 nm.

Smaller pores possess high specific surface area so they can accomodate more active sites [7].

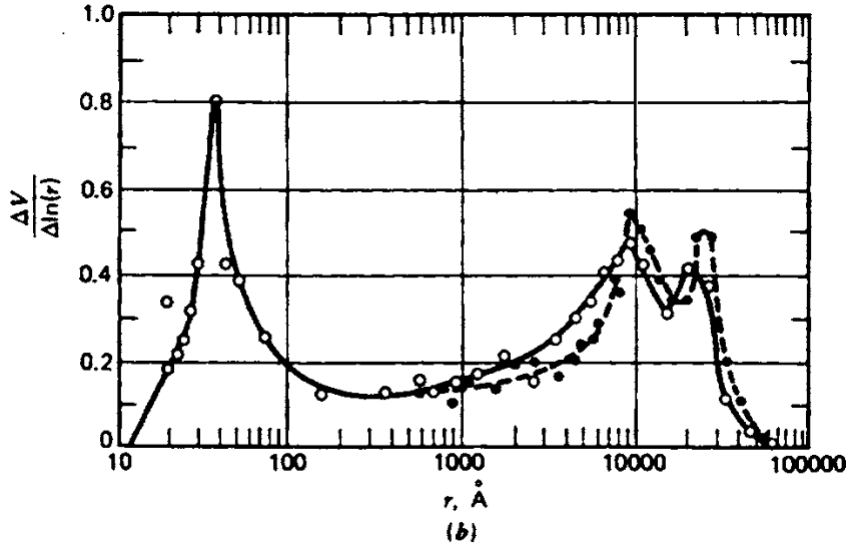

Figure 2.1.2: Example of a pore distribution in a catalyst. The picture shows clearly that the pore radius inside the solid matrix is not constant but falls in a wide range of possible values. Adapted from [1]

In heterogeneous reactors catalyst particles interact with reacting fluids. Two different approaches can be used for the description of this interaction (see Figure (2.1.3))

1. a *pseudo-homogeneous* approach, which neglects the description of the internal porous structure and considers the combination of fluid phase and solid phase as a unique pseudo-phase with uniform properties
2. a *heterogenous* approach, which explicitly accounts for two distinct phases, fluid and solid.

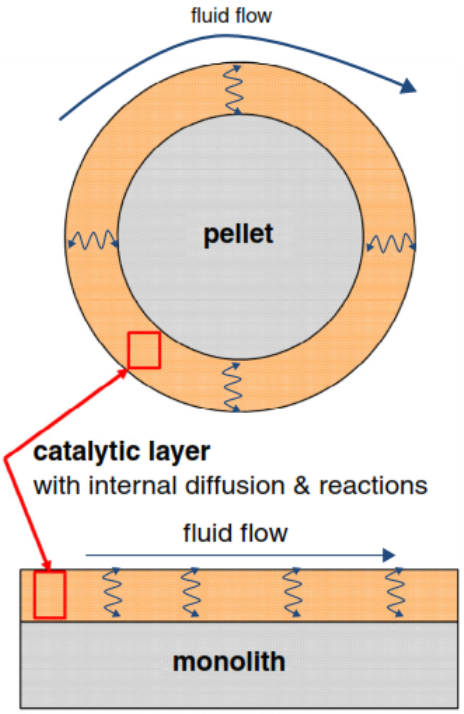

Figure 2.1.3: Interaction between reacting fluid and solid catalytic pellet. The reagents in the fluid flow diffuse in the catalytic layer while reacting and the reaction products counter-diffuse in the fluid phase. The interplay between fluid and catalytic solid phases is then strong

The pore size distribution strongly affects the dominant diffusion mechanism. In general, three fundamentally different types of diffusion mechanisms can be distinguished:

1. *bulk diffusion*, whose importance is relevant for macropores. The distinctive feature is that the pore diameter is much greater than the diffusion mean free path. An example is depicted in Figure (2.1.4) [32].

2. *Knudsen diffusion*, which becomes dominant when the diffusion mean free path is much larger than the pore diameter thus increasing the importance of the interaction between molecule and catalyst wall. It is important to notice that this mechanism is not negligible in industrial catalysts where the diffusion lengths are much longer than in laboratory catalysts. An example is depicted in Figure (2.1.5) [32].

3. *surface diffusion* of adsorbed species along the pore wall surface, whose

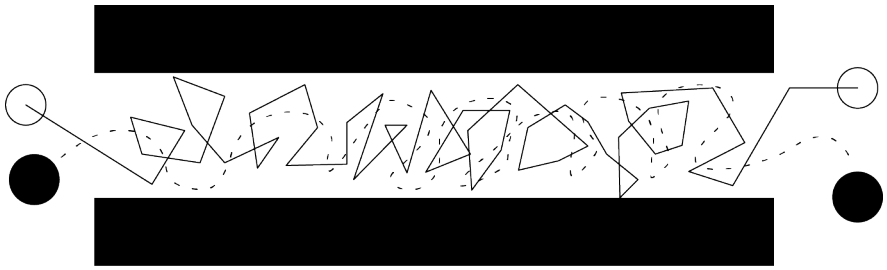

Figure 2.1.4: Sketch of bulk diffusion mechanism. The black bars represent the pore walls while the spheres are the species which diffuse inside the pore. The full and dashed lines represent the diffusion trajectories

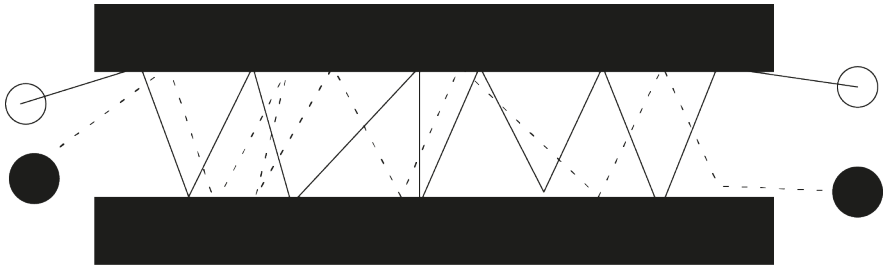

Figure 2.1.5: Sketch of Knudsen diffusion mechanism

importance is relevant for micropores and for strongly adsorbed species. An example is depicted in Figure (2.1.6) [32].

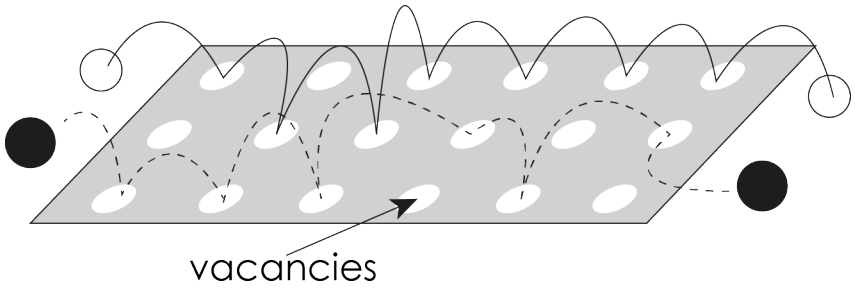

Figure 2.1.6: Sketch of surface diffusion mechanism

The approach to diffusion based upon Fick's law

$$\mathbf{J_i} = -\mathcal{D}_i^e \nabla \mathbf{c_i} \tag{2.1}$$

is inaccurate in describing mass transfer phenomena when the pore diameter falls into the range of mesopores and micropores because the constitutive equation (2.1) does not account for the fact that bulk and Knudsen diffusion mechanisms occur simultaneously [18]. Secondly, in the case of diffusion with a non-equimolar chemical reaction, the

pressure changes inside the pore and the contribution to diffusion given by the viscous flow

$$\mathbf{J_{i,visc}} = -c_i \left(\frac{B_0}{\mu} \right) \nabla \mathbf{p} \tag{2.2}$$

are completely neglected. An accurate description of the physical significance for each symbol herein used can be found in the **List of Symbols**.

A more suitable model for overcoming the latter limitation was proposed by Maxwell and Stefan [18]. They developed a new, rigorous diffusion model with physical foundations based on the exchanges of momentum between the molecules of the diffusing species. Due to its strong physical basis, in contrast to the axiomatic nature of Fickian approach, the Maxwell-Stefan model is able to account for a wider range of contributions to the diffusion process.

In particular, the pressure gradients are natively included. In the following, the physical basis and the mathematical derivation for the Maxwell-Stefan model is presented.

2.2 Derivation of Maxwell-Stefan diffusion equation

The mathematical derivation of the Maxwell-Stefan model starts from considering a gaseous mixture and applying the law of conservation for momentum **M** on every species.

The formulation for the balance follows the logical statement

$$ACC = IN - OUT + PROD \tag{2.3}$$

where

- IN: is the amount of the considered species which enters into the control volume per unit of time
- OUT: describes the amount of the considered species which is leaving the control volume per unit of time
- PROD: is the reacting term and represents the amount of the considered species converted per unit of time

- ACC: is the amount of the considered species which is accumulated in the control volume per unit of time.

The control volume is infinitesimal and the cross sectional area is unitary (see Figure (2.2.1)).

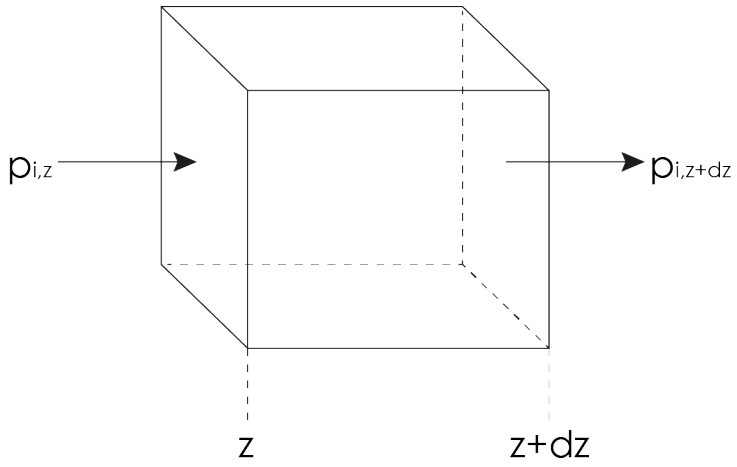

Figure 2.2.1: Sketch of infinitesimal control volume

The forces to be balanced are those deriving from changes in the partial pressure p_i and those deriving by mutual internal friction between species.

The following set of hypotheses is assumed:

1. monodimensional domain along z axis
2. steady state conditions
3. no net production for **M**
4. ideal gas mixture
5. constant temperature

2.2.1 Forces depending on the partial pressures

Focusing on p_i, applying Taylor's expansion

$$p_{i,z+dz} = p_{i,z} + \left(\frac{\partial p_i}{\partial z}\right) \mathrm{d}z \tag{2.4}$$

allows to state that $-\left(\frac{\partial p_i}{\partial z}\right)$ is the force acting per unit of volume and $-\frac{1}{c_i}\left(\frac{\partial p_i}{\partial z}\right)$ the force acting per mole of species *i*.

At constant temperature, under the hypothesis of ideal gas behavior, the following equalities hold

$$c_i = \frac{p_i}{RT} \tag{2.5}$$

$$\mathrm{d}\mu_i = RT\mathrm{d}\log p_i \tag{2.6}$$

where Equation (2.6) is the Lewis standard definition for ideal gas fugacity.

The combination of Equations (2.5) and (2.6) into $-\frac{1}{c_i}\left(\frac{\partial p_i}{\partial z}\right)$ shows that forces deriving from changes of partial pressure can be expressed directly in terms of the chemical potential gradient as $-\frac{1}{c_i}\left(\frac{\partial p_i}{\partial z}\right)$ equals to $-\left(\frac{\partial \mu_i}{\partial z}\right)$.

Thus, the forces depending on partial pressures are described by Equation (2.7)

$$\mathbf{F_{i,p}} = -\left(\frac{\partial \mu_i}{\partial z}\right) \tag{2.7}$$

which can be easily cast into three dimensional notation leading to

$$\mathbf{F_{i,p}} = -\nabla \mu_i \tag{2.8}$$

2.2.2 Forces depending on the mutual drag

Internal frictional forces must balance the pressure forces in order to guarantee the mechanical equilibrium. Every molecule is influenced by the surrounding ones, as depicted in Figure (2.2.2).

The Maxwell-Stefan model states that these forces are proportional, through an appropriate coefficient, to the velocity difference of species and to their concentration expressed by the mole fraction of component *i*.

Therefore, an expression for such coefficient, called drag coefficient is provided:

$$\frac{RT}{\mathcal{D}_{MS}} \tag{2.9}$$

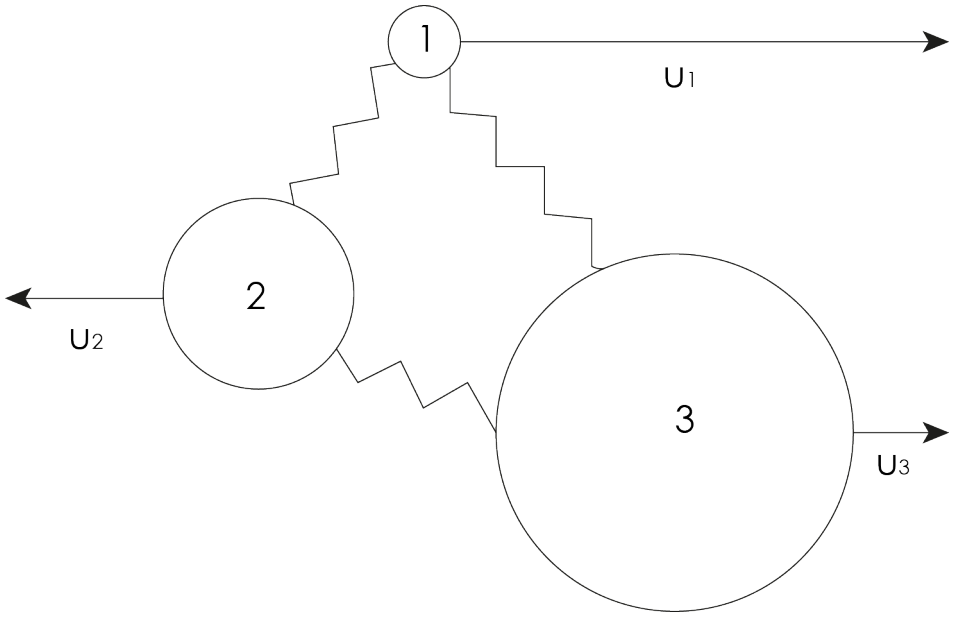

Figure 2.2.2: Mutual interaction between different species in the mixture

With this definition, Maxwell-Stefan diffusivity $\mathcal{D}_{MS}$ has the usual units $\left[\frac{\mathrm{m}^2}{\mathrm{s}}\right]$ and the physical meaning of an inverse drag coefficient.

Velocity differences between one molecule and every remaining molecule must be computed. It follows that deriving drag forces requires a summation all over the molecules in the mixture

$$\mathbf{F_{i,d}} = RT \sum_{\substack{j=1 \\ j \neq i}}^{n} \frac{x_j \left(\mathbf{u_i} - \mathbf{u_j}\right)}{\mathcal{D}_{ij,MS}} \tag{2.10}$$

where self-interactions, and consequently the self-diffusion coefficients $\mathcal{D}_{ii,MS}$, must be excluded.

The equivalence of Equations (2.8) and (2.10) leads to a first formulation of the Maxwell-Stefan model

$$-\nabla \mu_i = RT \sum_{\substack{j=1 \\ j \neq i}}^{n} \frac{x_j \left(\mathbf{u_i} - \mathbf{u_j}\right)}{\mathcal{D}_{ij,MS}} \tag{2.11}$$

which depends on the reference velocity frame chosen for the diffusion process. Some refinement to get a more convenient expression is therefore needed. Firstly, both sides of Equation (2.11) are multiplied by $\left(\frac{x_i}{RT}\right)$; secondly, recalling that

$$\mathbf{N_i} = c_t x_i \mathbf{u_i} \tag{2.12}$$

and after substitution, Equation (2.11) leads to a formulation which does not depend on the reference velocity frame

$$-\frac{x_i}{RT}\nabla\mu_i = \sum_{\substack{j=1 \\ j\neq i}}^{n} \frac{x_j\mathbf{N_i} - x_i\mathbf{N_j}}{c_t\mathcal{D}_{ij,MS}} \tag{2.13}$$

2.2.3 Generalization of diffusion under external forces

The most useful aspect of approaching diffusion phenomena through Maxwell-Stefan model is the easiness of extending it for simultaneously considering the contribution of external forces, such as electrostatic potential gradients, centrifugal forces *etc.*, to the overall diffusion process.

External forces are accounted for by the means of a proper quantity $\mathbf{d_i}$ called *generalized driving force*. In the simplest situation, where no external forces are acting on the system, the generalized driving force is defined as

$$\mathbf{d_i} = -\frac{x_i}{RT}\nabla\mu_i \tag{2.14}$$

From $\mathbf{d_i}$ the force acting per volume of mixture and the force acting per mole of component *i*, $c_t RT\mathbf{d_i}$ and $\frac{\mathbf{d_i}}{x_i}$ respectively, can be quickly calculated.

Assuming that $\widetilde{\mathbf{F}}_\mathbf{i}$ represents the external force acting per unit of mass of species *i* and converting it to its per volume counterpart, the generalized driving force for diffusion is modified as follows

$$\mathbf{d_i} = -\frac{x_i}{RT}\nabla\mu_i + \frac{\rho_i\widetilde{\mathbf{F}}_\mathbf{i}}{c_t RT} \tag{2.15}$$

Under the action of external forces the balance for momentum

$$\frac{\mathrm{d}\mathbf{v}}{\mathrm{d}t} + \nabla\cdot\overline{\overline{\tau}} = \sum_i^n \omega_i\widetilde{\mathbf{F}}_\mathbf{i} - \frac{\nabla p}{\rho} \tag{2.16}$$

must be considered. However, in applications of relevance to chemical engineering, the mechanical equilibrium is reached far quicker than the thermodynamic equilibrium

[18], so the constraint (2.16) can be safely modified to the simpler form

$$\sum_{i=1}^{n} \omega_i \widetilde{\mathbf{F}}_\mathbf{i} - \frac{\nabla p}{\rho} = 0 \tag{2.17}$$

This equation is included in the generalized driving force, leading to

$$\mathbf{d_i} = -\frac{x_i}{RT}\nabla\mu_i + \frac{\rho_i \widetilde{\mathbf{F}}_\mathbf{i}}{c_t RT} + \frac{\rho_i}{c_t RT}\left(\sum_{i=1}^{n} \omega_i \widetilde{\mathbf{F}}_\mathbf{i} - \frac{\nabla p}{\rho}\right) \tag{2.18}$$

Now, the chemical potential gradient must be divided into two parts to explicitly show the contribution of pressure gradient

$$\nabla\mu_i = \nabla_{T,p}\mu_i + \widetilde{V}_i \nabla p \tag{2.19}$$

The subsequent inclusion of Equation (2.19) into Equation (2.18) yields to an alternative formulation for $\mathbf{d_i}$:

$$\mathbf{d_i} = -\frac{x_i}{RT}\nabla_{T,p}\mu_i - \frac{1}{c_t RT}\left(c_i\widetilde{V}_i - \omega_i\right)\nabla p + \frac{\rho_i}{c_t RT}\left(\widetilde{\mathbf{F}}_\mathbf{i} - \sum_{i=1}^{n} \omega_i \widetilde{\mathbf{F}}_\mathbf{i}\right) \tag{2.20}$$

The comparison between Equation (2.13)

$$-\frac{x_i}{RT}\nabla\mu_i = \sum_{\substack{j=1 \\ j\neq i}}^{n} \frac{x_j \mathbf{N_i} - x_i \mathbf{N_j}}{c_t \mathcal{D}_{ij,MS}}$$

and Equation (2.20) leads to the general formulation of the Maxwell-Stefan model:

$$-\frac{x_i}{RT}\nabla_{T,p}\mu_i - \frac{1}{c_t RT}\left(c_i\widetilde{V}_i - \omega_i\right)\nabla p + \frac{\rho_i}{c_t RT}\left(\widetilde{\mathbf{F}}_\mathbf{i} - \sum_{i=1}^{n} \omega_i \widetilde{\mathbf{F}}_\mathbf{i}\right) = \sum_{\substack{j=1 \\ j\neq i}}^{n} \frac{x_j \mathbf{N_i} - x_i \mathbf{N_j}}{c_t \mathcal{D}_{ij,MS}} \tag{2.21}$$

In particular, when dealing with ideal gas mixtures, Equation (2.21) simplifies to:

$$-\nabla x_i - \frac{1}{p}\left(x_i - \omega_i\right)\nabla p + \frac{\rho_i}{p}\left(\widetilde{\mathbf{F}}_\mathbf{i} - \sum_{i=1}^{n} \omega_i \widetilde{\mathbf{F}}_\mathbf{i}\right) = \sum_{\substack{j=1 \\ j\neq i}}^{n} \frac{x_j \mathbf{N_i} - x_i \mathbf{N_j}}{c_t \mathcal{D}_{ij,MS}} \tag{2.22}$$

While proving that

$$\frac{c_i}{c_t}\frac{\widetilde{V}_i}{RT} = \frac{x_i}{p} \tag{2.23}$$

is a straightforward application of the ideal gas equation of state, proving that

$$\frac{x_i}{RT}\nabla_{T,p}\mu_i = \nabla x_i \tag{2.24}$$

involves mathematical manipulation of thermodynamics equalities regarding chemical potential and partial molar Gibbs free energy.

Remembering that [26]:

1. for mixtures, the chemical potential and the partial molar Gibbs free energy are the same, and so their differential

$$\mathrm{d}\mu_i = \mathrm{d}g_i \tag{2.25}$$

2. the residual Gibbs free energy g_i^{R} is the difference between g_i in the current state of the mixture and g_i with respect to the ideal gas mixture state, where Lewis-Randall law holds

$$\hat{f}_i = f_i x_i \tag{2.26}$$

3. the mixture fugacity coefficient $\hat{\phi}_i$ is defined as

$$\hat{\phi}_i = \frac{\hat{f}_i}{f_i x_i} \tag{2.27}$$

4. a correlation between g_i^{R} and $\hat{\phi}_i$ exists

$$RT\log\hat{\phi}_i = g_i^{\mathrm{R}} \tag{2.28}$$

a chain of equivalences follows:

$$\mathrm{d}g_i^{\mathrm{R}} = RT\mathrm{d}\log\hat{f}_i - RT\mathrm{d}\log f_i x_i \tag{2.29}$$

$$\mathrm{d}g_i^{\mathrm{R}} = RT\mathrm{d}\log\hat{\phi}_i \tag{2.30}$$

$$\mathrm{d}\log\hat{\phi}_i = \frac{1}{RT}\mathrm{d}\mu_i - \mathrm{d}\log f_i x_i \tag{2.31}$$

Rewriting the last equation in three dimensional notation in conjunction with the chain derivation rule

$$\nabla \log \hat{\phi}_i = \frac{\partial \log \hat{\phi}_i}{\partial x_i} \nabla x_i = \frac{\nabla \mu_i}{RT} - \frac{\nabla x_i}{x_i} \tag{2.32}$$

allows to prove the following

$$\frac{x_i}{RT} \nabla_{T,p} \mu_i = \nabla x_i$$

In fact, algebraic manipulation of Equation (2.32) leads to

$$\frac{x_i}{RT} \nabla_{T,p} \mu_i = \left(1 + x_i \frac{\partial \log \hat{\phi}_i}{\partial x_i} \right) \nabla x_i \tag{2.33}$$

which reduces to Equation (2.24) for ideal gas mixtures ($\hat{\phi}_i = 1$).

Another advantage is that the Maxwell-Stefan diffusivity and the Fick diffusivity are the same for ideal gas mixtures as they are bounded by the relation

$$\mathcal{D}_{ij} = \left(1 + x_i \frac{\partial \log \hat{\phi}_i}{\partial x_i} \right) \mathcal{D}_{ij,MS} \tag{2.34}$$

The Maxwell-Stefan model herein derived accounts for a broader number of contributions to diffusion processes with respect to the Fick model, which is the most commonly used. Thus, it is suitable as a supporting basis for the development a new diffusion model, as described in the following.

2.3 The dusty gas model for diffusion in porous structures

The need of a new model for intraporous diffusion arises from the fact that a Fickian approach is not suitable for describing combined bulk and Knudsen diffusion mechanimism occurring in mesopores and micropores.

The best solution is using a model which is a particular expression of the Maxwell-Stefan diffusion equations, called *dusty gas model*: the reason behind this name is that the pore wall is considered to be a dummy species consisting of giant molecules (*dust*) uniformly distributed in space.

In a mixture of *n* species, regarding the dust as an additional $(n+1)^{th}$ component, the whole system including species and dust is actually a pseudomixture, as depicted in Figure (2.3.1) [32].

Another useful aspect of the dusty gas formulation is the chance of directly account for viscous flow right from the beginning.

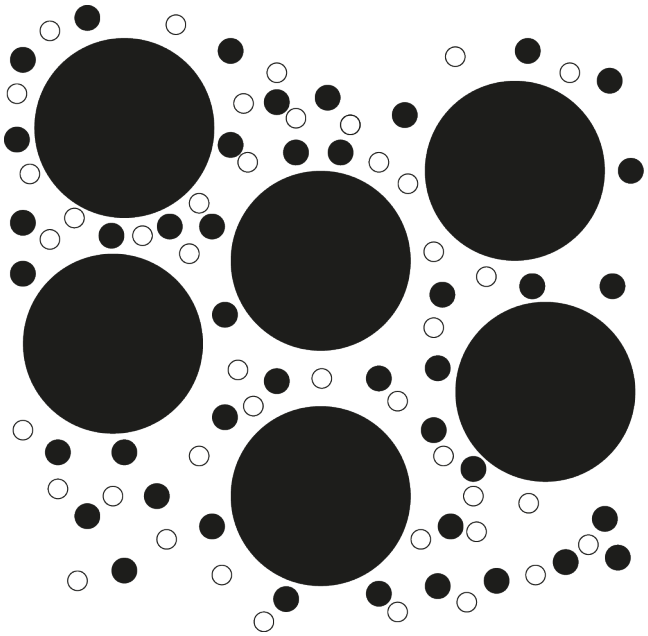

Figure 2.3.1: Sketch of dusty gas

To obtain equations describing the dusty gas model, the following set of assumptions must be applied:

1. the dust concentration is spatially uniform, i.e. $\nabla x_{n+1} = 0$
2. the dust is held motionless in space by some clamping force, so that $N_{n+1} = 0$
3. the molar mass of the dust particles approaches $+\infty$

In order to satisfy the second requirement the dust molecules must be constrained by external forces. Physically, these represent the support forces exerted on the dust molecules which 'clamp' the molecules, preventing them from moving in response to gas pressure gradients, i.e.

$$\nabla p = c_{n+1}\mathbf{F_{n+1}} \tag{2.35}$$

As an additional assumption, no external forces are acting on the remaining species

$$\mathbf{F_i} = \mathbf{0} \qquad i = 1, \dots n \tag{2.36}$$

2.3.1 Mathematical formulation of the dusty gas model

The formulation of the model is a straigthforward application of the Maxwell-Stefan equation. The resulting set of equations is slightly different if the importance of pressure gradient is relevant or not.

Jakobsen and Solsvik [28] proposed a formulation where pressure gradient and so viscous flow are neglected

$$\mathbf{N_i} = \left(\frac{\sum_{\substack{j=1 \\ j \neq i}}^{n} \frac{\mathbf{N_j} x_i}{\mathcal{D}_{ij}} - \frac{c_i \mathbf{u}}{\mathcal{D}_{i,K}} - c_t \nabla x_i}{\sum_{\substack{j=1 \\ j \neq i}}^{n} \frac{x_j}{\mathcal{D}_{ij}} + \frac{1}{\mathcal{D}_{i,K}}} \right) \tag{2.37}$$

while Malinauskas and Mason [22] proposed a more general expression

$$\sum_{\substack{j=1 \\ j \neq i}}^{n} \frac{x_j \mathbf{N_i} - x_i \mathbf{N_j}}{p \mathcal{D}^e_{ij}} - \frac{\mathbf{N_i}}{p \mathcal{D}^e_{i,K}} = \frac{\nabla x_i}{RT} + \frac{x_i}{pRT} \left(\frac{B_0 p}{\mu \mathcal{D}^e_{i,K}} + 1 \right) \nabla p \tag{2.38}$$

which will be the one analyzed from here on.

Equation (2.38) can be conveniently rewritten in terms of vector algebra [16]

$$\mathbf{N} = \mathbf{A}^{-1} \mathbf{b} \tag{2.39}$$

where the elements in the coefficient matrix A and in the vector $\mathbf{b}$ are set according to the following rules:

1. if $i = j$

$$A_{ii} = \frac{1}{p \mathcal{D}^e_{i,K}} + \sum_{\substack{j=1 \\ j \neq i}}^{n} \frac{x_j}{p \mathcal{D}^e_{ij}} \tag{2.40}$$

2. if $i \neq j$

$$A_{ij} = -\frac{x_i}{p \mathcal{D}^e_{ij}} \tag{2.41}$$

3. for $i = 1, \dots n$

$$b_i = -\frac{1}{RT} \left(\nabla x_i + \frac{x_i}{p} \left(\frac{B_0 p}{\mu \mathcal{D}^e_{i,K}} + 1 \right) \nabla p \right) \tag{2.42}$$

From a physical point of view, Equation (2.22)

$$-\nabla x_i - \frac{1}{p}\left(x_i - \omega_i\right)\nabla p + \frac{\rho_i}{p}\left(\widetilde{\mathbf{F}}_\mathbf{i} - \sum_{i=1}^{n}\omega_i\widetilde{\mathbf{F}}_\mathbf{i}\right) = \sum_{\substack{j=1\\ j\neq i}}^{n}\frac{x_j\mathbf{N_i} - x_i\mathbf{N_j}}{c_t\mathcal{D}_{ij,MS}}$$

or Equation (2.38)

$$\sum_{\substack{j=1\\ j\neq i}}^{n}\frac{x_j\mathbf{N_i} - x_i\mathbf{N_j}}{p\mathcal{D}^e_{ij}} - \frac{\mathbf{N_i}}{p\mathcal{D}^e_{i,K}} = \frac{\nabla x_i}{RT} + \frac{x_i}{pRT}\left(\frac{B_0 p}{\mu\mathcal{D}^e_{i,K}} + 1\right)\nabla p$$

can be successfully used in mathematical simulations of both reacting and not reacting systems through the appropriate set of partial differential equations.

Given a consistent set of boundary and initial conditions, the existence of a unique and regular solution is guaranteed [3]. Even if the solution exists, this does not necessarily mean that it is analytical; in most cases it is actually impossible to find an analytical solution, so the numerical solution is unavoidable.

So far in this work, different diffusion models (Fick, Maxwell-Stefan, dusty gas) have been presented. These models provide expressions to describe quantitatively the diffusion phenomenon, which is one of the way physical systems exchange mass through (the other being advection). In particular, these expressions can be used to obtain equations describing the conservation of mass through time in a system with arbitrary geometry, the so called *transport equations*. In the following, an overview about the derivation of the partial differential equation modelling the conservation of mass, together with some technique for its numerical solution, is shortly presented.

2.4 Simultaneous advection-diffusion with reaction modeling

The partial differential equation underlying the physical phenomenon of advection-diffusion accompanied by reaction is an expression of mass conservation law (see Equation (2.3)) applied to an infinitesimal control volume Ω with enclosing surface S.

The basic equality is

$$\frac{\partial}{\partial t}\int_{\Omega} c_i \mathrm{d}\Omega = -\int_{S} (\mathbf{N_i}\cdot\mathbf{n})\,\mathrm{d}S - \int_{S} (c_i\mathbf{v}\cdot\mathbf{n})\,\mathrm{d}S + \int_{\Omega} R_{i,reac}\mathrm{d}\Omega \tag{2.43}$$

By taking the derivative under the sign of integral, applying the divergence theorem to the surface integral on the right and exploiting integral linearity, the equality transforms into

$$\int_{\Omega}\left(\frac{\partial c_i}{\partial t} + \nabla\cdot(\mathbf{N_i}) + \nabla\cdot(c_i\mathbf{v}) - R_{i,reac}\right)\mathrm{d}\Omega = 0 \tag{2.44}$$

Since the control volume is chosen arbitrarily, the only way to satisfy Equation (2.44) ends up to be setting the integrand to zero, i.e.

$$\frac{\partial c_i}{\partial t} = -\nabla\cdot\mathbf{N_i} - \nabla\cdot(c_i\mathbf{v}) + R_{i,reac} \tag{2.45}$$

which is the partial differential equation [10] for describing molar mass balance in reacting systems, alternatively rewritten as

$$\frac{1}{RT}\frac{\partial p_i}{\partial t} = -\nabla\cdot\mathbf{N_i} - \frac{1}{RT}\nabla\cdot(p_i\mathbf{v}) + R_{i,reac} \tag{2.46}$$

when ideal gas law applies. Molar fluxes $\mathbf{N}_i$ can be expressed following Fickian or dusty gas approach.

A well-posed set of boundary conditions and an initial time data are needed to solve the problem, as shown in Equation (2.47):

$$\begin{cases} \dfrac{\partial c_i}{\partial t} = -\nabla\cdot\mathbf{N_i} - \nabla\cdot(c_i\mathbf{v}) + R_{i,reac} \\ c_i = c_{i,0} \qquad on \quad \mathrm{S} \\ c_i(\Omega,0) = c_i(\Omega) \qquad \mathrm{t} = 0 \end{cases} \tag{2.47}$$

In this work no advection is considered since the dusty gas model is used for the solid phase where advection is not present. Under this hypothesis, Equation (2.45) becomes

$$\frac{\partial c_i}{\partial t} = -\nabla\cdot\mathbf{N_i} + R_{i,reac} \tag{2.48}$$

2.5 Conclusions

In this chapter the mathematical formulation of the dusty gas model have been presented. It has been shown that the dusty gas model, due to its more rigorous theoretical basis deriving from Maxwell-Stefan approach to diffusion, grants superior accuracy in describing combined bulk and Knudsen diffusion in porous media where the Fick approach fails even at the qualitative level. The higher accuracy is counterbalanced by an increased complexity in the computation of molar fluxes as it is not possible to write an explicit dependance between fluxes and concentrantion/mole fraction gradient but a linear system of algebraic equations must be solved instead. The main advantage of the dusty gas formulation is the possibility of accounting for a wider range of contribution to the diffusion process such as external forces or pressure gradients due to chemical reactions. These contributions are neglected in the commonly used Fick approach.

Chapter 3

Comparison between the dusty gas model and the Fick's law

In this chapter, a comparison between dusty gas model and two formulations of Fick law is carried out investigating the effect of reaction stoichiometry, reaction kinetics and diffusivity on each model. To solve the resulting systems of partial differential equations, finite differences techniques are used.

3.1 Problem characterization

The standard Fickian approach does not take into account possible effects that mutual drag or pressure gradient can have on mass transport. Even the extended Fick model, that accounts for viscous flows, omits to consider drag effects. For this reason, the results obtained with the former approaches can show different results with respect to those achieved by the dusty gas formulation. To highlight differences and similarities between the dusty gas approach and two different Fickian approaches, the unsteady behavior of a reactive, porous sphere has been studied. In particular, the effect of reaction stoichiometry, reaction kinetics and diffusivity on mole fraction and pressure profiles has been analyzed. In the following, the modeling of this specific problem is presented. The catalytic porous particle, if its properties (ϵ, τ) are considered uniform, shows radial symmetry. Therefore, the boundary and initial conditions must show radial symmetry too. For this reason, the indefinite mass balance can be treated as monodimensional along

the radius, splitting the domain in concentrical, spherical shells. The set of equations obtained in this way requires an initial condition on time and two boundary conditions on the spatial domain.

Recalling that:

1. $$\frac{\partial}{\partial t}\int_{\Omega} c_i \mathrm{d}\Omega = -\int_{S} (\mathbf{N_i}\cdot\mathbf{n})\,\mathrm{d}S + \int_{\Omega} R_{i,reac}\mathrm{d}\Omega$$

   where, for a spherical shell,

$$\begin{cases} \mathrm{d}S_{in} = 4\pi r^2 \\ \mathrm{d}S_{out} = 4\pi(r+\mathrm{d}r)^2 \sim 4\pi r^2 + 8\pi r \mathrm{d}r \\ \mathrm{d}V = 4\pi r^2 \mathrm{d}r \end{cases} \tag{3.1}$$

2. according to Taylor's theorem

$$\mathbf{N_{i,r+dr}}\cdot S_{out} = \mathbf{N_{i,r}}\cdot S_{in} + \frac{\partial(N_i\cdot S)}{\partial r}\mathrm{d}r$$

3. ideal gas law holds

the molar mass balance in the spherical shell results in

$$\frac{1}{RT}\frac{\partial p_i}{\partial t} = \frac{\partial \mathbf{N_i}}{\partial r} + \frac{2}{r}\mathbf{N_i} + R_{i,react} \tag{3.2}$$

The resulting set of partial differential equations are solved by the means of the *method of lines*. This is a numerical method which solves PDEs by replacing spatial derivatives with finite differences derivatives. The finite differences methods used in this work are presented below.

3.2 Test case: diffusion with reaction in a catalytic sphere

3.2.1 Numerical approach to the sphere problem

To obtain the numerical solution for the set of equations that describes the diffusion with reaction problem in a spherical catalyst, the spatial domain has been discretized.

The number of points chosen to split it will be indicated as *N* from now on. The criteria to choose an adequate number of points are explained in the **convergence analysis** subsection. No discretization was necessary for the time variable as the MATLAB® built-in routine *ode15s* was used to deal with it. With this approach, the partial differential algebraic equations system consisting in the following (*NC+1*) equations

$$\begin{cases} \dfrac{1}{RT}\dfrac{\partial p_i}{\partial t} = \dfrac{\partial \mathbf{N_i}}{\partial r} + \dfrac{2}{r}\mathbf{N_i} + \nu_i R_{i,react} \\ p = \displaystyle\sum_{i=1}^{n} p_i \end{cases} \tag{3.3}$$

becomes a differential algebraic equations system of N groups of $(NC+1)$ equations, each one corresponding to one grid point. The groups from point $2 \dots (N-1)$ are structured as

$$\begin{cases} \dfrac{1}{RT}\dfrac{\partial p_{i,j}}{\partial t} = \left.\dfrac{\partial N_i}{\partial r}\right|_j + \dfrac{2}{r}N_{i,j} + \nu_i R_{i,j,react} \\ p_j = \displaystyle\sum_{i=1}^{n} p_{i,j} \end{cases} \tag{3.4}$$

As initial and boundary conditions required, an internal partial pressure profile of pure inert and a fixed value on one edge were chosen, where the latter expresses the condition of the reactant presence outside the sphere. Due to the symmetry of porous media, it was possible to use a zero derivative condition in the center of the sphere instead of a fixed value on the other edge. For this reason, only half domain was studied. Due to the applied discretization, the boundary conditions appear as the first and last groups of equations structured in the following way:

$$\begin{cases} p_{i,1} = p_{i,out} \\ p_1 = p_{out} \\ \left.\dfrac{\partial p_i}{\partial r}\right|_N = 0 \\ \left.\dfrac{\partial p}{\partial r}\right|_N = 0 \end{cases} \tag{3.5}$$

The n^{th} group of equations can be obtained by assigning zero value to the discretized derivative of the corresponding equation variable. Furthermore analyzing the problem, it can be noticed that the groups of equations implemented contain the term $-\frac{\partial N_i}{\partial r}|_j$; the

fluxes $N_{i,j}$ in turn require, independently by the model considered, the terms $-\frac{\partial x_i}{\partial r}|_j$ to be calculated on each point. It was then necessary to choose a way to express those spatial derivatives. A forward differences method was implemented for the mole fraction derivatives while a backward one was used for the molar fluxes. The reasons of this choice will be subsequently explained. It is easy to notice, looking at the boundaries, that N_i and $\frac{\partial N_i}{\partial r}|_j$ values are not needed on the first and the last spatial points. The forward-backward combination adopted allowed to calculate the required terms without any need to change the derivative discretization scheme at the edges. This would have happened in case the discretization model had asked points outside of the domain. To prove this is not the case, the scheme proposed will be further analyzed. Each $N_{i,j}$ and $\frac{\partial N_i}{\partial r}|_j$ couple required the mole fraction values on *(j-1)*th, *j*th and *(j+1)*th point since

$$\begin{cases} \left.\dfrac{\partial N_i}{\partial r}\right|_j = f(N_j, N_{j-1}) \\ N_j = f(x_{i,j}, x_{i,j+1}) \\ N_{j-1} = f(x_{i,j-1}, x_{i,j}) \end{cases} \tag{3.6}$$

and those coupled values were not needed on the first and on the last point.

3.2.2 Selected conditions

The parameters used in the following simulations were chosen relying on literature work [32].

Pure reactant has been considered in each case and results have been compared at steady state. Thus, the external environment with respect to the sphere is full of reactant. A summary of the operating conditions used in each case is presented in Tables (3.2.1) and (3.2.2) [32].

$\mathbf{R_0}$ [m]	$\mathbf{r_p}$ [m]	$\mathbf{B_0}$ [$\mathbf{m^2}$]	ϵ [-]	τ [-]
$1.00{\cdot}10^{-3}$	$2.90{\cdot}10^{-7}$	$4.79{\cdot}10^{-16}$	$4.56{\cdot}10^{-2}$	1.00

Table 3.2.1: Catalyst parameters (sphere radius, pore radius, permeability coefficient, catalyst porosity and tortuosity respectively)

$\mathbf{k_r}$ [s^{-1}]	**T** [K]	μ [Pa s]	$\mathcal{D}_{ij}^0$ [m^2s^{-1}]	M_A [kg mol^{-1}]	M_B [kg mol^{-1}]
981	600	$1.0{\cdot}10^{-5}$	$1.0{\cdot}10^{-4}$	$20{\cdot}10^{-3}$	$\frac{20}{3} \cdot 10^{-3}$

Table 3.2.2: Reaction and transport parameters

For most of the comparisons, a moderate value for the kinetic constant ($\frac{k_r}{9}$) is used to shift the dominant regime from diffusive to a more intermediate one. The simulations proposed deal with bicomponent mixtures. Three aspects have been investigated:

- kinetic constant variation in a non-equimolar case (in a reaction with increasing number of moles) together with catalyst efficiency calculations
- diffusivity order of magnitude variation to check model sensibility to this parameter
- catalyst efficiency estimation according to the dusty gas model by changing the stoichiometric coefficient ratio

3.2.3 Reaction with increasing number of moles

A mole-increasing reaction in the form

$$\mathrm{A} \longrightarrow 3\,\mathrm{B} \tag{3.7}$$

has been tested in order to check variations in pressure profiles.

In Figure (3.2.1), it can be noticed that a mole-increasing stoichiometry causes the pressure to increase. Standard Fick model presents a steeper pressure profile since it does not account for the viscous flow nor for the mutual drag, whose overall effect is influenced by the direction of viscous flow too. On the contrary, extended Fick and dusty gas models, accounting natively for pressure gradient, show similar trend. It is important to notice as even pressure profile in the dusty gas model is not flat. **This happens in unsteady state since the regime is influenced by diffusion limitations so the pressure gradient generated by the reaction (according to the ideal gas laws) cannot be drained efficiently by the outgoing material fluxes. Then, at steady state, the material fluxes need a pressure gradient higher than zero to drain the surplus**

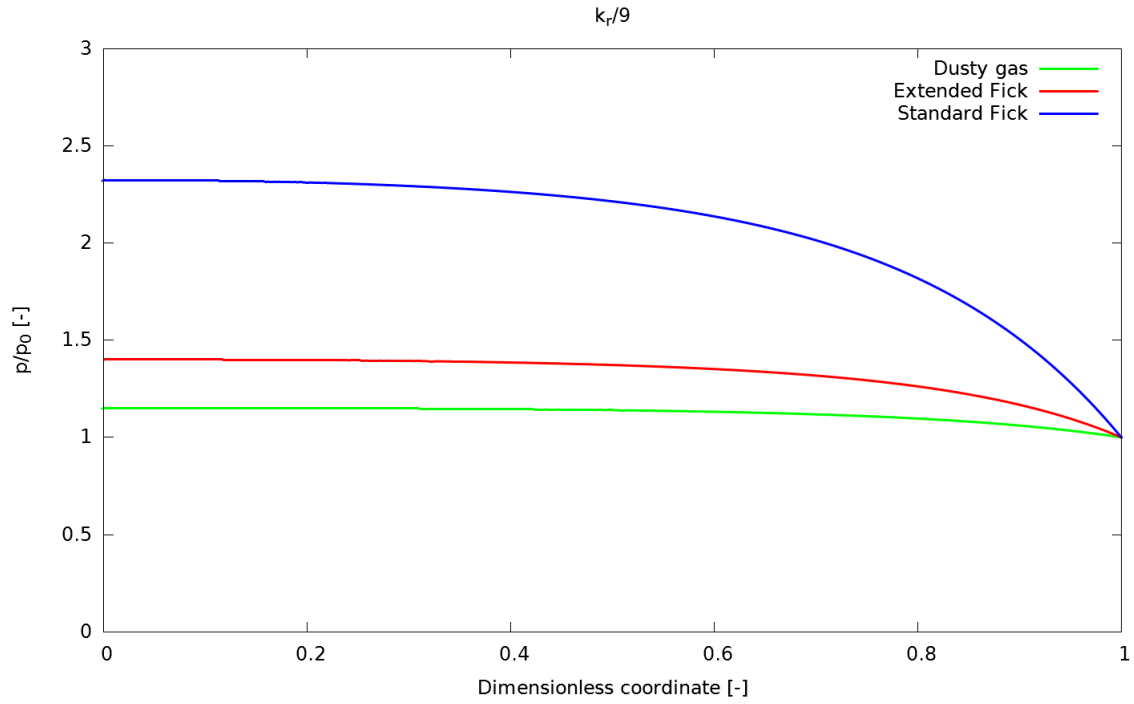

Figure 3.2.1: Pressure ratio in mole-increasing reaction

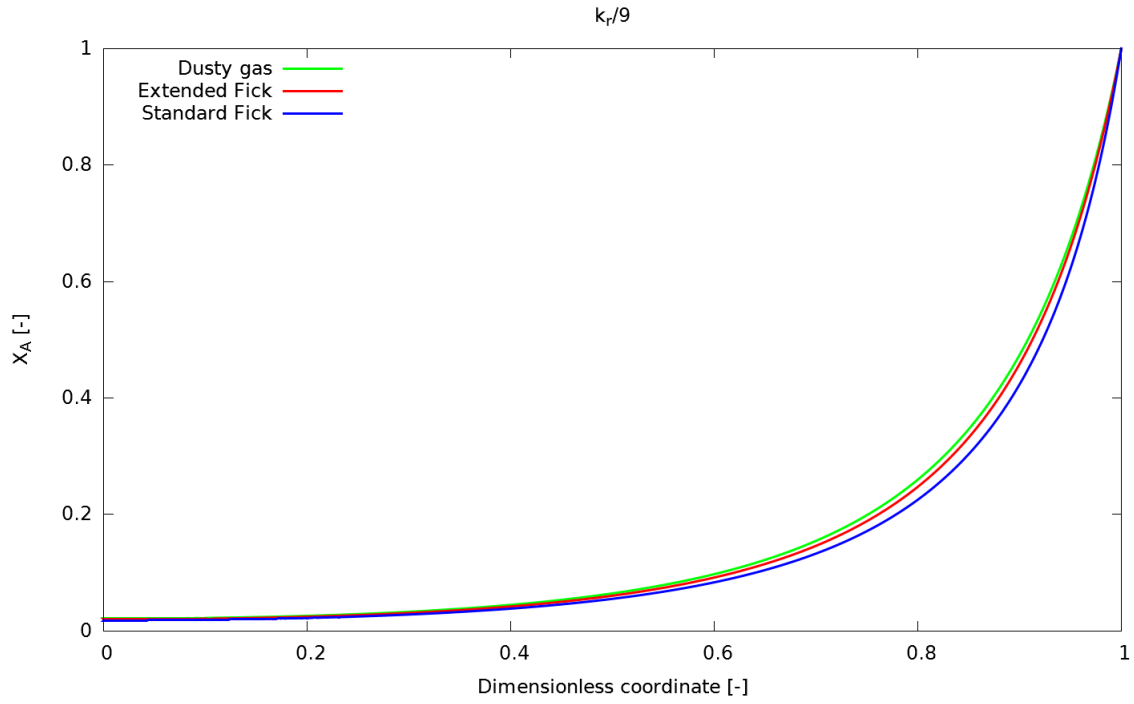

Figure 3.2.2: Mole fraction of component A in mole-increasing reaction. The reference value for the kinetic constant k_r has been divided by 9 to shift the regime to intermediate

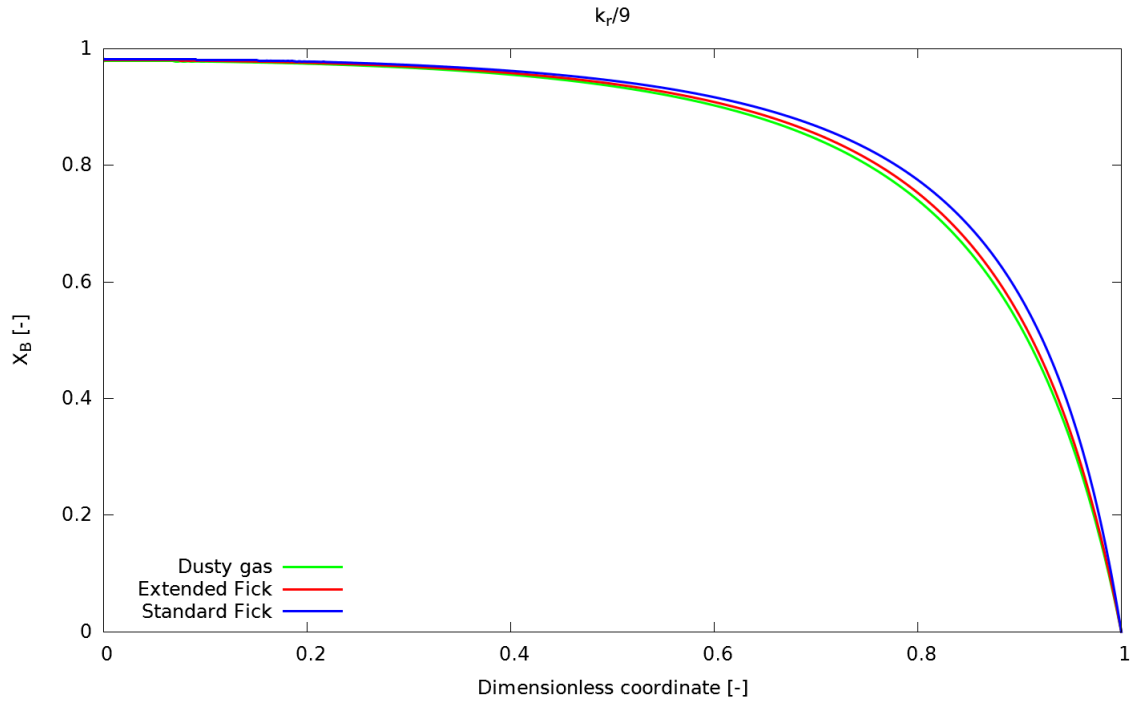

Figure 3.2.3: Mole fraction of component B in mole-increasing reaction. The reference value for the kinetic constant k_r has been divided by 9 to shift the regime to intermediate

of moles and thus avoid changes in profiles. Regarding reactant mole fraction (Figure (3.2.2), extended Fick and dusty gas show nearly overlapping profiles while standard Fick is slightly different. This difference is due to the higher pressure predicted by the standard Fick model. Recalling that the reaction rate is a function of the local partial pressure, a higher pressure implies higher reaction rate, lower mole fraction for reactants and higher for products. A confirmation for this, reported in Figure (3.2.3), comes from the fact that Fick model presents lower reactant mole fractions, a higher reaction rate, due to a higher pressure, leads to lower efficiencies (see Table (3.2.3). This aspect will be further dealt with on the section regarding the **effects of the kinetic constant**.

3.2.4 Reaction with decreasing number of moles

A mole-decreasing reaction in the form

$$3\,\mathrm{A} \longrightarrow \mathrm{B} \tag{3.8}$$

has been tested in order to check variations in pressure profiles.

In Figure (3.2.4), pressure decreases along the catalyst radius as expected. It can be seen again the steeper profile predicted by the standard Fick model since it neglects viscous flow and mutual drag effects. Extended Fick model, only lacking the latter, displays and intermediate pressure profile between the standard Fick and the dusty gas ones. Reactant mole fraction profiles (Figure (3.2.5)) are consequence of two opposite effects

- a lower reaction rate, since it depends on partial pressures which decrease
- a higher incoming flux of reactant due to the more negative pressure gradient.

The dusty gas profile shows less reactant mole fraction since its higher predicted pressure avoid an excessive drop in reaction rate. The lower pressure of extended Fick causes it to show more unreacted species. While standard Fick should show even higher reactant mole fraction, it does not take into account the higher incoming flux caused by the negative pressure gradient. This is the reason why its behavior is intermediate. The formerly described effects can also be noticed on the reaction product side (Figure (3.2.6).

3.2.5 Equimolar reaction

In conclusion, an equimolar reaction in the form

$$A \longrightarrow B \tag{3.9}$$

has been studied. The results are shown , (3.2.8) and (3.2.9).

In Figure (3.2.7), no change in pressure is noticed. This is in agreement with the underlying physics of the problem.

An interesting aspect is the complete equality in results for the three models. The equality of the two alternative Fickian formulations descends naturally from the absence of pressure gradients due to mole variation

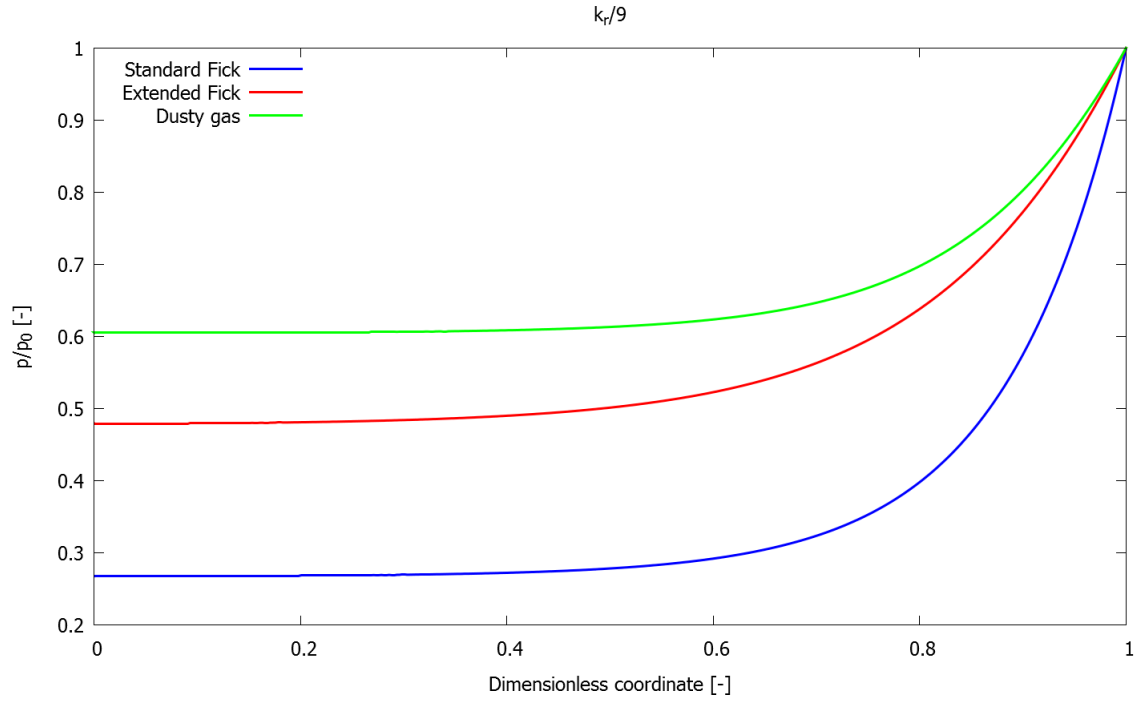

Figure 3.2.4: Pressure profile in mole-decreasing reaction. The reference value for the kinetic constant k_r has been divided by 9 to shift the regime to intermediate

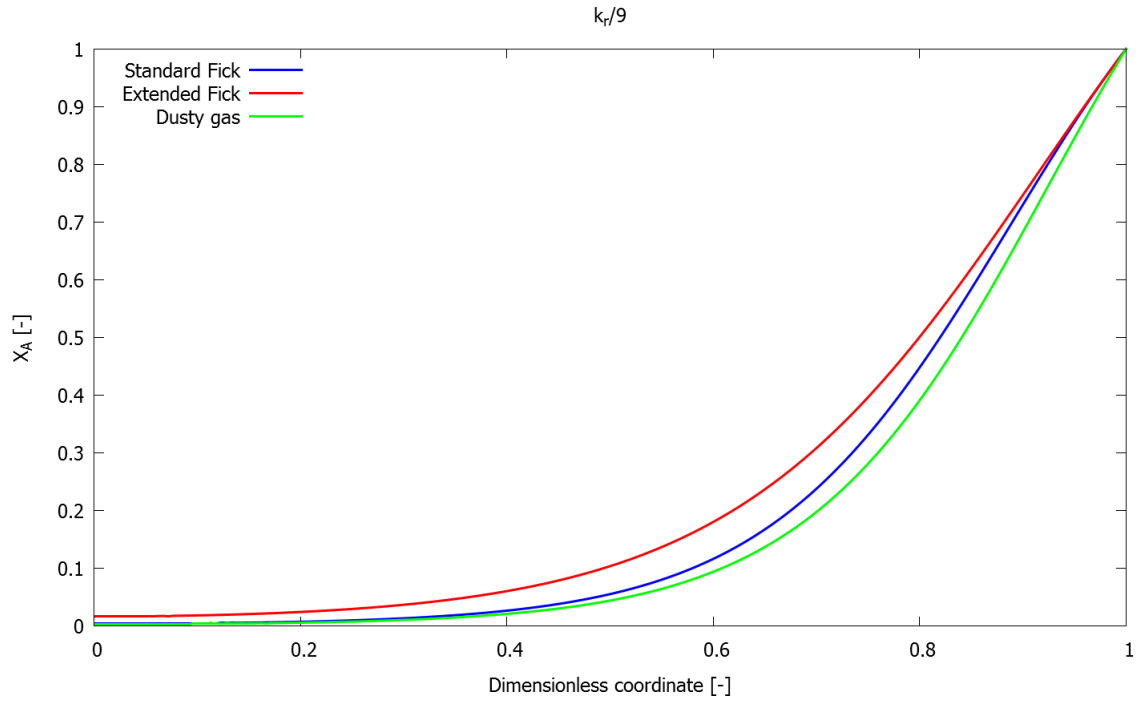

Figure 3.2.5: Species A mole fraction profile in mole-decreasing reaction. The reference value for the kinetic constant k_r has been divided by 9 to shift the regime to intermediate

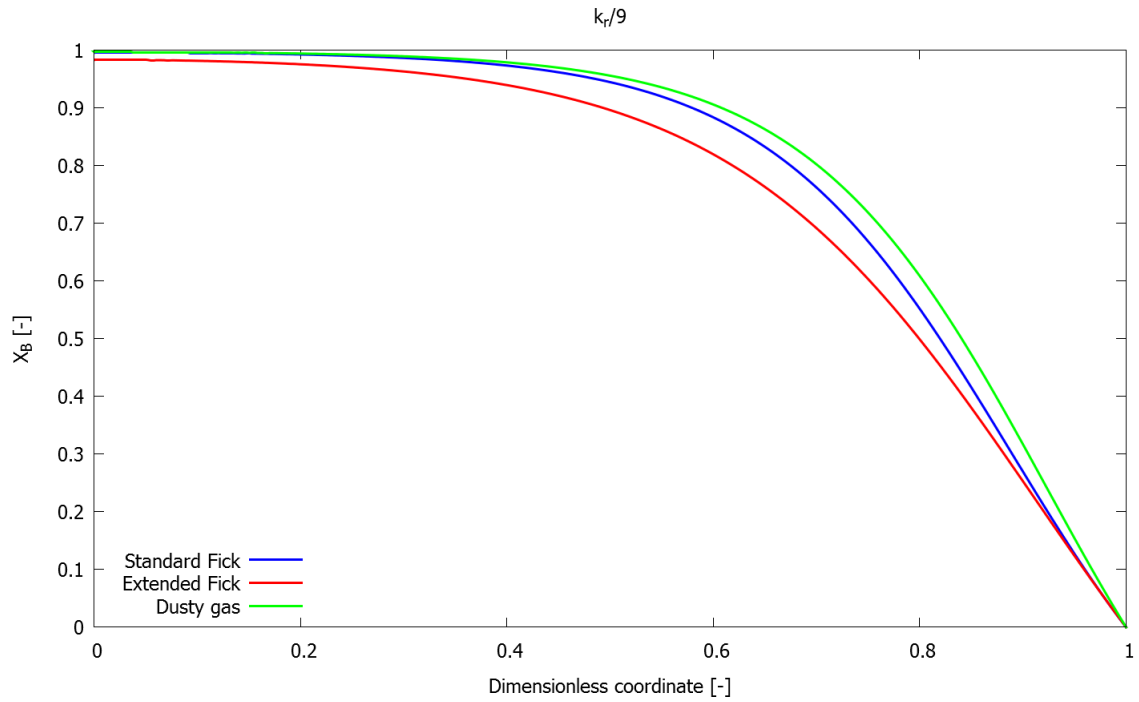

Figure 3.2.6: Species B mole fraction profile in mole-decreasing reaction. The reference value for the kinetic constant k_r has been divided by 9 to shift the regime to intermediate

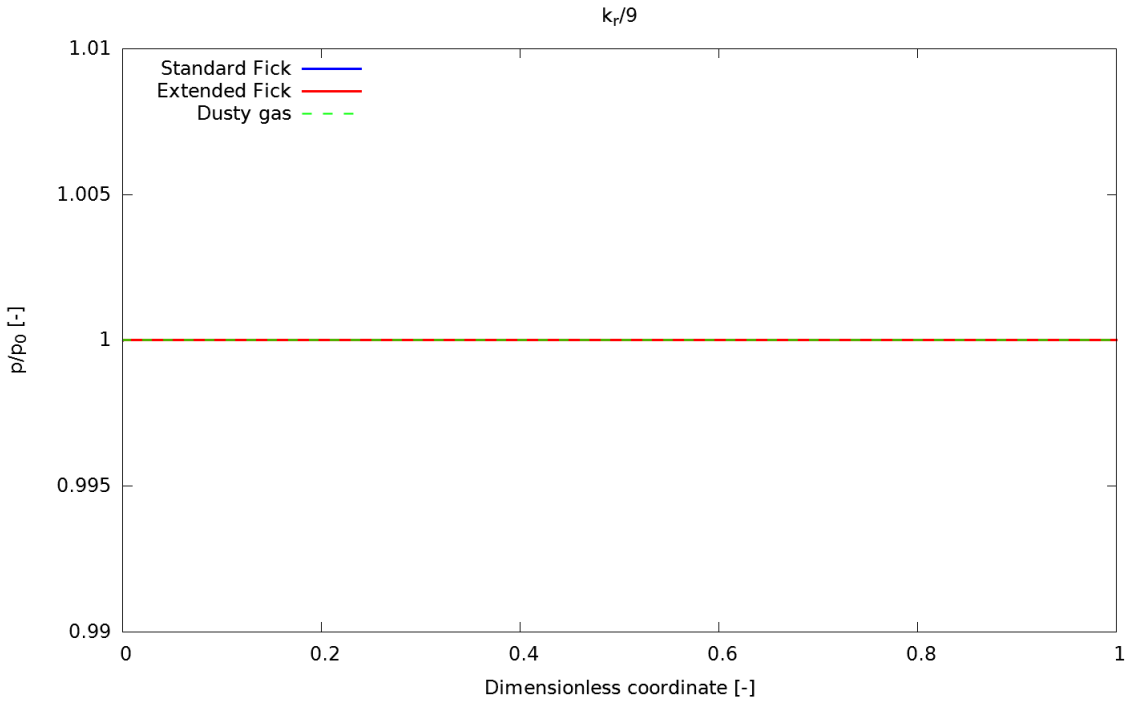

Figure 3.2.7: Pressure profile in equimolar reaction. The reference value for the kinetic constant k_r has been divided by 9 to shift the regime to intermediate

$$\begin{cases} \mathbf{J_i} = -\dfrac{1}{RT}\mathcal{D}_i^e \nabla \mathbf{p_i} \\ \mathbf{J_i} = -\dfrac{1}{RT}\left(\mathcal{D}_i^e \nabla \mathbf{p_i} + \dfrac{B_0 p_i}{\mu}\nabla \mathbf{p}\right) \\ \nabla \mathbf{p} = \mathbf{0} \end{cases}$$

Proving the interchangeability for the dusty gas model involves algebraic manipulation of system (2.39) for the binary case

$$\begin{cases} \dfrac{x_1 N_{2,z} - x_2 N_{1,z}}{\mathcal{D}_{12}} - \dfrac{N_{1,z}}{D_{1,K}} = \dfrac{p}{RT}\dfrac{\partial x_1}{\partial z} \\ \dfrac{x_2 N_{1,z} - x_1 N_{2,z}}{\mathcal{D}_{21}} - \dfrac{N_{2,z}}{D_{2,K}} = \dfrac{p}{RT}\dfrac{\partial x_2}{\partial z} \end{cases} \tag{3.10}$$

Recalling that

1. mole fractions must sum to 1 so $x_2 = 1 - x_1$ and $\frac{\partial x_2}{\partial z} = -\frac{\partial x_1}{\partial z}$

2. the pair of diffusion coefficients is symmetrical, i.e. $\mathcal{D}_{ij} = \mathcal{D}_{ji}$

3. dealing with an equimolar reaction, molecular weigth is the same for reagent and product so $\mathcal{D}_{1,K} = \mathcal{D}_{2,K}$

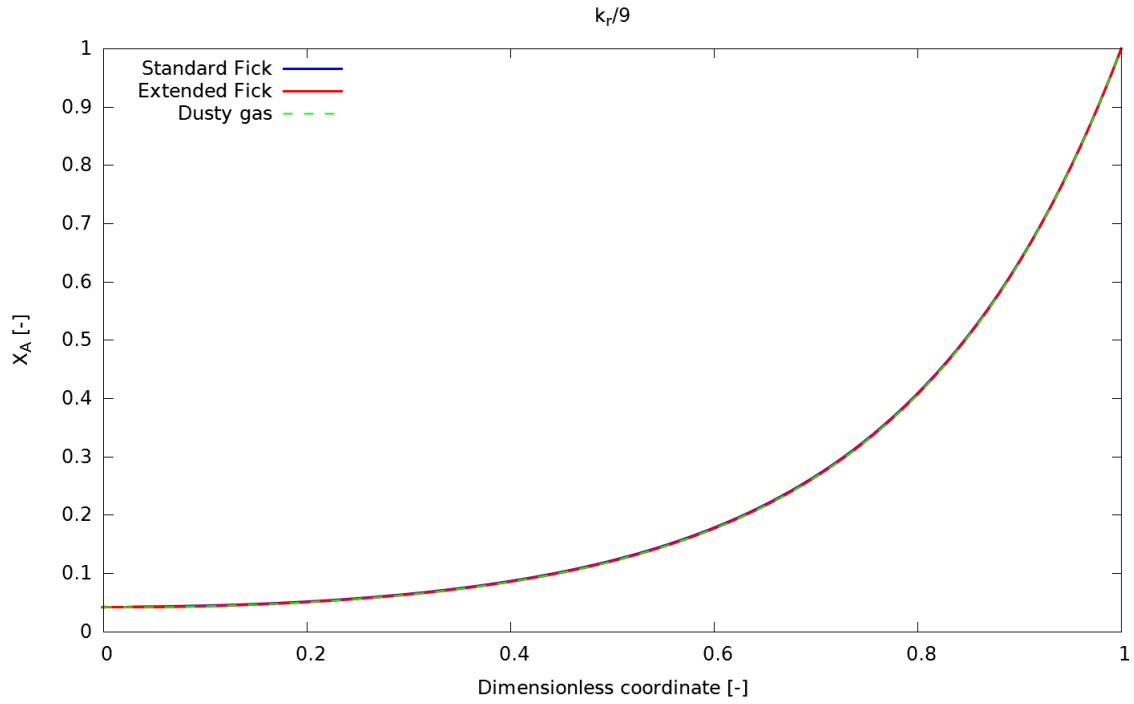

Figure 3.2.8: Species A mole fraction profile in equimolar reaction. The reference value for the kinetic constant k_r has been divided by 9 to shift the regime to intermediate

4. effective diffusivities can be computed coupling Bousanquet formula with Blanc law [32]

$$\begin{cases} \mathcal{D}_i^e = \left(\dfrac{1}{\mathcal{D}_{i,m}^e} + \dfrac{1}{\mathcal{D}_{i,K}^e} \right)^{-1} \\ \mathcal{D}_{i,m}^e = \dfrac{1}{(1-x_i)} \displaystyle\sum_{\substack{j=1 \\ j \neq i}}^{n} \mathcal{D}_{ij}^e x_j \end{cases} \tag{3.11}$$

, it turns out that the solution to system (3.10), after summing the two equations, is

$$\begin{cases} N_{2,z} = -N_{1,z} \\ N_{1,z} = -\dfrac{1}{RT} \mathcal{D}_1^e \dfrac{\partial p_1}{\partial z} \end{cases} \tag{3.12}$$

which is the standard Fick formulation for molar fluxes. Therefore they sum up to zero because a binary mixture is involved. This concludes the explanation why there are no differences in the three models. It is useful to point out that, since the reaction rate is a function of the partial pressures of the reactant, equal pressure and mole fraction

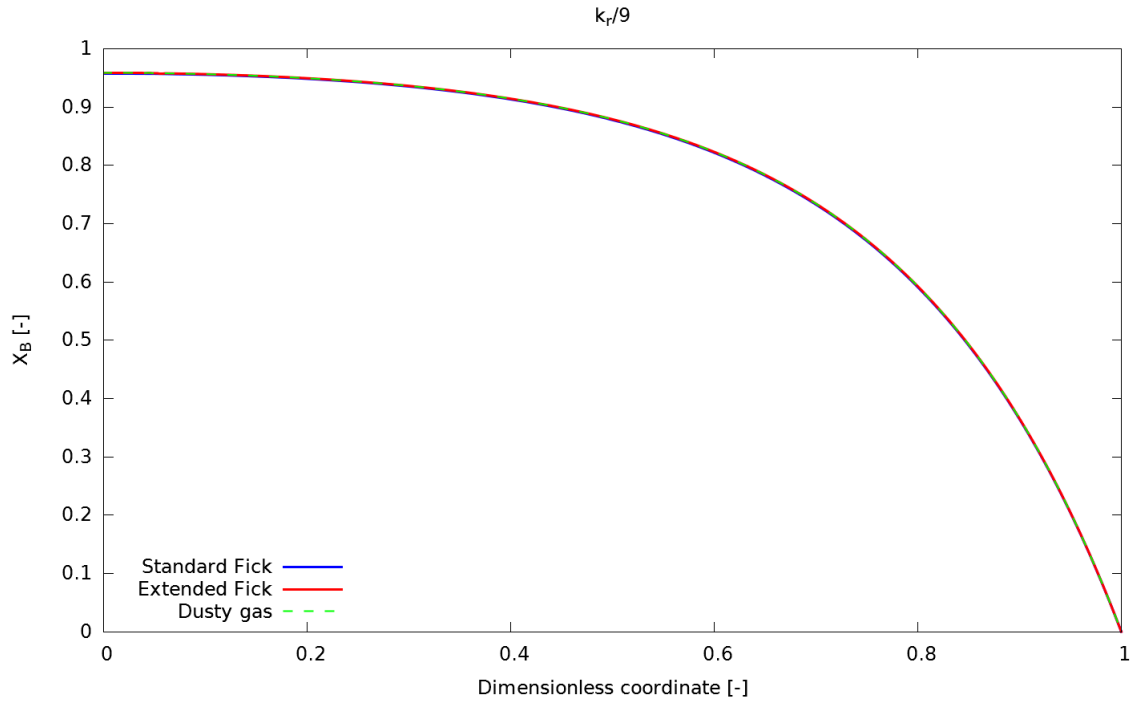

Figure 3.2.9: Species B mole fraction profile in equimolar reaction. The reference value for the kinetic constant k_r has been divided by 9 to shift the regime to intermediate

profiles indicate equal reaction rate and, thus, equal efficiencies evaluated by the three different models. This statement is confirmed by the result shown in Table (3.2.3).

3.2.6 Effects of kinetic constant

The influence of kinetic constant on pressure was checked.

The tests have been conducted on the mole-increasing case using different kinetics constants. A reference value k_r, fixed to 981 s^{-1}, was progressively increased or decreased. In diffusive regime (Figure (3.2.10)), the pressure profile shows a steep gradient near the surface due to the fast reaction and a plateau in the internal zone. Increasing the value of the kinetic constant has little effect (a bigger plateu zone), since the catalyst is already in diffusive regime (see Figure (3.2.10)).

Decreasing the kinetic constant shows how the regime moves from diffusive to intermediate, with a maximum of the pressure profile in the centre of the sphere. In fact, due to reducing the value of k_r, pressure plateau shrinks (see Figure (3.2.11)) more and more until becoming a point and its value starts dropping if the kinetic constant keeps

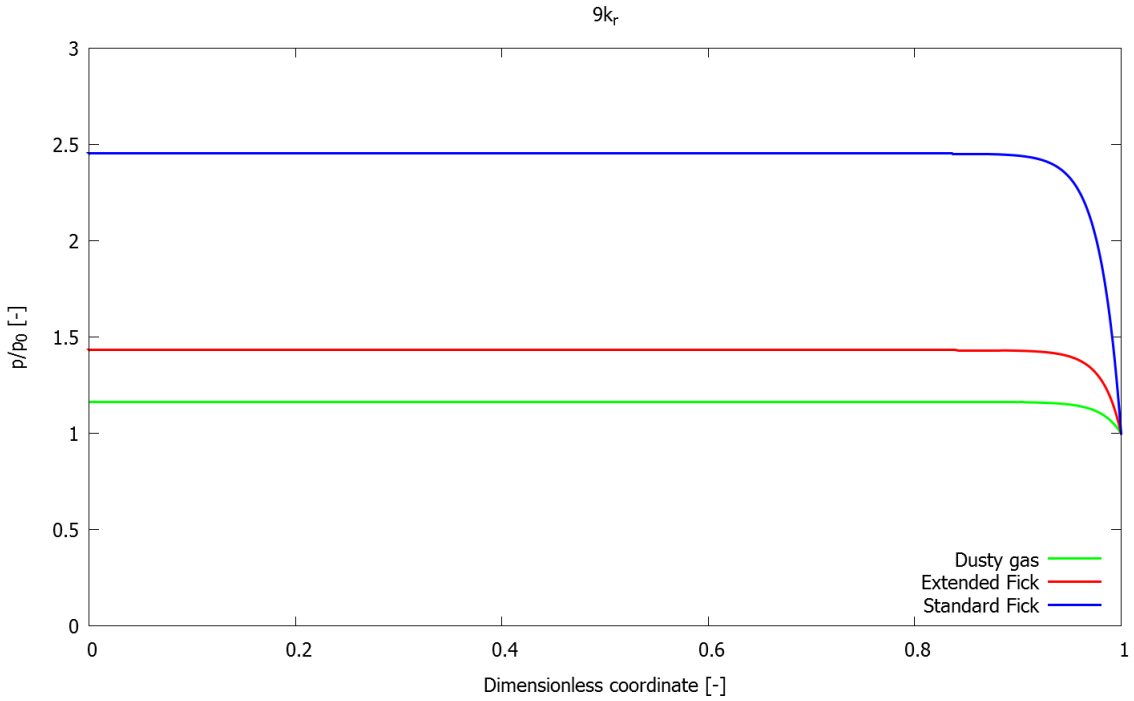

Figure 3.2.10: Pressure ratio with different diffusion models in diffusive regime

decreasing .

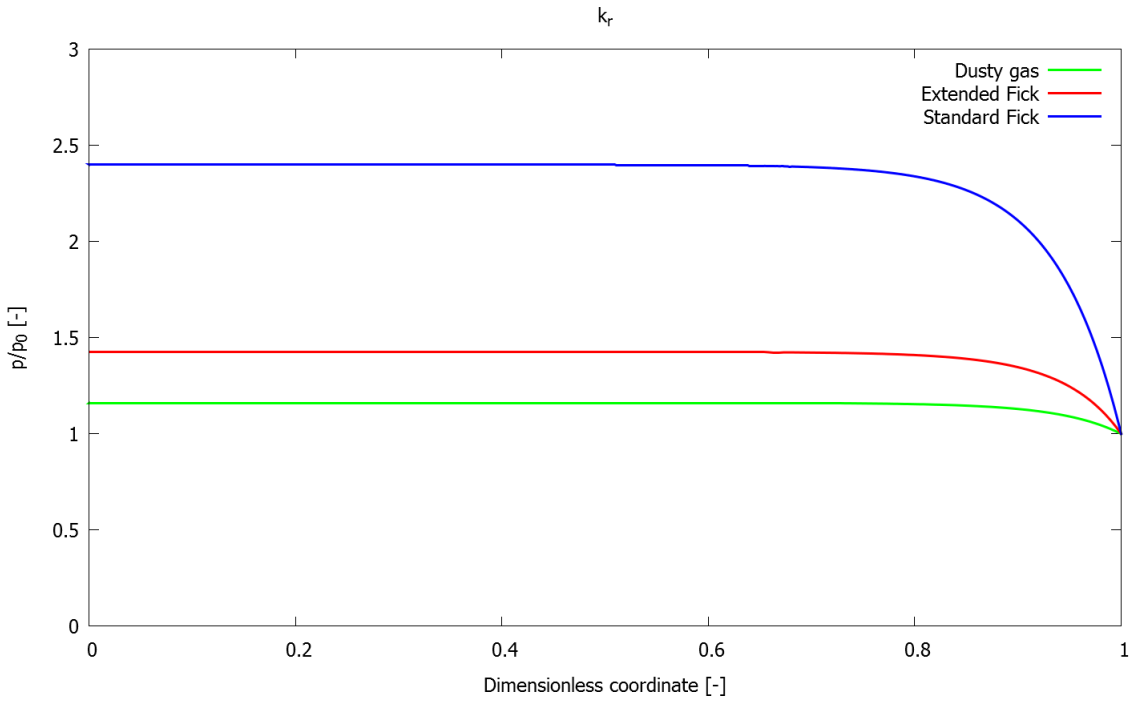

Figure 3.2.11: Pressure ratio with different diffusion models in diffusive regime

With a lower kinetic constant, but still on diffusive regime (Figure 3.2.11), the plateau

is smaller and at a lower value of pressure.

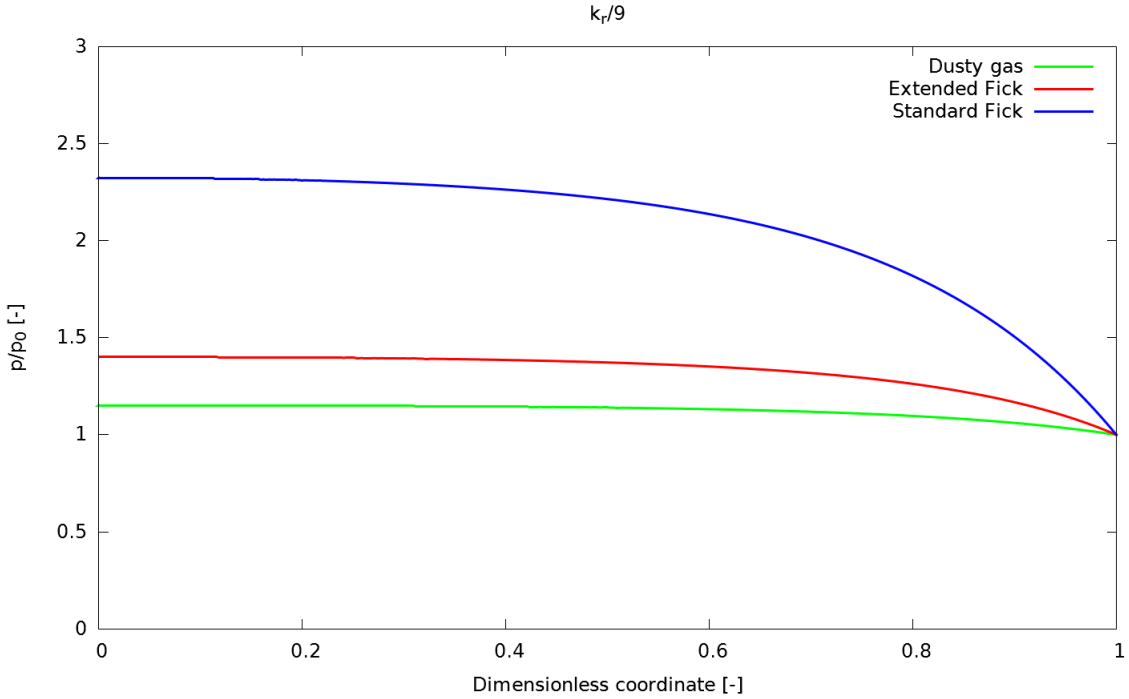

Figure 3.2.12: Pressure ratio with different diffusion models in intermediate reaction

A lower value of k_r (Figure 3.2.12) leads to an intermediate regime where steep gradients are still present but the plateau zone is not. In place of it, a maximum in the profile can be seen.

The difference between the models tends to vanish approaching the chemical regime where diffusion is no longer the limiting step. All the models show a negligible pressure gradient (Figure (3.2.13)).

Therefore, the catalyst efficiency η has been calculated with different kinetic constant using the definition [29]

$$\eta = \frac{\int_V R_A \mathrm{d}V}{R_{A,sup}} \tag{3.13}$$

(see Figure (3.2.14) and Table (3.2.3)).

As numerical strategy for the integral evaluation, the trapezoidal rule has been chosen. Since the spatial domain is a sphere discretized monodimensionally along the radius, in addition to the calculation of reaction rate, the area of the sphere surface had also to be calculated point by point.

Hence, the integral of the discretized function $R_A \cdot A(r)$ between two grid points r_n

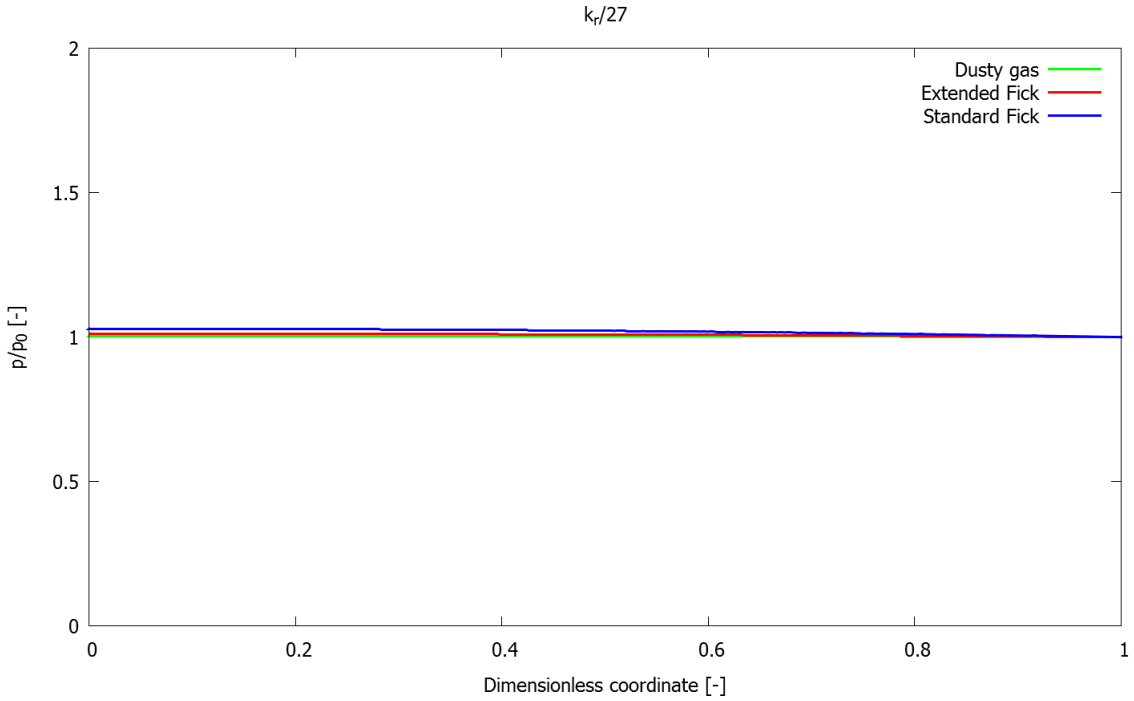

Figure 3.2.13: Pressure ratio with different diffusion models in chemical regime

and r_{n+1} has been approximated with the underlying trapezoid area according to the formula

$$\int_{x_n}^{x_{n+1}} R_A \cdot A(r)\mathrm{d}r \sim \left(\frac{R_{A,n+1} \cdot A_{n+1} + R_{A,n} \cdot A_n}{2} \cdot (x_{n+1} - x_n) \right) \tag{3.14}$$

The total definite integral is then obtained summing the above contributes all over the sphere radius.

Figure (3.2.14) shows the efficiency dropping when the dominant regime shifts from chemical to diffusive regime. The reason why this happens is that only a thin layer of catalyst experiences the reaction in diffusive regime. As expected, the values tend to converge with kinetic constant fall-off while higher differences in intermediate situations can be noticed.

3.2.7 Effects of diffusion coefficients

To test the effect of different diffusivity values, a reaction of the kind

$$3\,\mathrm{A} \longrightarrow 2\,\mathrm{B} \tag{3.15}$$

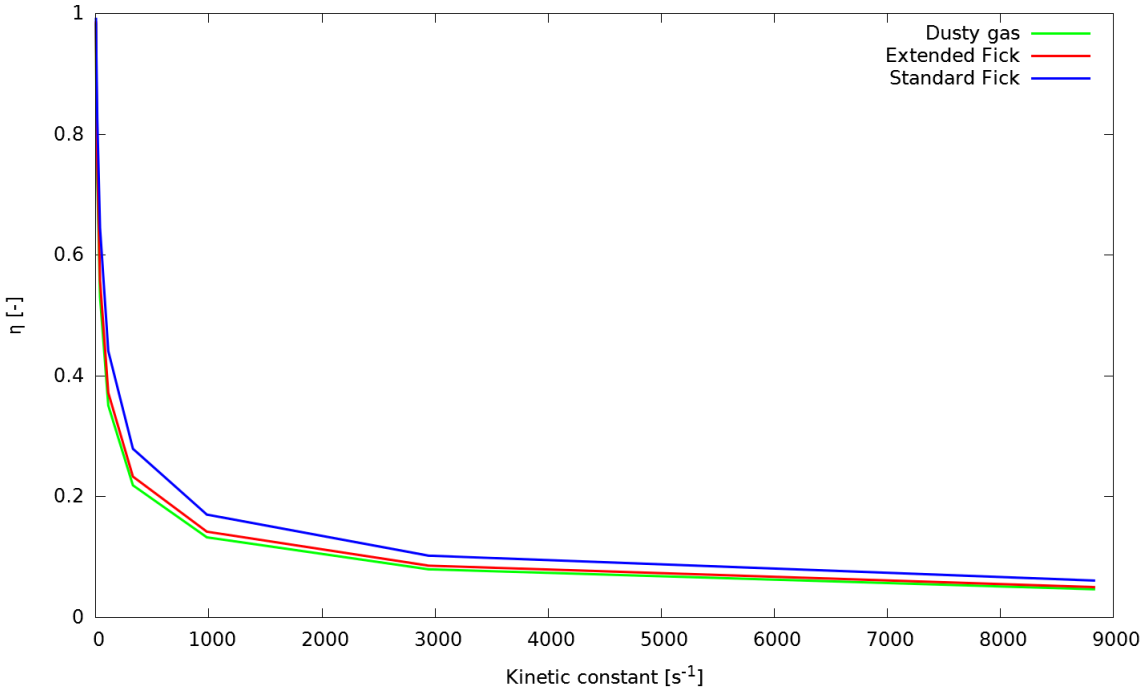

Figure 3.2.14: Catalyst efficiency vs. kinetic constant

$\mathbf{k_r}$	η_{SF}	η_{EF}	η_{DG}
0.448	0.991	0.985	0.982
1.345	0.975	0.957	0.949
4.04	0.930	0.887	0.871
12.11	0.825	0.75	0.723
36.33	0.645	0.558	0.530
109	0.441	0.372	0.351
327	0.279	0.233	0.220
981	0.170	0.142	0.132
2943	0.102	0.0854	0.0794
8829	0.0608	0.0499	0.0463

Table 3.2.3: Efficiency results

with second order reaction rate was used. The kinetic constant was chosen to be $\frac{1}{9}$ of the reference value (981 s^{-1}) and the diffusion coefficient for species A was set equal to the one for O_2 in mixture at 600 K (4.84$\cdot 10^{-4}$ $\frac{m^2}{s}$) and varied in order of magnitude. O_2 was chosen because it can undergo the aforementioned reaction. Therefore, the operating condition data were available from the OpenSMOKE library. Knudsen coefficients, calculated according to the kinetic gas theory

$$\mathcal{D}_{i,K} = \frac{2}{3}\frac{\epsilon}{\tau} r_p \sqrt{\frac{8RT}{\pi M_i}} \tag{3.16}$$

resulted to be $\mathcal{D}_{A,K} = 5.5547 \cdot 10^{-6}$ and $\mathcal{D}_{B,K} = 1.3606 \cdot 10^{-6}$.

As expected, a lower diffusion coefficient makes the catalyst work in diffusive regime which implies steeper internal mole fraction gradients. An opposite trend is shown by the pressure gradients: this happens because a small diffusion coefficient causes the product to take a lot of time to leave the catalityc media and the reactant to enter slowly. Thus, the extreme case shows no pressure gradient and a sphere filled with product. However this can only be noticed using extended Fick and dusty gas models, since the pressure gradient related to reaction can be quickly eliminated by the viscous flow, which does not depend on the diffusion coefficient.

This comparisons highlights again that the standard Fick model overestimates the pressure gradient with respect to the extended Fick model, which in turn shows similar behavior to the dusty gas formulation. Diffusivity values used are indicated in plot legends. Referring to Equation (3.11)

$$\mathcal{D}_i = \frac{\mathcal{D}_{ij} \cdot \mathcal{D}_{i,K}}{\mathcal{D}_{ij} + \mathcal{D}_{i,K}}$$

alternatively rewritten as

$$\mathcal{D}_i = \frac{\mathcal{D}_{ij}}{\frac{\mathcal{D}_{ij}}{\mathcal{D}_{i,K}} + 1}$$

When the material diffusivity is far higher than Knudsen diffusivity, $\mathcal{D}_i \sim \mathcal{D}_{i,K}$. In the opposite situation, $\mathcal{D}_i \sim \mathcal{D}_{ij}$. In intermediate situations (in this test order of magnitude 10^{-6} for both), $\mathcal{D}_i$ shares the same order of magnitude of $\mathcal{D}_{ij}$ and $\mathcal{D}_{i,K}$. This fact is important to explain why the profiles are all the same for high material diffusivities, only tiny variations can be noticed when $\mathcal{D}_{i,K}$ and $\mathcal{D}_{ij}$ are similar and big differences can be

noticed for smaller $\mathcal{D}_{ij}$ values (see Figure (3.2.15), (3.2.16) and (3.2.17).

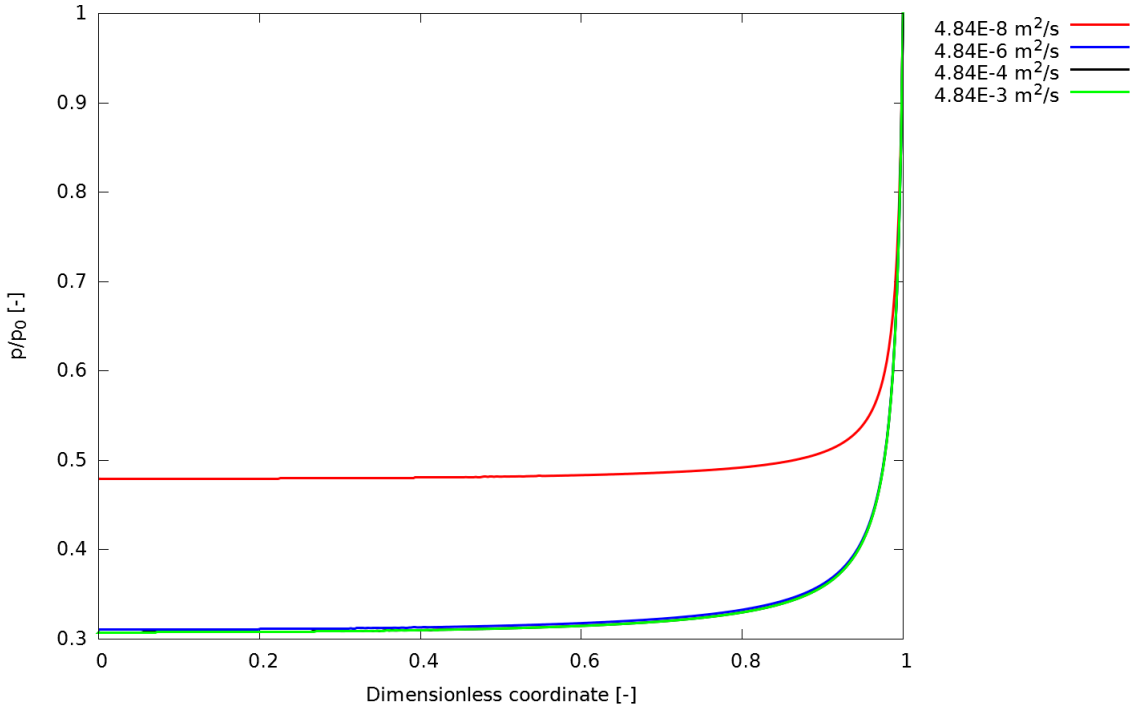

Figure 3.2.15: Standard Fick model, pressure profile

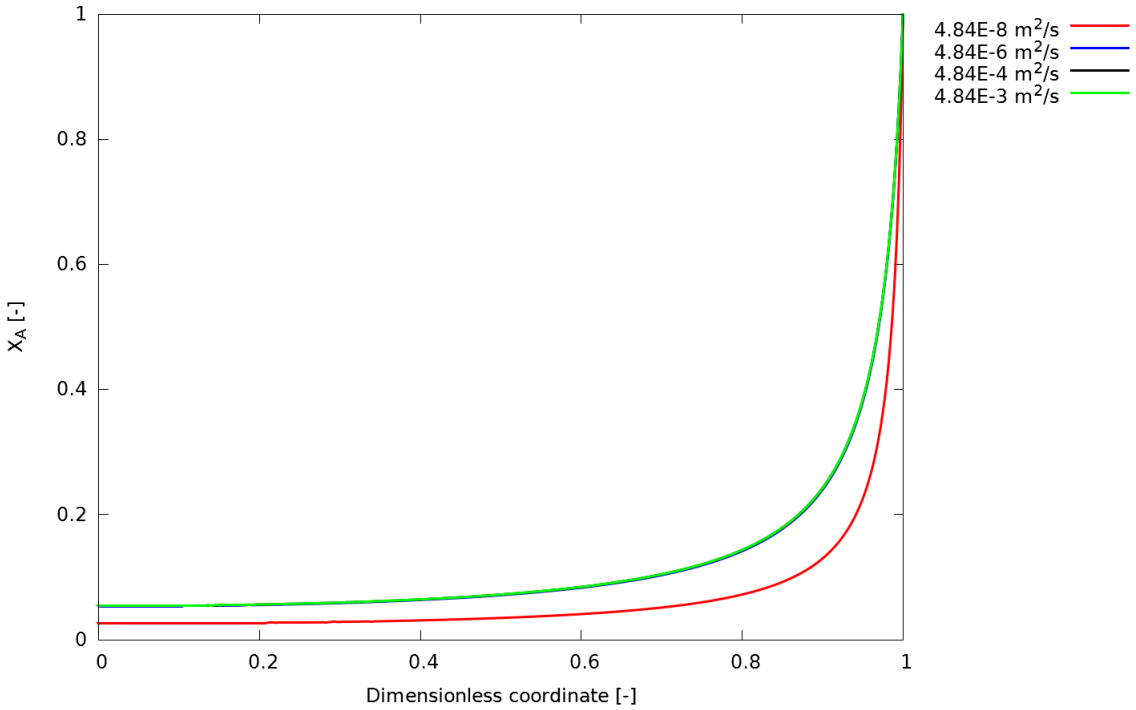

Figure 3.2.16: Standard Fick model, species A mole fraction

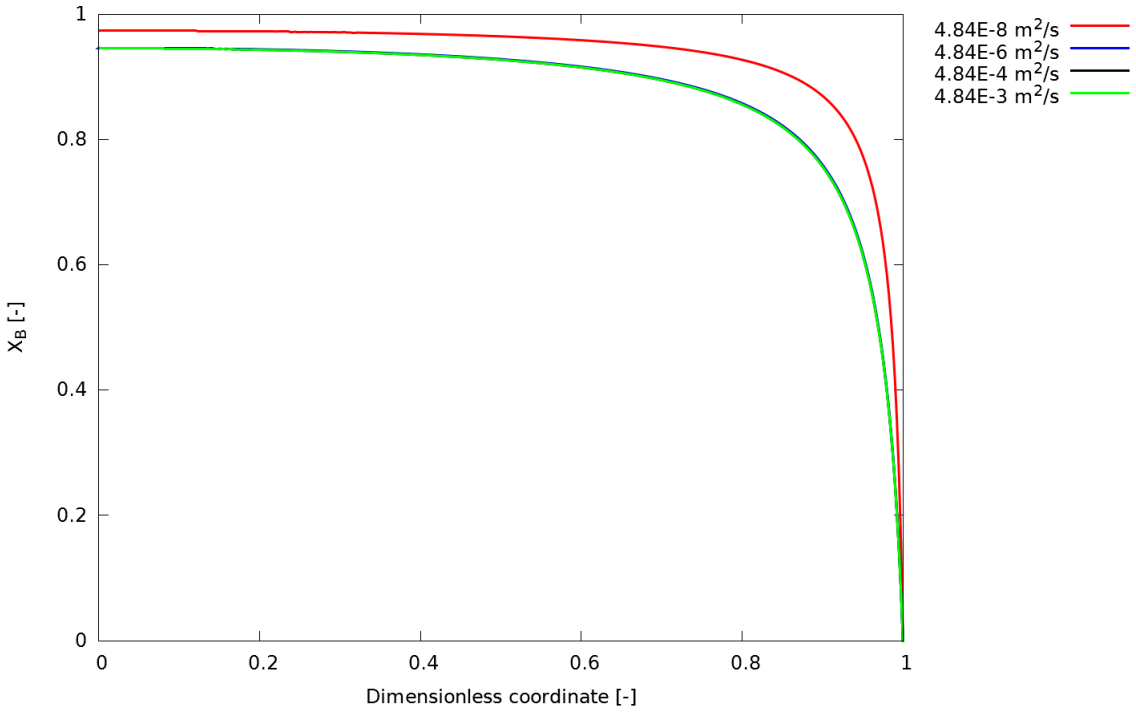

Figure 3.2.17: Standard Fick model, species B mole fraction

It can be noticed as standard Fick modelization shows analogous profiles in case of diffusivity order of magnitude higher than 10^{-6}. Regarding extended Fick model, decreasing the order of magnitude of diffusivity leads the pressure gradients to vanish since the viscous flow is not affected by this variation but less product is allowed to leave the catalytic media (see Figure (3.2.18). According to the previous reason, on unsteady state the reaction rate is limited by the product that saturates the sphere more and more while the pressure gradients is diminished by the viscous flow.

A lower $\mathcal{D}$ shifts the regime to diffusive so steeper gradients arise also because the higher pressure enhances the reaction rate (see Figure (3.2.19) and (3.2.20)).

Regarding pressure (Figure (3.2.21)), the dusty gas model shows the same effects aforementioned for the extended Fick one. The pressure gradient approaches zero sooner because drag effects cause less reactant income. Focusing on mole fraction (Figure (3.2.22) and (3.2.23)) instead, the dusty gas gradients, although showing analogous behaviour with $\mathcal{D}$ than extended Fick ones, are steeper since the drag of the product leaving the media has a noticeable effect on such a low reactant inlet flux.

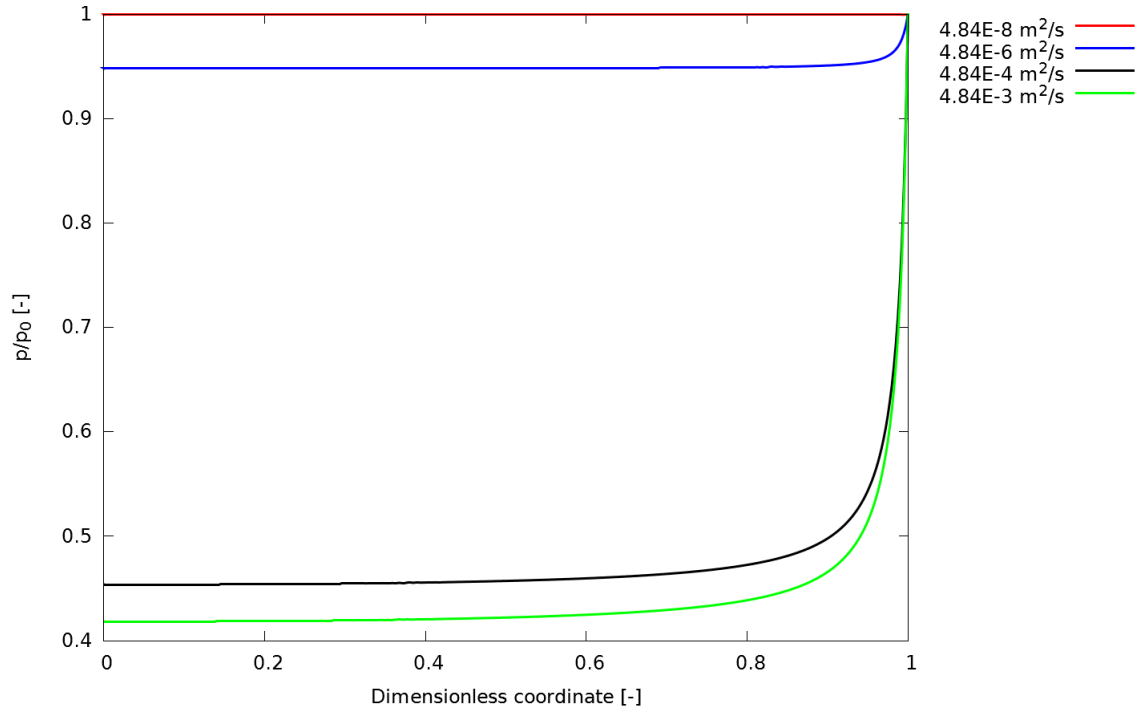

Figure 3.2.18: Extended Fick model, pressure profile

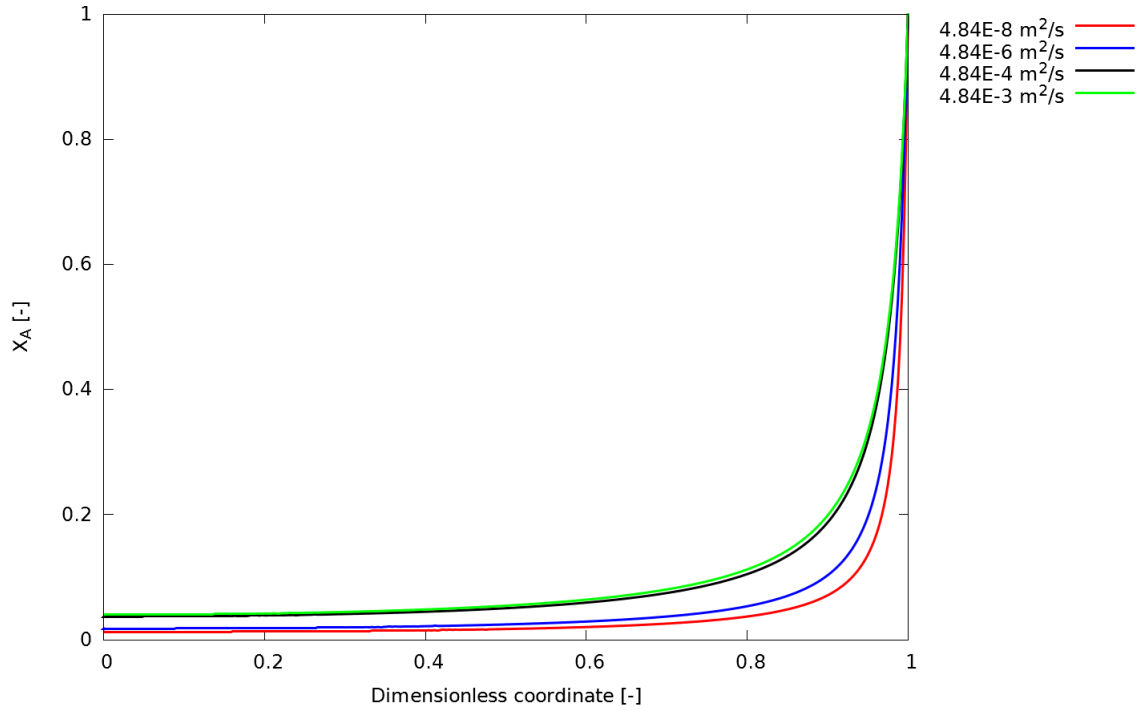

Figure 3.2.19: Extended Fick model, species A mole fraction

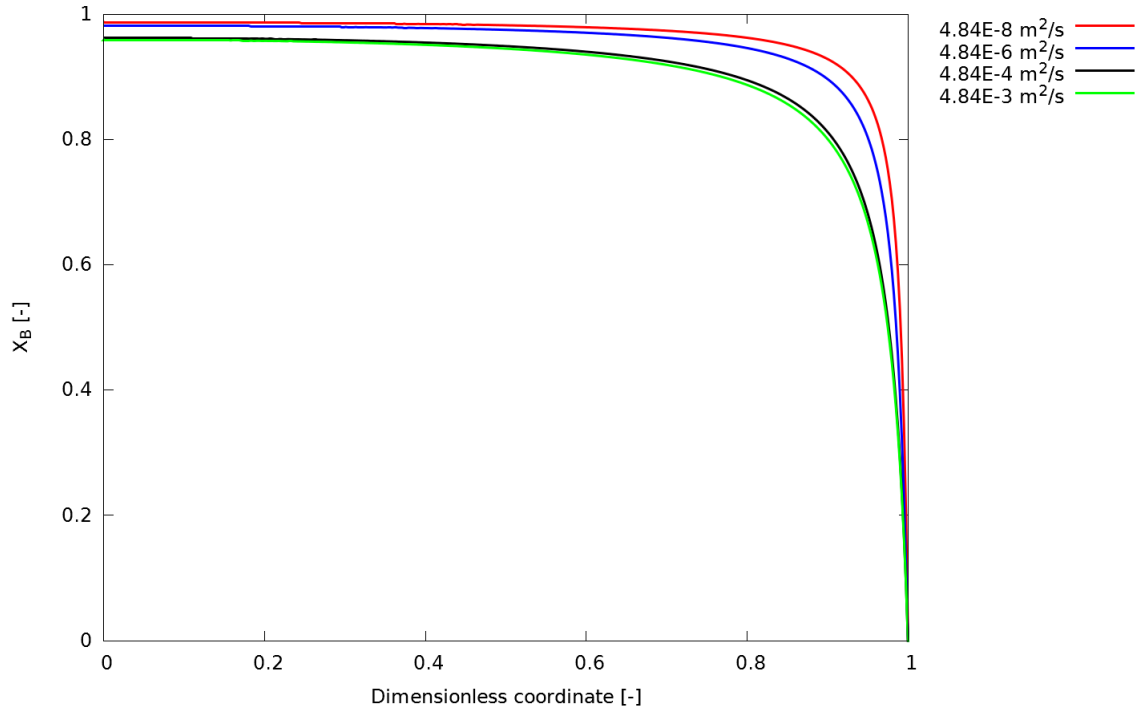

Figure 3.2.20: Extended Fick model, species B mole fraction

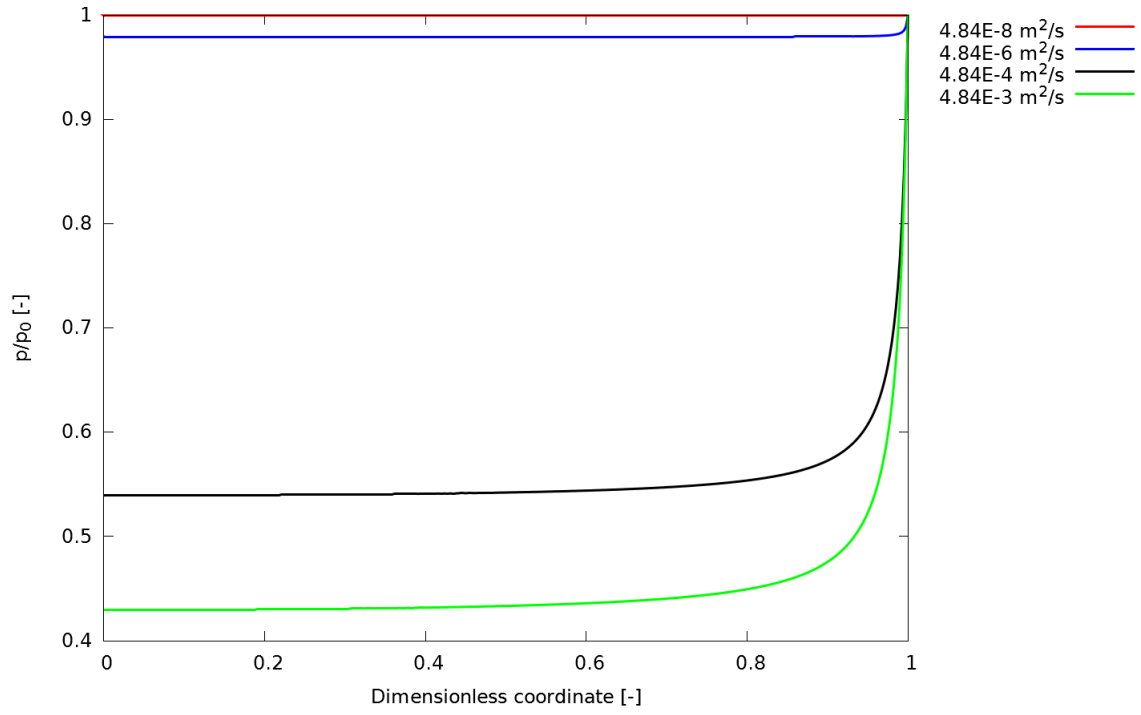

Figure 3.2.21: Dusty gas model, pressure profile

3.2.8 Effect of stoichiometric ratio on efficiency estimation

Further tests were carried out to analyze the effect of stoichiometry on catalyst efficiency.

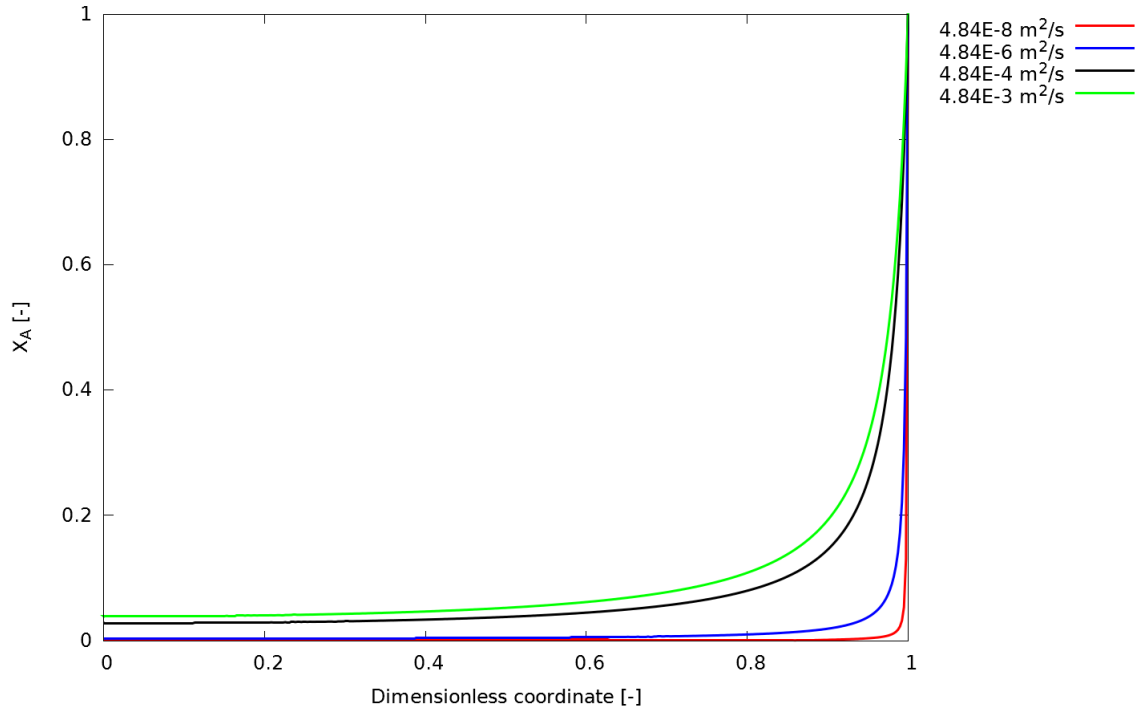

Figure 3.2.22: Dusty gas model, species A mole fraction

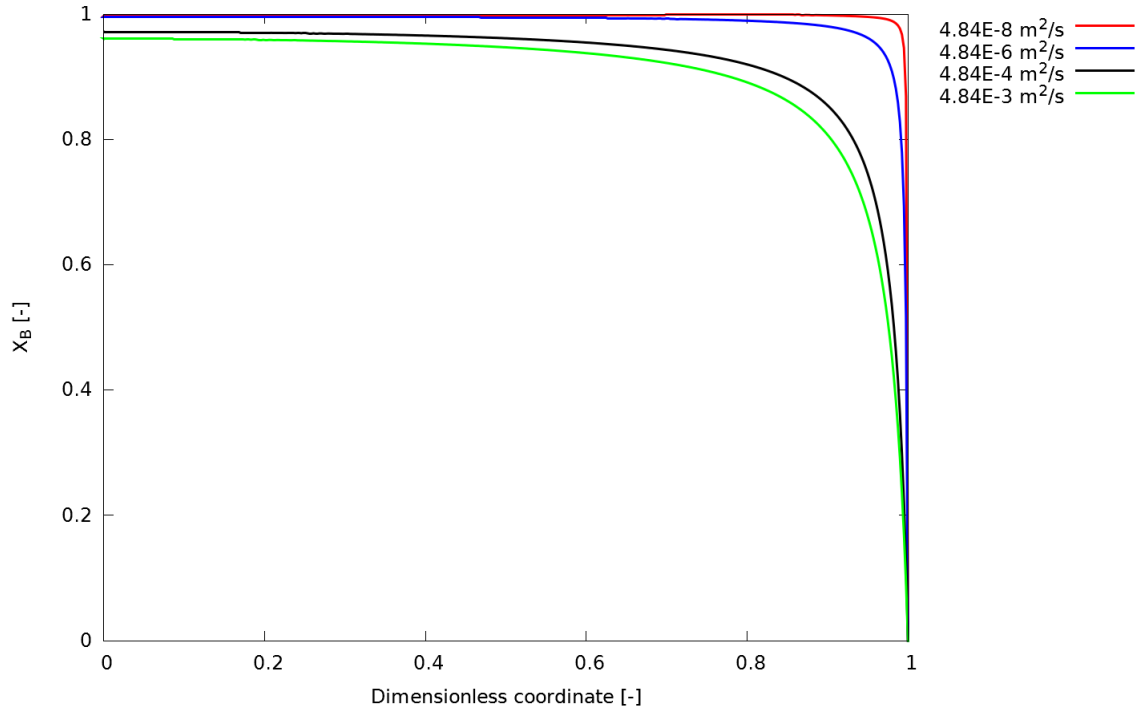

Figure 3.2.23: Dusty gas model, species B mole fraction

To allow comparisons between different conditions, a first order reaction rate and a fixed kinetic constant (109 s^{-1}) were used. The chemical reaction coefficients were

divided by the reactant one to grant equal effects of the same kinetic constant value. It can be noticed in Figure (3.2.24) that increasing the stoichiometric coefficient ratio causes the efficiency to drop. This is due to the fact that the pressure profile values grow proportionally with the stoichiometry ratio, as seen in Figure (3.2.25) and, thus, the reaction rate since it depends on the partial pressures.

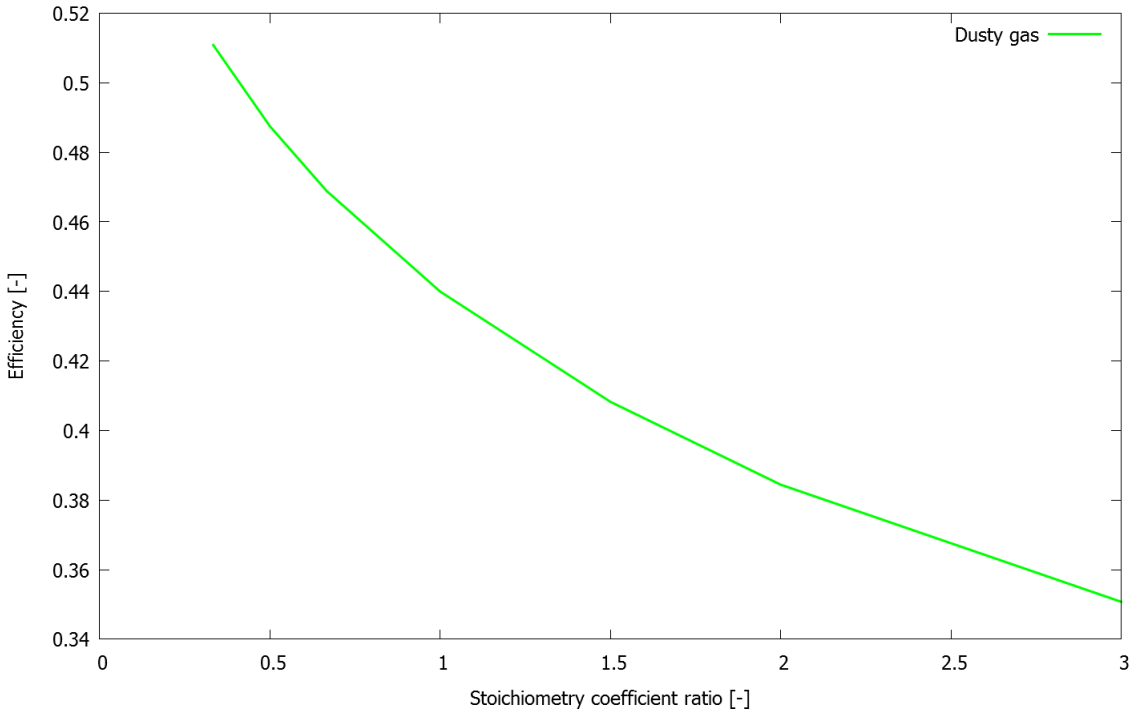

Figure 3.2.24: Catalyst efficiency as a function of stoichiometric coefficient ratio

In Figure (3.2.26), it can be noticed that a higher reaction rate due to higher pressure implies a lower reactant mole fraction.

3.2.9 Results and convergence analysis

Both the standard and the extended Fick model predicted different pressure over the catalyst particle than the dusty gas model, with a remarkable difference for the standard model.

This is due to the fact that pressure is increasing because of the non-equimolar chemical reaction inside the catalyst particle but the boost to back diffusion given by the pressure gradient is not accounted in the standard Fick formulation so the net flux going out of the particle is low and internal pressure rises. The inclusion of pressure gradient

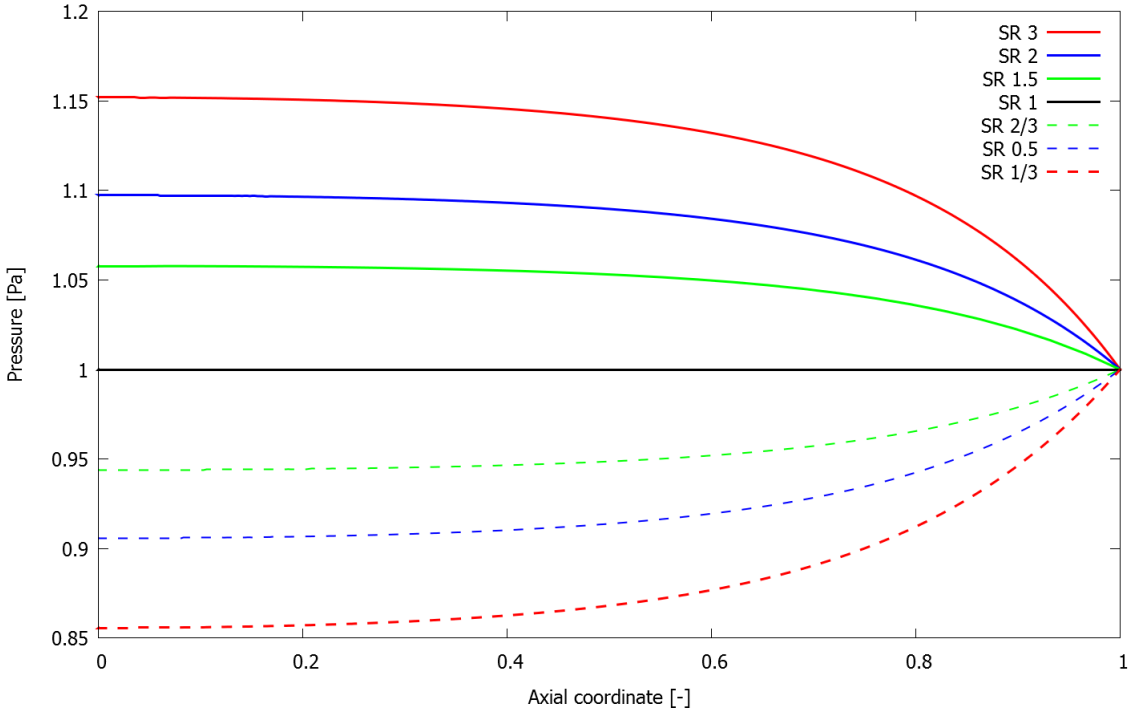

Figure 3.2.25: Pressure as a function of stoichiometric coefficient ratio

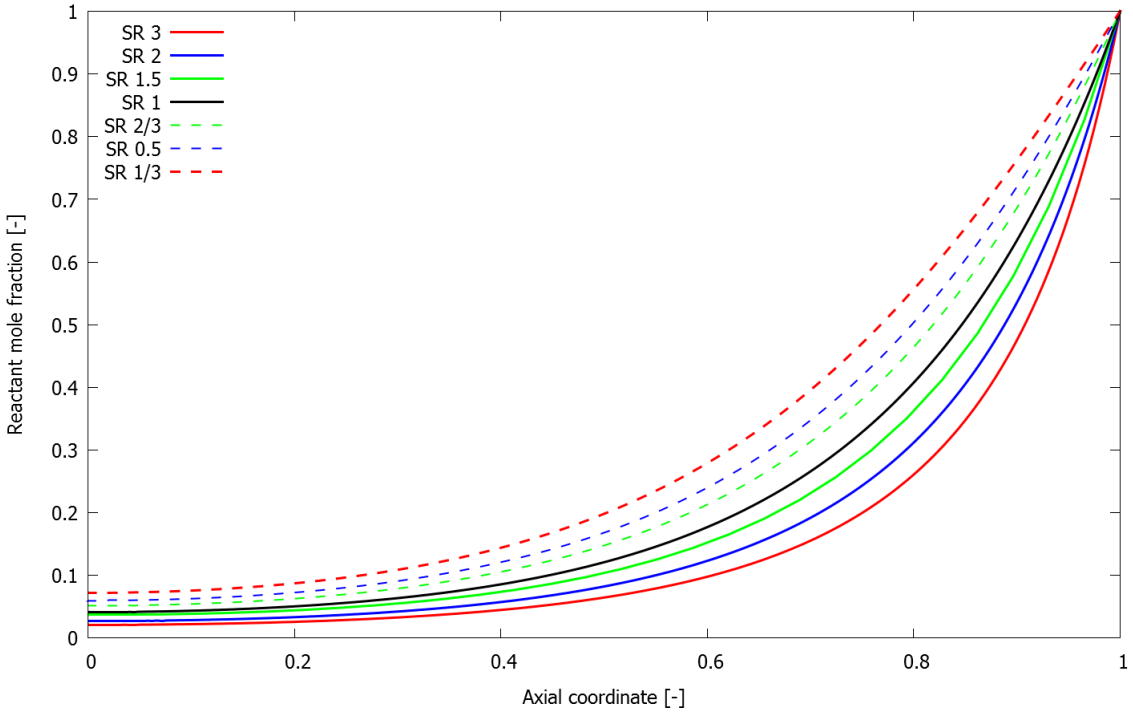

Figure 3.2.26: Reactant mole fraction as a function of stoichiometric coefficient ratio

into the molar flux definition like results in considerably lower values of maximum pressure while the dusty gas model yields to the lowest pressure value as it accounts

mutual drag too.

Mole fraction profiles reflect the above statement as the standard Fick model shows an higher fraction of product since a major partial pressure for reagents implies an enhanced reaction rate.

The profiles for the extended Fick and the dusty gas models are almost identical, like stated by Veldsink [31]. This is a clear signal that the local partial pressures resulting from both models are different.

To verify the indipendency by the number of grid points chosen, and thus ensure the correctness of the solutions, convergence tests have been carried out for each different simulation. The minimum number of points, that grants independency of the variable profiles by itself, is the lowest one that can be used.

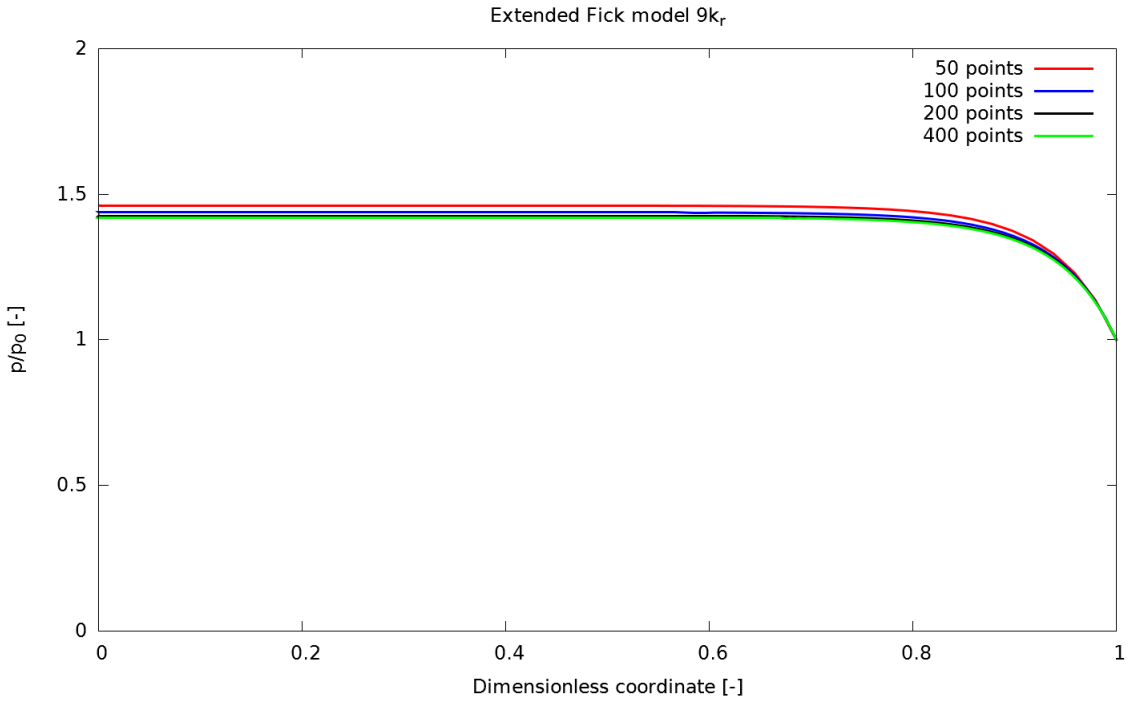

Figure 3.2.27: Example of numerical convergence. Solution profiles stop changing when a treshold value of spatial points is reached

Figure (3.2.27) is a sample of the convergence analysis made.

3.3 Conclusions

In this chapter, numerical simulations to solve unsteady diffusion with reaction problems coupled with the dusty gas model have been carried out. In addition, differences with two formulations of Fick law have been investigated and discussed. Simulations involving non-equimolar chemical reactions pointed out how Fick models overestimate the pressure gradient with the worst estimation obtained by the standard Fick model. However, it was also noticed as the mole fraction profiles does not appear so different between each model in the majority of the cases. This allow to use the standard Fick solution to obtain a good result approximation in situations where pressure gauge is not considered important. It was also noticed as, in equimolar binary reactions, the profiles obtained from the three models show no difference at all. Therefore, since the major differences are due to pressure variations, in equimolar cases the profiles should always be similar. Furthermore, the three models give very similar results in case of diffusive regime so Fick applications can be sufficiently accurate thus avoiding severe complexity and long duration of the simulations.

Chapter 4

Implementation of the dusty gas model in catalyticFOAM

In this chapter catalyticFOAM, a computational fluid dynamics code for homogeneous and heterogeneous gas/solid reactions, the solvers herein implemented and a detailed description of their mathematical approach are presented. Therefore, the implementation of the dusty gas model in a C++ dedicated class and the subsequent insertion into the catalyticFOAM framework is discussed.

4.1 General overview

catalyticFOAM is a computational fluid dynamics code developed to investigate the interactions between fluid dynamics and chemistry in heterogeneous catalytic reactors following a "first principle approach" [13]. The development of this code relies heavily on OpenFOAM®, a free, open source computational fluid dynamics framework capable to solve several different systems dealing with many areas of applied mathematics.

catalyticFOAM solvers come in two different versions

- catalyticFOAM standard [13] able to simulate complex reacting flows in conjuction with detailed microkinetic scheme to describe surface reactivity. The major drawback is the inability in predicting the diffusion phenomenona inside the catalyst as the description of the solid region is neglected.

- catalyticFOAM multiRegion [5] [12] which overcomes the limitations regarding the solid region by introducing a multi-region structure to account for fluid and solid phase simultaneously. Heterogeneous reactions occur in the whole solid volume and not only at the surface.

4.1.1 The operator splitting technique

These solvers implement the operator splitting technique [6], suited for the numerical computation of reactive flows. This particular algorithm splits the equations governing the reaction-diffusion phenomenon into two groups which are integrated separately and sequentially. The splitting is based on the degree of linearity and stiffness for each term involved. The great advantage of the operator splitting is the targeted use of the best technique to solve each term efficiently and then combine each step to reach an accurate solution of the original problem.

After spatial discretization, the transport equations of species mass fractions and energy can be written in the following, general form

$$\frac{\partial \mathbf{\Psi}}{\partial t} = \mathbf{M}(\mathbf{\Psi}, t) + \mathbf{S}(\mathbf{\Psi}) \tag{4.1}$$

where $\mathbf{\Psi}$ is the vector of dependent variables (mass fractions and temperature), $\mathbf{S}(\mathbf{\Psi})$ is the vector of rates of change of $\mathbf{\Psi}$ due to chemical reactions and $\mathbf{M}(\mathbf{\Psi}, t)$ is the vector or rates of change of $\mathbf{\Psi}$ due to transport processes. $\mathbf{M}(\mathbf{\Psi}, t)$ presents low stiffness and quasi linearity while $\mathbf{\Psi}$ is highly nonlinear and stiff due to the very broad timescales range of the reacting phenomena. The splitting scheme applied in the solvers is based on staggered time step approach, whose details are reported in previous works [12]. This method separates the terms of the equation in two different systems of equations, (*N+1*) PDEs given by *N* (number of species) diffusion and convection terms and one terms for the energy balance and *NC* (number of cells) indipendent ODEs systems obtained from the reactive term, as shown in Equation (4.2)

$$\begin{cases} \dfrac{\partial \mathbf{\Psi}_1}{\partial t} = \mathbf{M}(\mathbf{\Psi}_1, t) \\ \dfrac{\partial \mathbf{\Psi}_2}{\partial t} = \mathbf{S}(\mathbf{\Psi}_2) \end{cases} \tag{4.2}$$

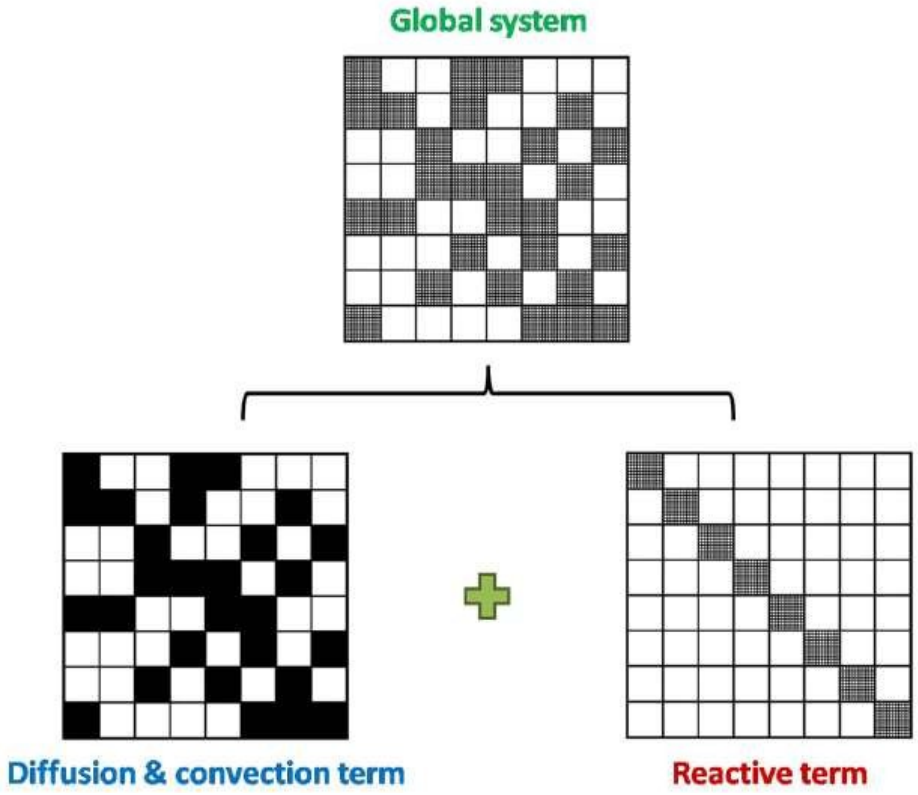

Figure 4.1.1: Jacobian matrix of PDEs and ODEs systems

The Jacobian matrix of the global system has the dimension of $N_c \times N_u$ where N_c is the number of computational cells and N_u the number of unknowns (species and temperature). Therefore, it is unstructured and sparse [13]. The Jacobian matrix associated to the PDEs is unstructured and sparse while the one associated to the reactive step is a diagonal block matrix, as shown in Figure (4.1.1) [12]. Indeed, the rate of production in each cell depends only on the conditions of the cell itself. This implies that the PDEs system can be turned into a group of decoupled ODEs systems. The resulting numerical problem consists of a system of weakly nonlinear PDEs and a group of nonlinear ODEs systems. The numerical solution for the stiff, nonlinear ODEs systems representing the reaction step is demanding in terms of computational effort, while solving transport and diffusion terms is performed smoothly. The level of detail of the kinetic scheme has great influence on the required computational time as the dimension of the system is proportional to the number of species involved.

4.1.2 Definition of mass fluxes

In the current release of catalyticFOAM, the transport equation are based upon Fick law, but a corrected expression of the Fickian flux is used to obtain no pressure gradient inside the porous media.

First the material fluxes are calculated for each species

$$\mathbf{J_i} = -\mathcal{D}_i^e \nabla \rho_\mathbf{i} \tag{4.3}$$

then their sum is saved as a *correction factor*

$$\mathbf{J_c} = -\sum_{i=1}^{n} \mathbf{J_i} \tag{4.4}$$

The real flux for the ith species is a linear combination of Equations (4.3) and (4.4)

$$\mathbf{J_{i,r}} = \mathbf{J_i} + \omega_i \mathbf{J_c} \tag{4.5}$$

where the correction factor is weighted on the corresponding mass fraction. The zero sum for fluxes follows immediately as

$$\begin{aligned} \sum_{i=1}^{n} \mathbf{J_{i,r}} &= \sum_{i=1}^{n} \mathbf{J_i} - \sum_{i=1}^{n} \omega_i \sum_{i=1}^{n} \mathbf{J_i} \\ \sum_{i=1}^{n} \mathbf{J_{i,r}} &= \sum_{i=1}^{n} \mathbf{J_i} \left(1 - \sum_{i=1}^{n} \omega_i \right) = \mathbf{0} \end{aligned} \tag{4.6}$$

This methodology implicitly states that density and pressure must be constant. Being the transport equation

$$\frac{\partial \rho_i}{\partial t} = -\nabla \cdot \mathbf{J_{i,r}} \tag{4.7}$$

and recalling that $\rho = \sum_{i=1}^{n} \rho_i$, a summation all over the species in Equation (4.7) yields to

$$\frac{\partial \rho}{\partial t} = -\sum_{i=1}^{n} \nabla \cdot \mathbf{J_{i,r}} = 0 \tag{4.8}$$

which proves the thesis.

4.1.3 The PIMPLE loop at interphase surface

Focusing on catalyticFOAM multiRegion, the numerical methodology was based on a segregated approach for physical coupling of neighboring regions, involving the solution of the governing equations on each domain and the achievement of the convergence on the boundary conditions interface through an iterative loop called PIMPLE loop.

The iterative procedure begins with the solution of the governing equations for the fluid region. According to the operator splitting technique, the reactive term has been separated by the transport term. First of all, the heat and mass transport equations of each species are solved imposing the boundary conditions of the fluid side. Then the homogeneous reactions are solved. At this moment, the PISO (**P**ressure **I**mplicit with **S**plitting of **O**perator) loop starts: the Navier-Stokes and the continuity equations are solved and the velocity field is corrected explicitly (see Figure (4.1.2)). Once the solid side boundary conditions are updated, the solution of the equations in the solid region follows the same approach already used for the fluid domain. The mass and energy transport equations are solved and the side fluid interface values are updated. Once the convergence criteria are satisfied, the ODE system of the heterogeneous reactions is solved. The whole procedure is iterated till the reaching of the end time.

4.2 Inclusion of the dusty gas model into catalyticFOAM

4.2.1 General overview

The dusty gas formulation does not allow to express the material fluxes directly, in contrast to the Fickian approach. Due to this issue, the numerical routine dedicated to solving transport phenomena had to be rewritten to define these fluxes, given the properties of the system (temperature, pressure, etc.) for each time and domain cell. The set of equations for diffusion had to be rewritten in a general way since it was created to work specifically with Fick law. Furthermore, it did not take into account possible pressure variations so an equation for this particular unknown was missing. A direct consequence is the need of reaching convergence for pressure at the interphase surface, which implies a modification of the PIMPLE loop.

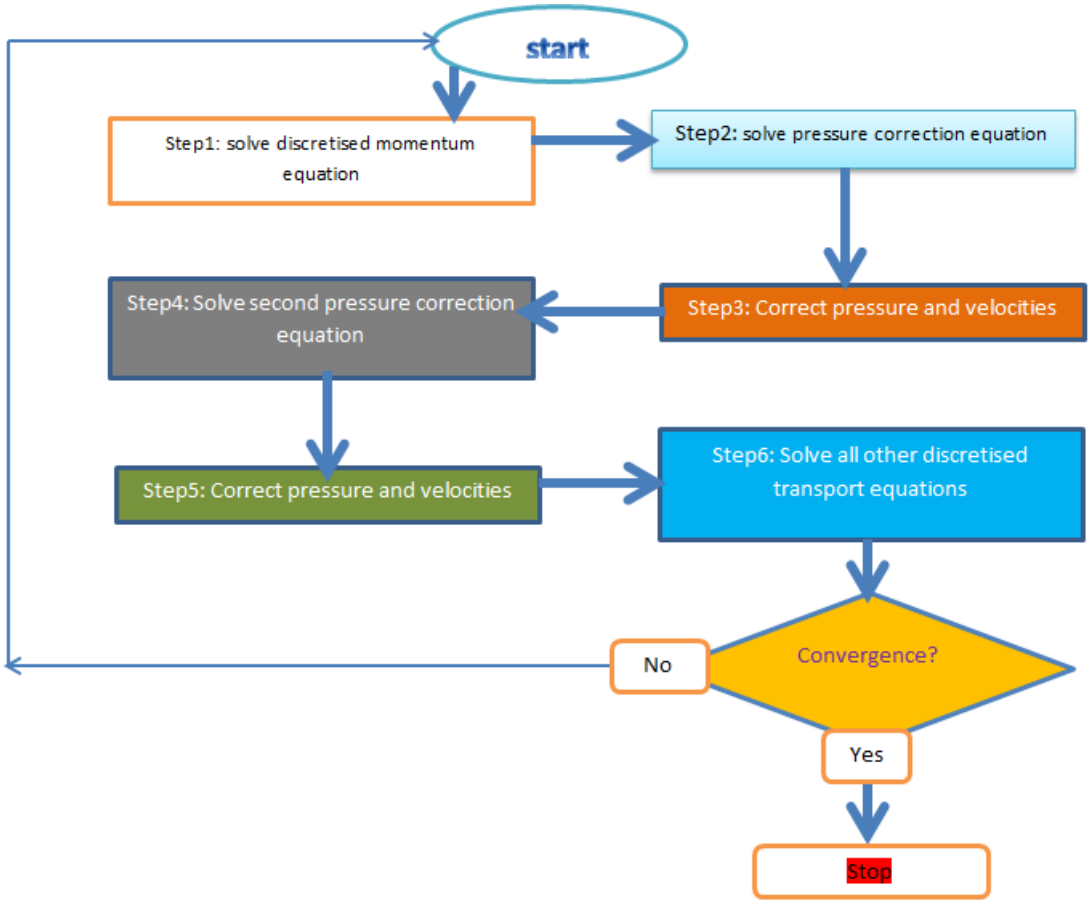

Figure 4.1.2: PISO loop

In the following, each aspect (fluxes definition, transport equations, PIMPLE loop) is individually described.

4.2.2 The *dustyGas* class

The entire numerical routine dedicated to the solution of the linear system (2.39) in conjuction with the existing catalyticFOAM layer was coded, following the principles of object oriented programming, into a C++ class named *dustyGas*. This class comes with many built-in methods whose purpose is both retrieving the information needed to build the coefficient matrix $\mathbf{A}$ (see Equation (2.39) and effectively solving the linear system returning the molar fluxes $\mathbf{N_i}$. The interconnection between OpenFOAM® and *dustyGas* is shown in Figure (4.2.1). OpenFOAM® relies on the OpenSMOKE++ libraries to calculate thermochemical properties, temperature, pressure, mass fractions etc. in each cell of integration domain. These data are then passed to *dustyGas* class which accomplishes the calculation of molar fluxes and returns them to the OpenFOAM® routines for solving the PDE. Once the PDE has been solved for the current time step the entire procedure is repeated in a cyclical manner.

Here a brief description of class methods:

1. *dustyGas*: the default class constructor. This class method creates the object *dustyGas* via the mandatory linking to OpenSMOKE++ libraries.

2. ∼*dustyGas*: the default class destructor. This class method deallocates the memory used by *dustyGas*.

3. *setMassFractions*: this class method reads the current vector of mass fractions and assigns it to the corresponding private variable within the class. It calculates mole fractions values simultaneously.

4. *setGradients*: this class method reads the current gradients for mole fractions and pressure and assigns them to the corresponding private variables within the class.

5. *setCatalystProperties*: this class method reads the properties regarding the catalyst solid matrix (porosity, tortuosity and pore radius) and sets the corresponding

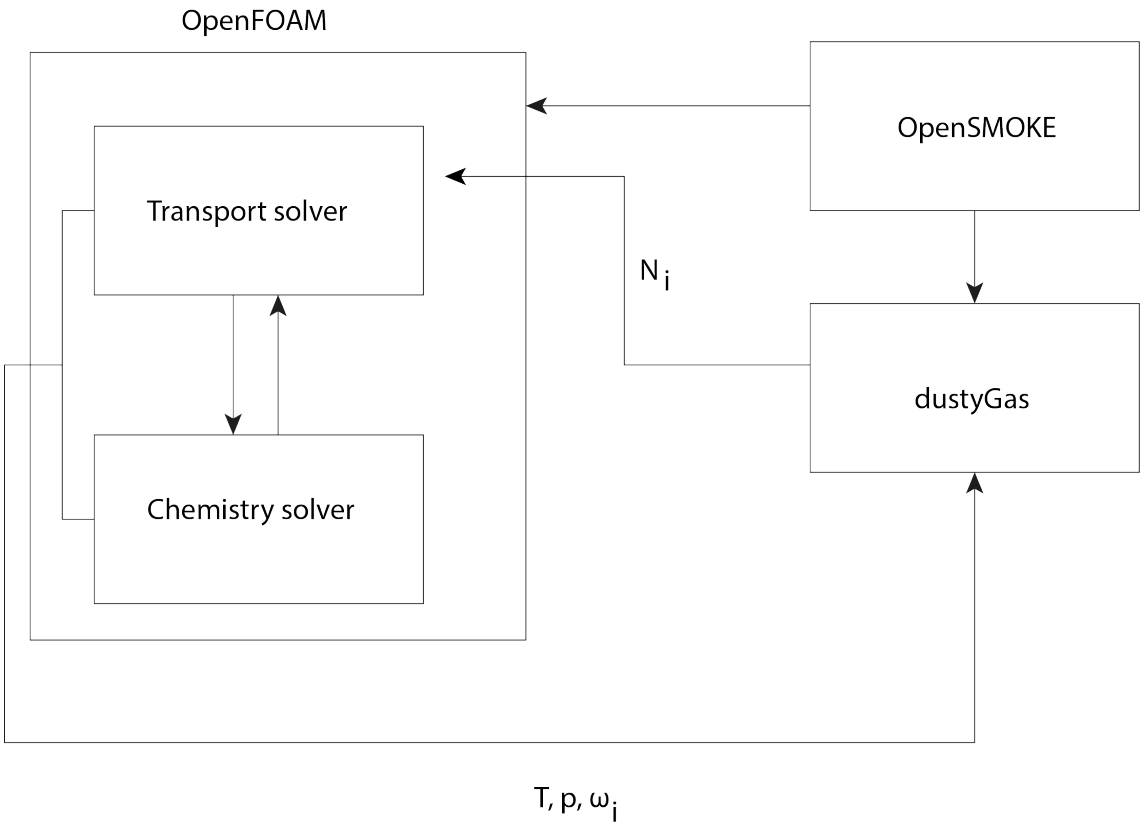

Figure 4.2.1: Interconnection between OpenFOAM® and *dustyGas*

private variables within the class.

6. *setPermeability*: this class method calculates the permeability coefficient B_0 once the solid properties are known.

7. *setKnudsenCoefficient*: this class method calculates the Knudsen coefficient once the solid properties are known.

8. *setTemperature*: this class method reads the current temperature value and set the corresponding private variable within the class.

9. *setPressure*: this class method reads the current pressure value and set the corresponding private variable within the class.

10. *setDynamicViscosity*: this class method calculates the mixture dynamic viscosity μ exploiting the OpenSMOKE library.

11. *getGammaBinary*: this class method calculates the mutual diffusivities $\mathcal{D}_{ij}$ for

every chemical species exploiting the OpenSMOKE library.

12. *calculateKnudsenDiffusionCoefficients*: this class method calculates Knudsen diffusivities $\mathcal{D}_{i,K}$ according to kinetic gas theory.

13. *dustyGasFluxes*: this is the core method of the class, its purpose is the calculation of molar fluxes. All the other methods have the purpose to retrieve the data needed by the core method (transport properties, gradients etc.). The output is a $NS \times 3$ matrix where every row stores the *vector components* corresponding to the ith chemical species flux (see Equation (4.9)).

$$\mathbf{N_{i,3}} = \begin{pmatrix} N_{1,x} & N_{1,y} & N_{1,z} \\ N_{2,x} & N_{2,y} & N_{3,z} \\ \vdots & \vdots & \vdots \\ N_{NS,x} & N_{NS,y} & N_{NS,z} \end{pmatrix} \tag{4.9}$$

This matrix arises from the fact that three dimensional gradients are involved so molar fluxes must be three dimensional vectors accordingly.

The algorithm chosen to perform the solution is the LU decomposition: given a generic linear system

$$\mathbf{Ax} = \mathbf{b} \tag{4.10}$$

a LU factorization transforms the coefficient matrix into the product of a lower unit triangular matrix L and an upper triangular matrix U

$$\mathbf{A} = \mathbf{LU} \tag{4.11}$$

This technique actually splits the original problem into two decoupled subproblems

$$\begin{cases} \mathbf{Ly} = \mathbf{b} \\ \mathbf{Ux} = \mathbf{y} \end{cases} \tag{4.12}$$

which can be solved directly by forward and backward substitution as triangular matrixes are involved. The cost of solving a system of linear equations by LU factorization, if the matrix A has size *n*, is approximately $\frac{2}{3}n^3$ floating point operations which is 50% lower than Gauss elimination [23].

14. *resizeAll*: this class method allocates memory to store all the matrixes and vectors needed within the class, resizing them to fit the appropiate dimension depending on the number of chemical species involved.

The complete code of *dustyGas* class is listed in **Appendix A**.

4.2.3 The new set of transport equations

The transport equation for each species was coded specifically to work according to the Fick law, more precisely according to the following equation

$$\rho\frac{\partial\omega_i}{\partial t} = \nabla\cdot\left(\mathcal{D}_i\rho\nabla\left(\omega_i\right)\right) + \nabla\cdot\left(\omega_i\mathbf{J_c}\right) \tag{4.13}$$

with density constant and where

$$\mathbf{J_c} = -\sum_{i=1}^{n}\mathbf{J_i}$$

This way was totally inadequate for the dusty gas formulation so a new set of equation was created and an internal switch was inserted to allow catalyticFOAM to discriminate which model to use. The expression for this new diffusion set is

$$\begin{cases} \dfrac{\partial p_i}{\partial t} = -RT\nabla\cdot\mathbf{N_i} \\ p = \displaystyle\sum_{i=1}^{n} p_i \end{cases} \tag{4.14}$$

where molar fluxes $\mathbf{N_i}$ are given by Equation (2.39). A zero sum constraint on molar fluxes has no physical ground when pressure gradients are involved, so pressure is no more kept constant as its value is automatically reassigned as the sum of partial pressures. This approach can also be found in the literature [32].

4.2.4 Coupling with chemical reaction side

The new aforementioned diffusion equations had to be linked to the chemistry solver following the operator splitting approach. Variables calculated by the diffusion routine (pressure, temperature, mole fractions) had thus to be shared with the chemistry routine to solve mass balances in each cell on each time step. Subsequentely, the update values obtained from the chemistry routine needed to be given back to the diffusion routine to keep iterating.

4.2.5 PIMPLE loop extended

The use of a diffusion model which natively accounts for pressure gradients arises the issue of updating the coupling between solid and fluid regions to satisfy convergence for pressure at the interphase surface. This means that pressure must be *continous* when moving from a region to another (see Figure (4.2.2 [30]). This aspect, neglected in the

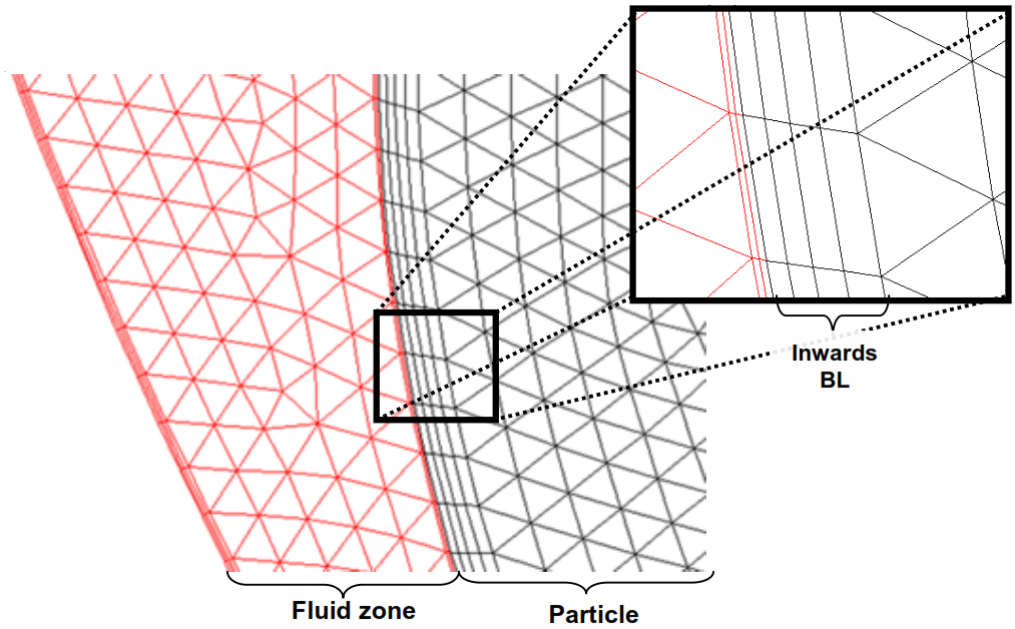

Figure 4.2.2: Sketch of the inner boundary layer between a fluid and a solid region. Pressure must have the same value while moving from the fluid to the solid phase and viceversa because it must be a *continous* function

current release of catalyticFOAM multiRegion code, is the major new feature deriving from the use of the dusty gas model.

4.3 Fully coupled (MATLAB®) versus operator-splitting (catalyticFOAM) implementation

To validate the right addition of *dustyGas* class into catalyticFOAM , a pure diffusion test case has been solved alongside with a MATLAB® simulation.

4.3.1 Solver differences

It must be stated that these two implementations present some differences:

1. MATLAB® fluxes are calculated for each spatial point simultaneously thus solving a block diagonal matrix, with size equal to NC $\times$ N (NC = number of components, N = grid points) with each block with size equal NC $\times$ N

2. catalyticFOAM takes into account fluxes obtained by the dusty gas class for each cell solving one of the $NC \times NC$ matrix that in MATLAB® represents only a block of the whole coefficient matrix

These statements mean that MATLAB® fully coupled approach would show more robustness, since it avoids spatial solution splitting, but would be incredibly heavy and thus not suitable for too complex simulations. Robustness is the ability to cope with errors during execution or to continue operating despite abnormabilities in inputs or calculations.

4.3.2 Test case: H_2O and O_2 diffusion through a slab

The situation analyzed consisted in studying the behaviour of a monodimensional slab full of $\mathrm{N_2}$, as inert, interacting with a mixture of $\mathrm{O_2}$ and $\mathrm{H_2O}$, both on unsteady (1 s) and steady state. To reach spatial convergence, the number of grid points is lower than in reacting cases since a pure diffusive case does not involve stiffness due to reaction. The boundary conditions used for this test are listed in Table (4.3.1).

The profile comparison shows that both the programs give the same results, thus confirming the success of the operation. In Figure (4.3.1), only small differences can be noticed since the diffusivity variations due to pressure in catalyticFOAM are negligible (pressure variation lower than 0.2%). In Figure (4.3.2), even on mole fraction profiles,

	Left side [Pa]	Right side [Pa]	Initial profile [Pa]
O_2	0	100000	0
H_2O	100000	0	0
N_2	0	0	100000
p	100000	100000	100000

Table 4.3.1: Conditions for the current case. The temperature is set to 773.15 K

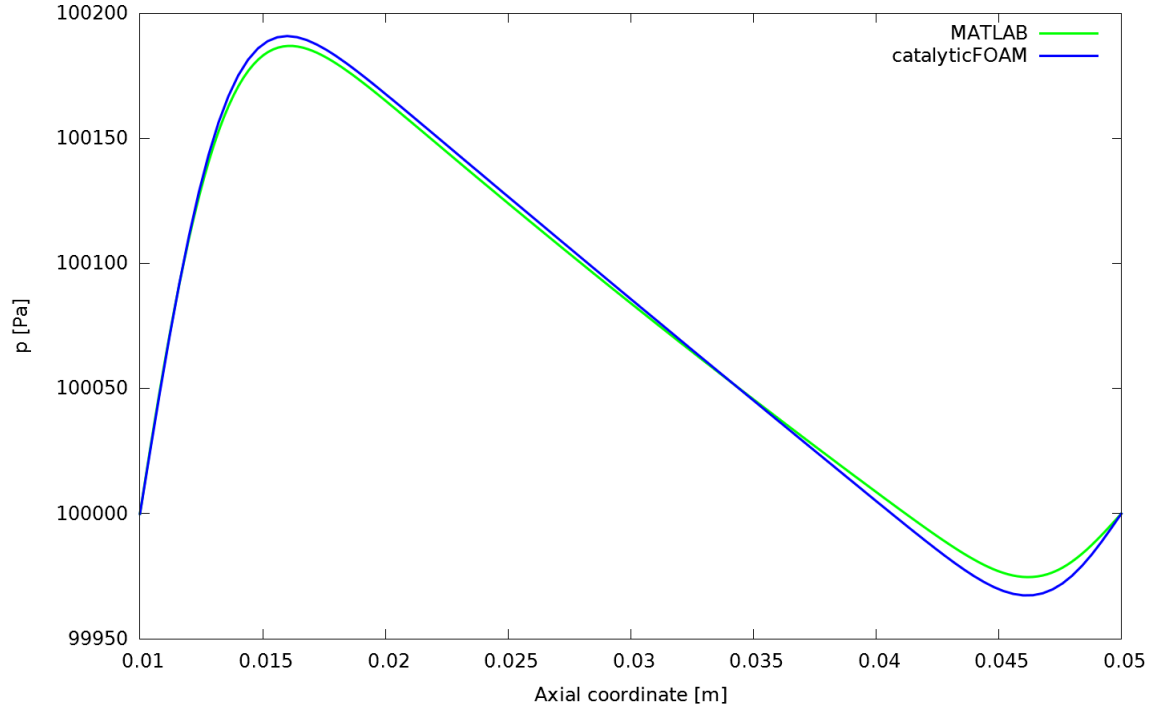

Figure 4.3.1: Transient comparison for pressure

no difference can be seen. The small quantity of H_2O that reaches the other edge of the slab shows a higher partial pressure due to the lower total pressure value of that region. In Figure (4.3.3), it can be noticed that the lower O_2 diffusivity prevents it from reaching the other side of the slab as efficiently as H_2O Figure (4.3.4) shows N_2 slowly leaving the slab during the unsteady part of the simulation. It can be seen that the pressure profile flattens again in Figure (4.3.5). The steady state profile is a straight line between the two boundaries, as mathematically expected. This is also true for H_2O and O_2 in Figure (4.3.6). In Figure (4.3.7), the inert species has left the catalytic media at steady state. Since no inert is left, H_2O and O_2 mixture fill the catalyst entirely.

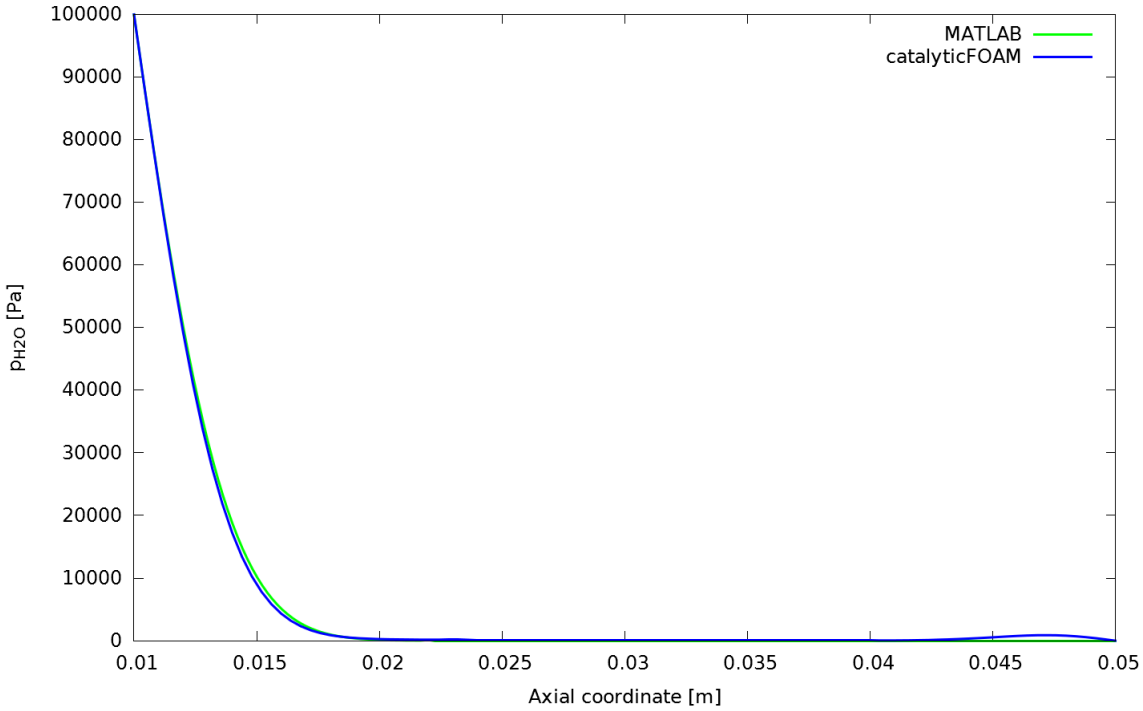

Figure 4.3.2: Transient comparison for H_2O partial pressure

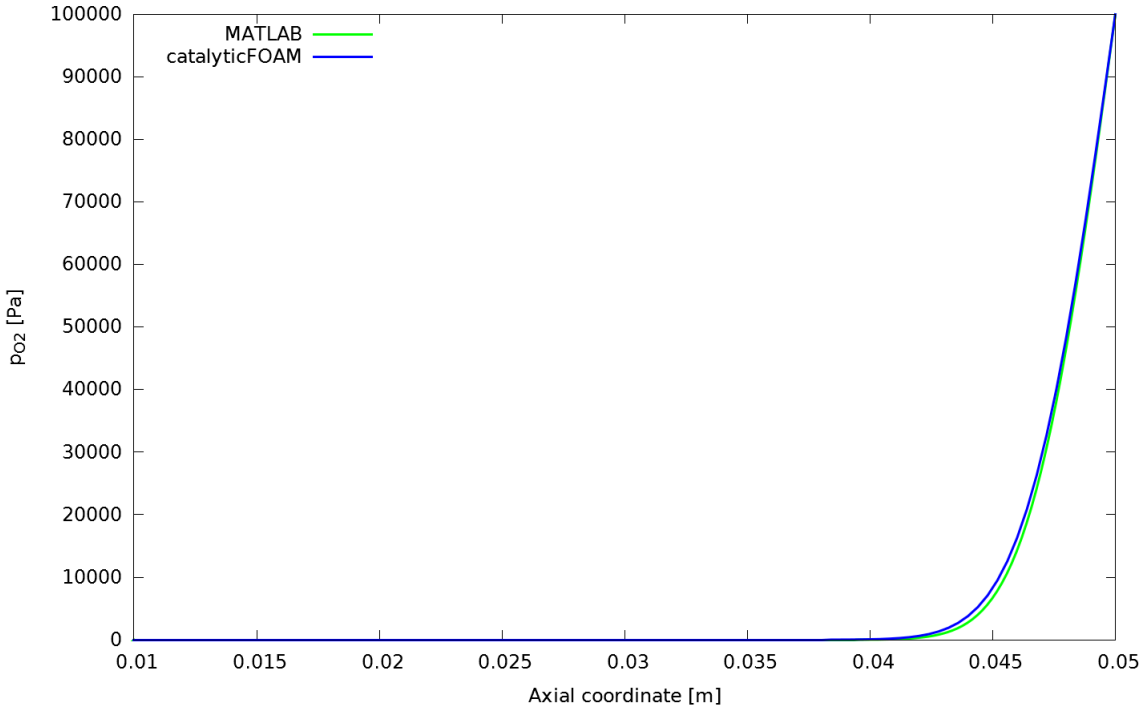

Figure 4.3.3: Transient comparison for O_2 partial pressure

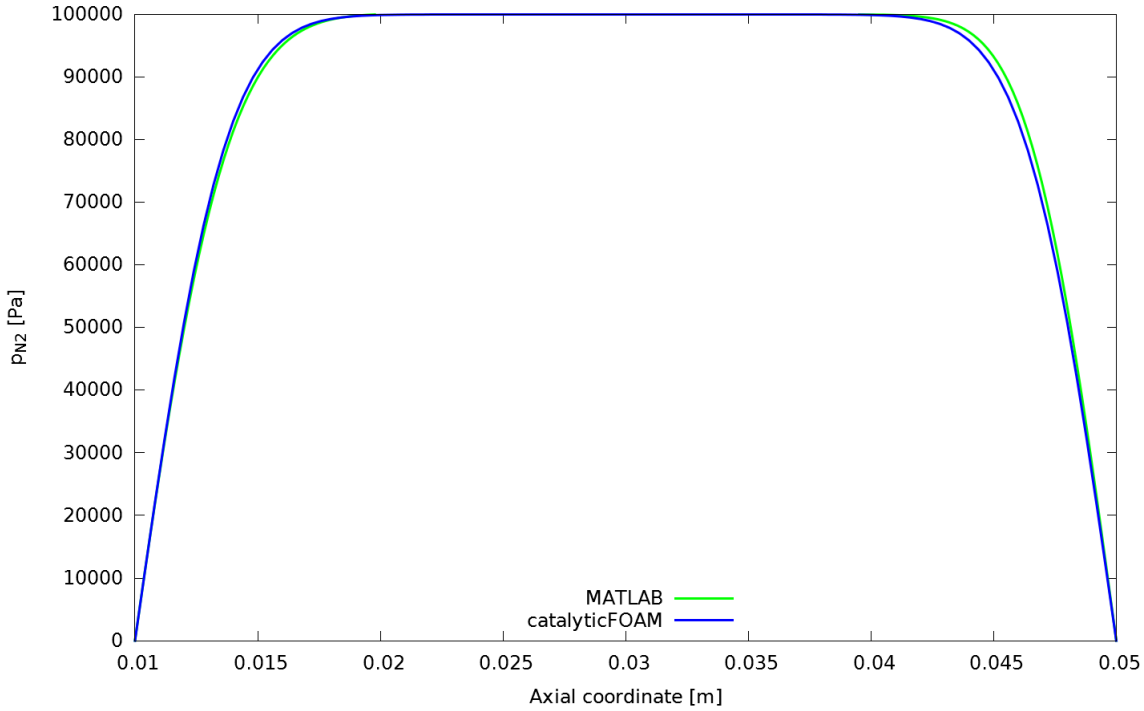

Figure 4.3.4: Unsteady state comparison for N_2 partial pressure

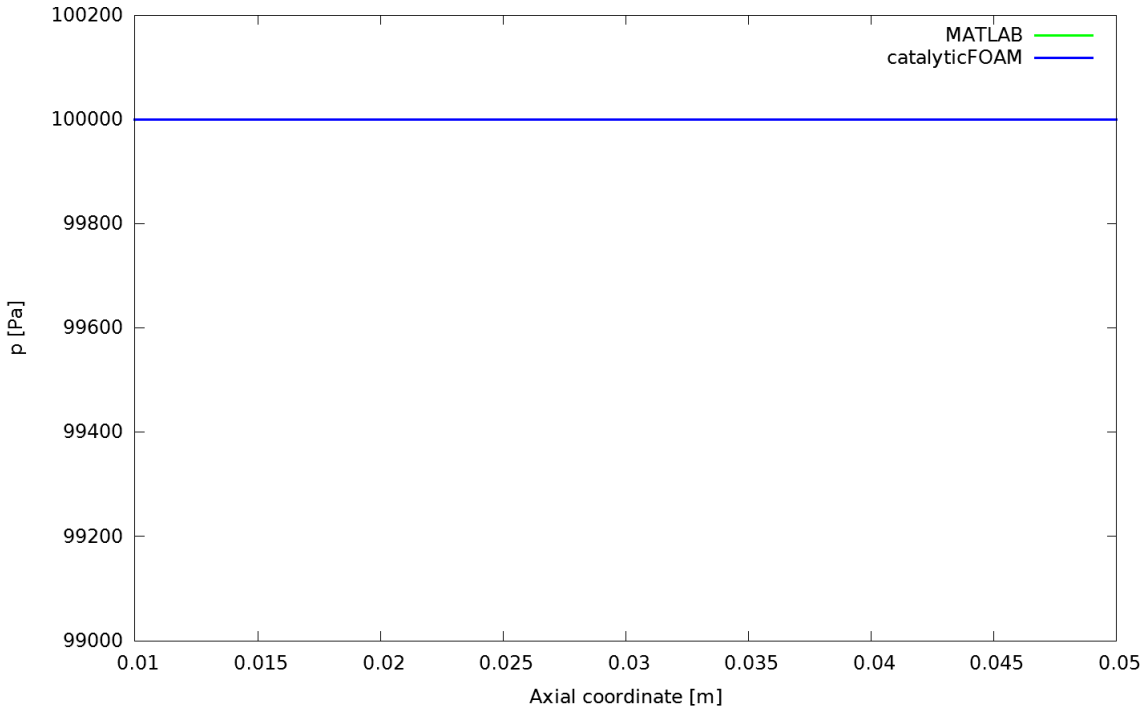

Figure 4.3.5: Steady state comparison for pressure

4.3.3 The effect of diffusivities on profiles

Afterwards, it was decided to compare the variation that replacing H_2O with H_2 would have had on catalyticFOAM results to check diffusivity value effects on pressure

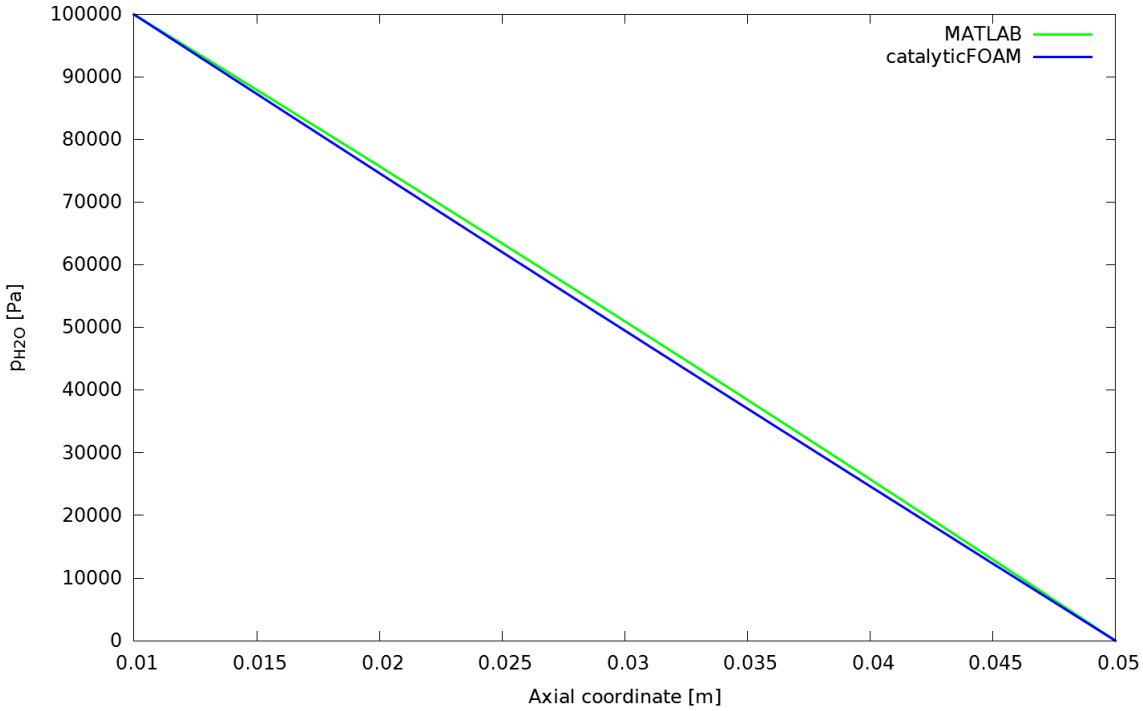

Figure 4.3.6: Steady state comparison for H_2O partial pressure

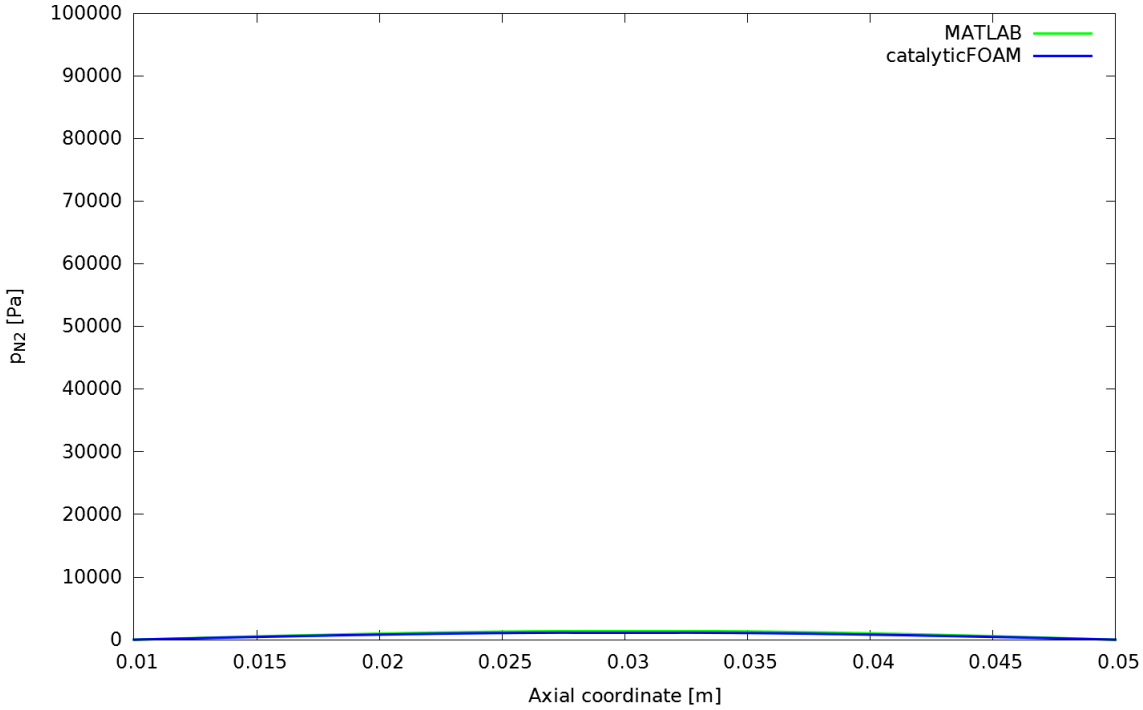

Figure 4.3.7: Steady state comparison for N_2 partial pressure

profiles. The boundary conditions used are listed in Table (4.3.2) and (4.3.3).

It can be noticed that this test case shows a pressure variation even without a reaction

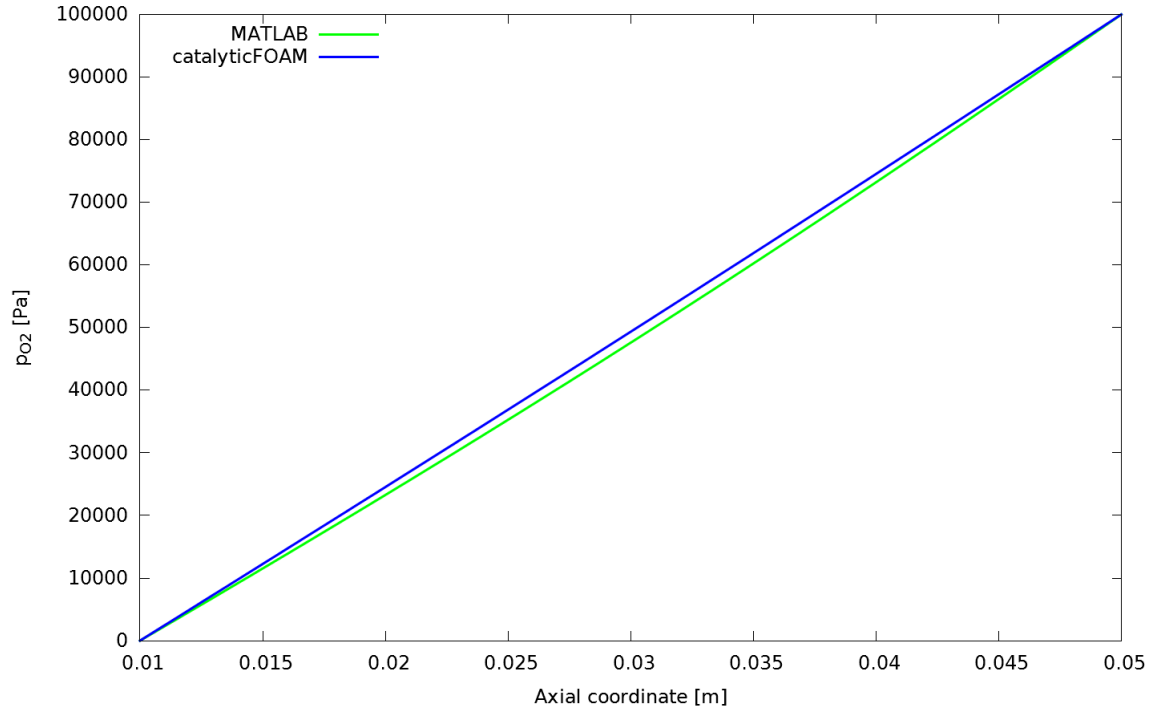

Figure 4.3.8: Steady state comparison for O_2 partial pressure

occuring. This behavior, unpredictable with the standard Fick model, will be further discussed. The effect of Knudsen diffusivities is not negligible. Being $\mathcal{D}^e_{H_2O} > \mathcal{D}^e_{N_2} > \mathcal{D}^e_{O_2}$ due to different molecular weights, the pressure growth can be explained by stating that the diffusion of H_2O inside the catalyst is faster than the diffusion of N_2 outside the catalyst. By the same argument the pressure drop nearby the O_2 boundary side is explained. An analogous case with H_2 in place of H_2O was used to further investigate the effect of diffusivity upon pressure. A higher pressure growth is noticed in unsteady conditions due to the higher Knudsen diffusivity of H_2 with respect to H_2O. As H_2 can

	Left side [Pa]	Right side [Pa]	Initial profile [Pa]
O_2	0	100000	0
H_2O	100000	0	0
H_2	0	0	0
N_2	0	0	0
p	100000	100000	100000

Table 4.3.2: Conditions for the current case. The temperature is set to 773.15 K

	Left side [Pa]	Right side [Pa]	Initial profile [Pa]
O_2	0	100000	0
H_2O	0	0	0
H_2	100000	0	0
N_2	0	0	0
p	100000	100000	100000

Table 4.3.3: Conditions for the current case. The temperature is set to 773.15 K

reach the opposite side of the slab much faster than H_2O, a lower mole fraction of O_2 with respect to the previous case is noticed. In Figure (4.3.9) a higher pressure growth

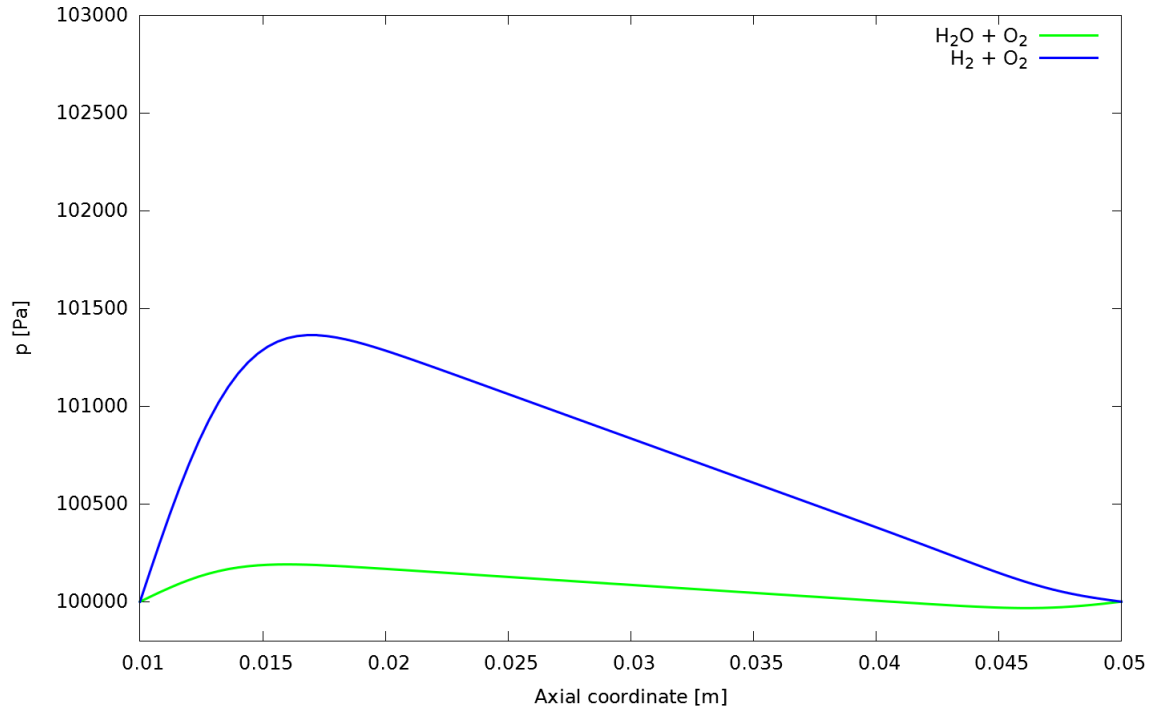

Figure 4.3.9: H_2O vs. H_2, unsteady pressure profiles

can be noticed in unsteady condition for the H_2 case with respect to the H_2O one due to higher Knudsen diffusivity of H_2O. In Figure (4.3.10), H_2 mole fraction is higher due to its greater Knudsen diffusivity. For the reason of an overall higher pressure, N_2 tends to leave the slab faster. The last statement implies a lower partial pressure for N_2 and so a higher partial pressure for O_2 on the right side of the slab (Figure (4.3.12)). Profiles simulated at steady state will now be analyzed. In Figure (4.3.13), pressure

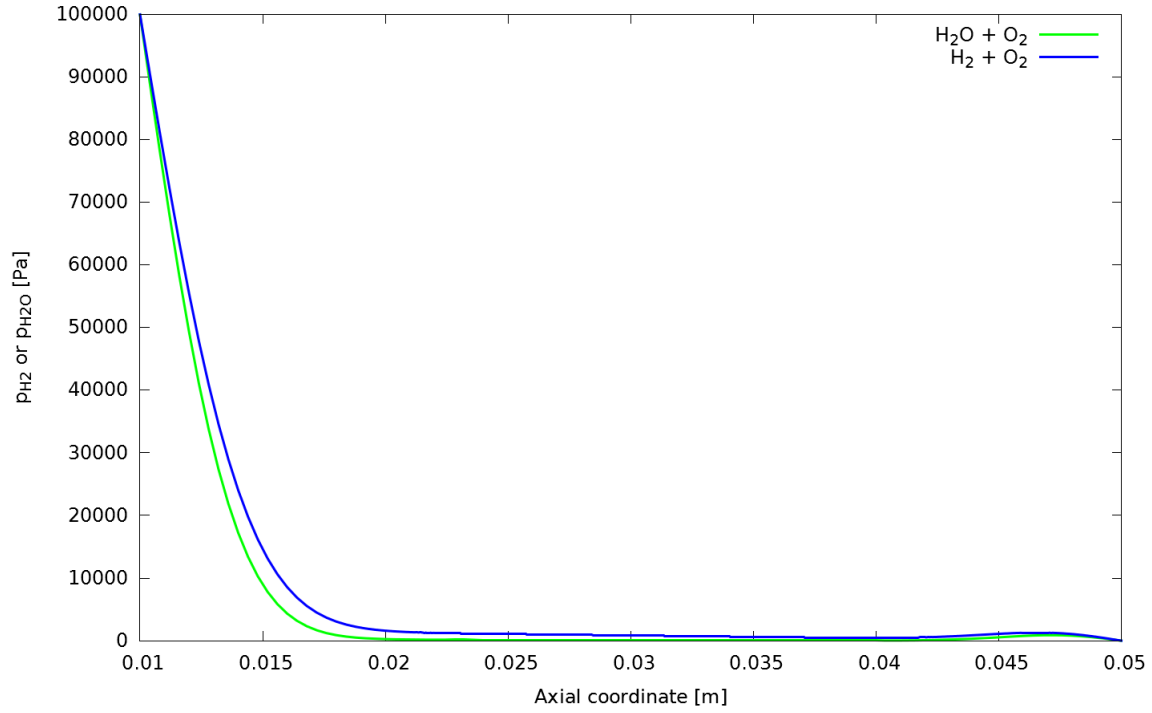

Figure 4.3.10: H_2O vs. H_2 unsteady profiles

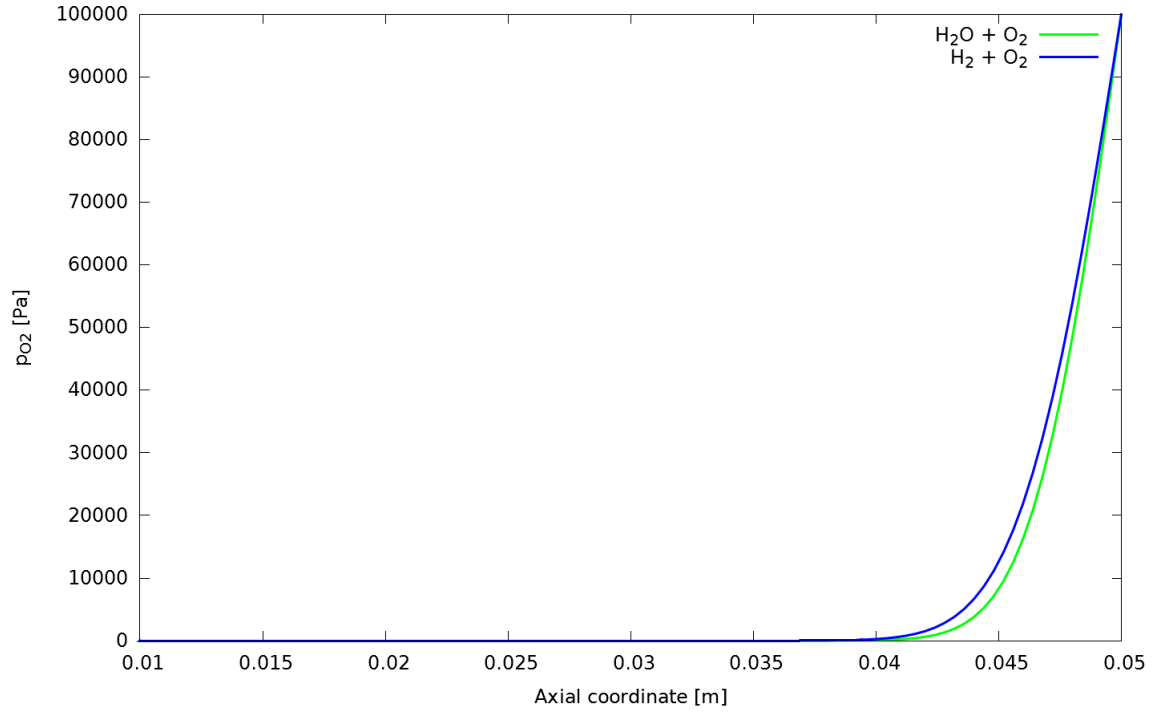

Figure 4.3.11: H_2O vs. H_2, unsteady O_2 profile

has reached the steady state in both cases and in Figure (4.3.14), it can be seen as H_2 and H_2O behavior becomes the same at steady state as so happens for every remaining

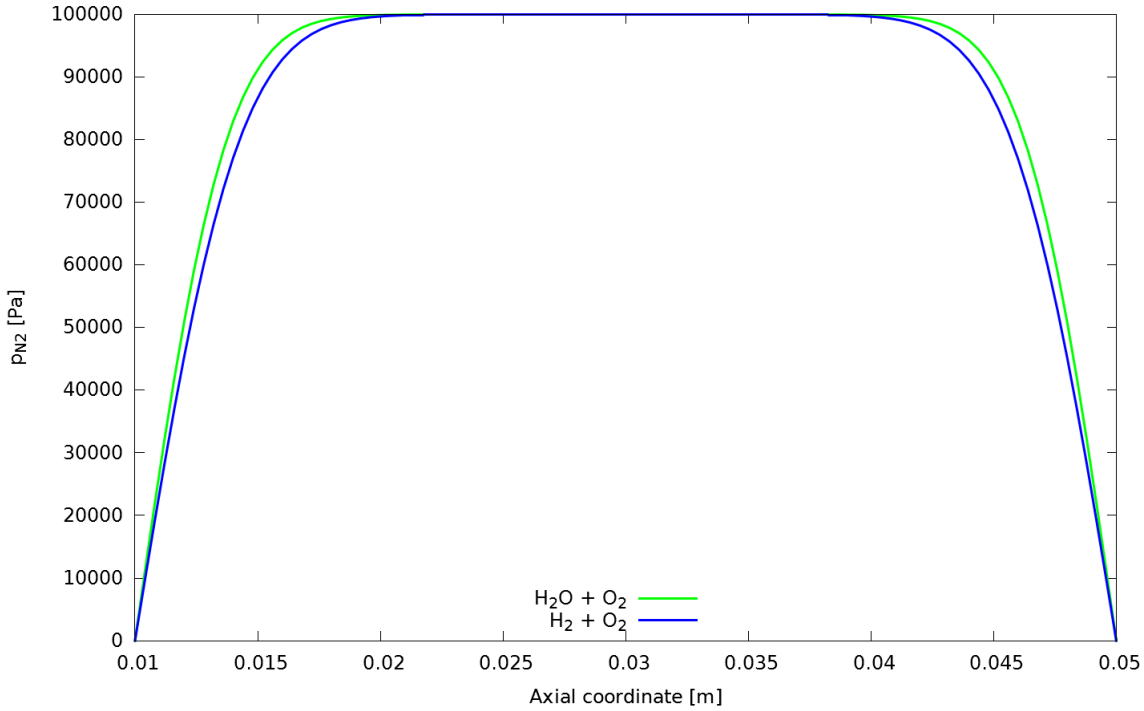

Figure 4.3.12: H_2O vs. H_2, unsteady N_2 profile

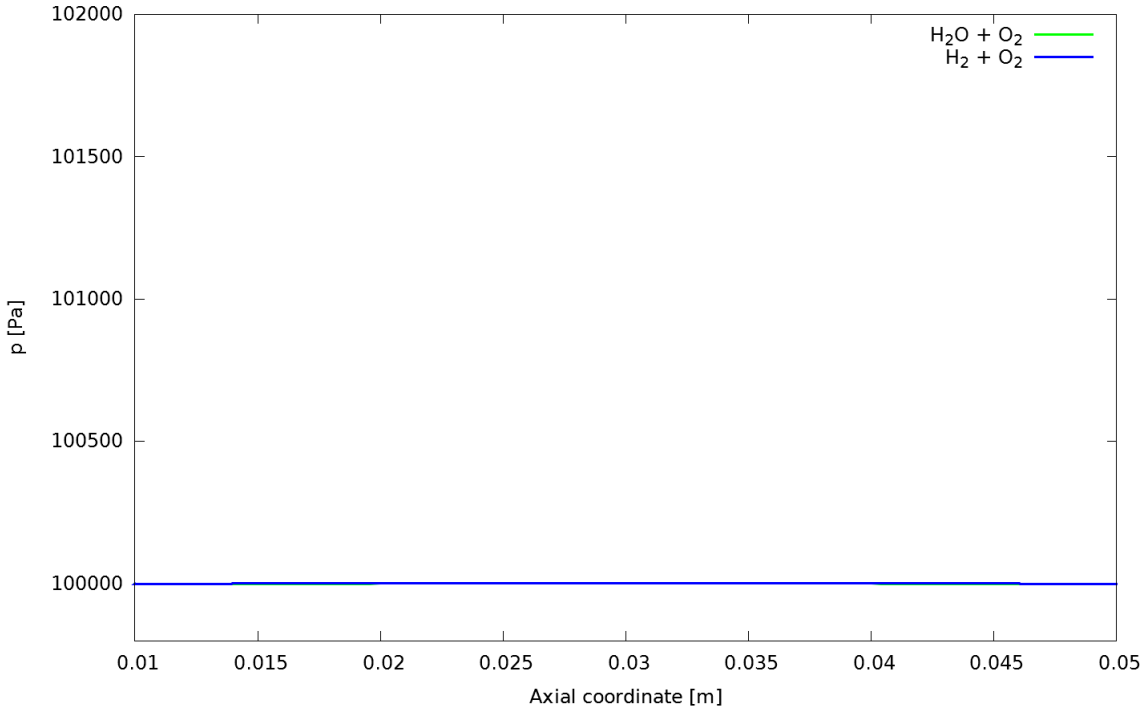

Figure 4.3.13: H_2O vs. H_2, steady state pressure profiles

species (whose profiles are omitted to avoid redundancy). The higher N_2 mole fraction, in the case with H_2O, was due to the lower pressure gradient which implies a smaller

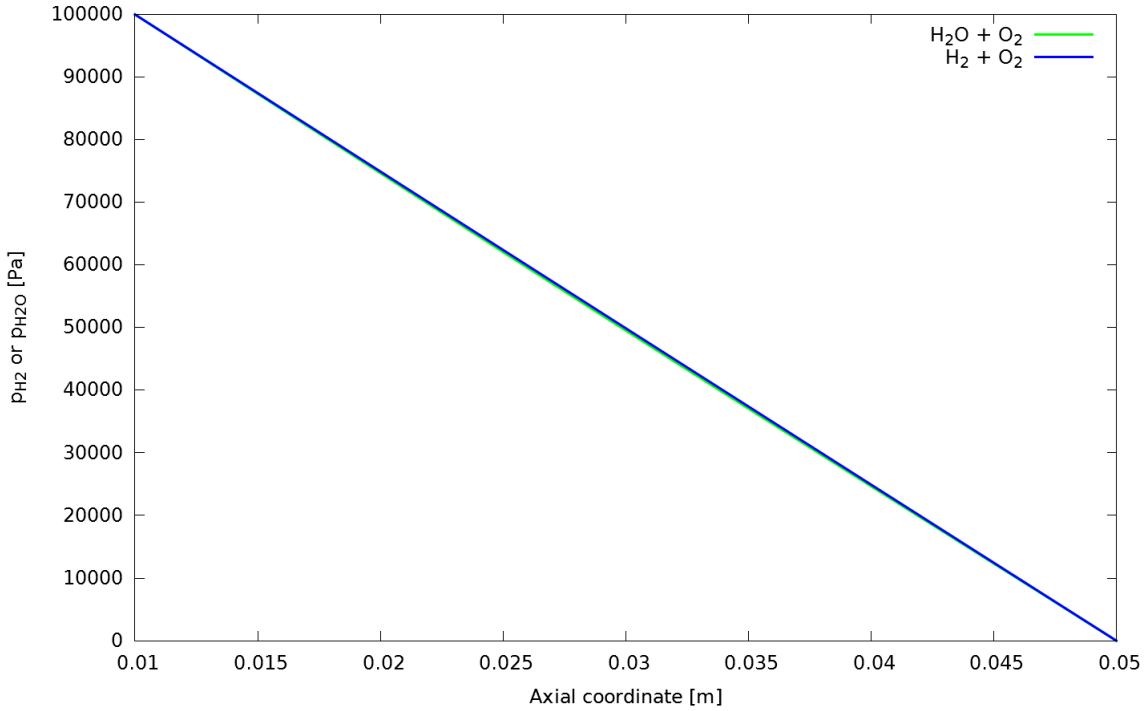

Figure 4.3.14: H_2O vs. H_2, steady state profiles

viscous flux. These differences vanish approaching the steady state condition when N_2 has left the slab.

4.4 catalyticFOAM: study of a H_2 heterogeneous oxidation case

After the study of pure diffusion conditions, reactive conditions in the same monodimensional slab were investigated: the reaction chosen for this purpose was the heterogeneous oxidation of H_2 on Rh

$$H_2 + 0.5\,O_2 \longrightarrow H_2O \tag{4.15}$$

coupled with a detailed, microkinetic scheme for the description of surface chemistry [8]. Two different inlet conditions, mixed reagents on both boundary sides or one pure reagent for each side, were considered. In the latter situation, reactants are far from each other so no considerable difference with respect to the pure diffusion condition can be noticed (see below). The comparison is carried out after $5s$ while, for mixed reagents

case, 1s proved to be enough to show the differences.

4.4.1 Pure reactants on opposite sides of the slab

The boundary and the initial conditions are listed in Table (4.4.1).

	Left side [Pa]	Right side [Pa]	Initial profile [Pa]
O_2	0	100000	0
H_2O	0	0	0
H_2	100000	0	0
N_2	0	0	0
p	100000	100000	100000

Table 4.4.1: Conditions for the current case. The temperature is set to 773.15 K

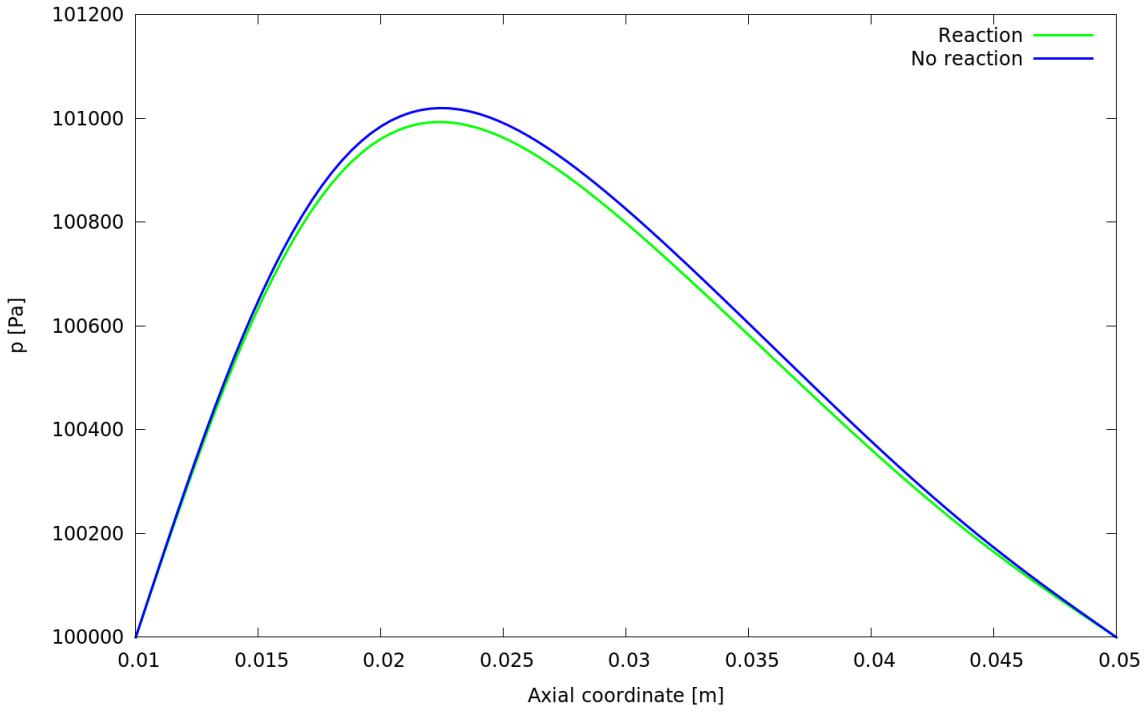

Figure 4.4.1: Opposite sides reagents, unsteady state pressure profile

In Figure (4.4.1), since the reaction stoichiometry implies a decreasing number of moles, the pressure on the reactive case drops consequently compared to its value on the diffusive simulation. It can be noticed in Figure (4.4.2) that only a small quantity of H_2O is produced due to the great distance between the reactants at the starting time. Furthermore, the production is concentrated near the O_2 edge since it is easier for H_2

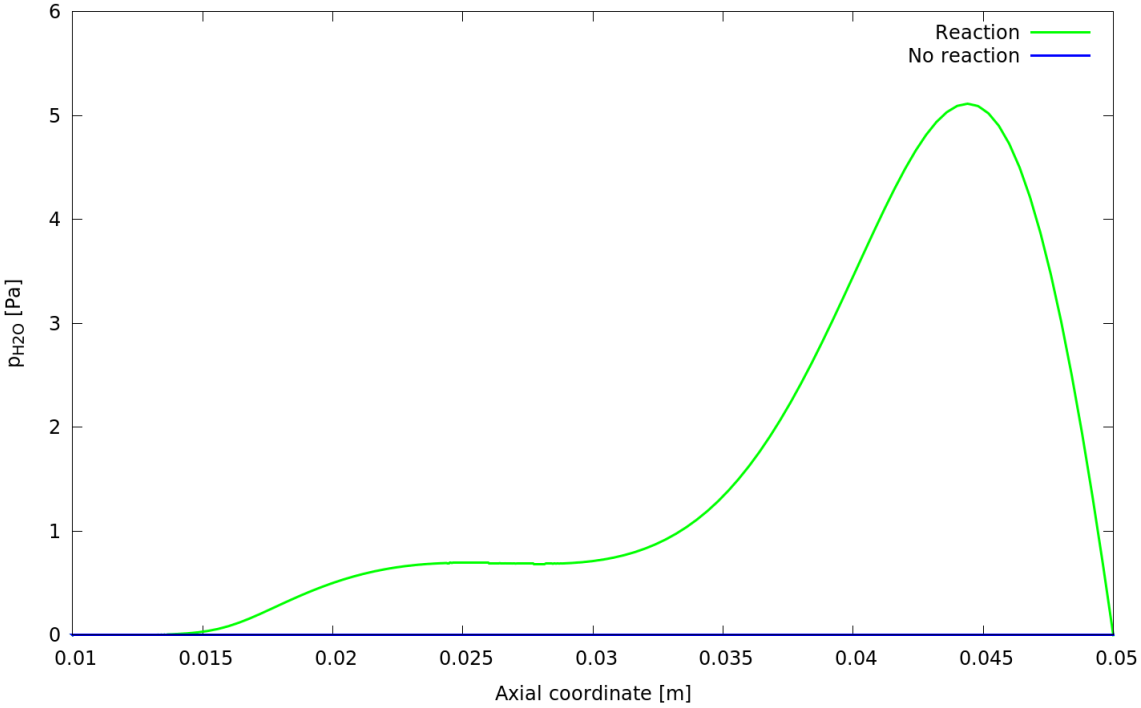

Figure 4.4.2: Opposite sides reagents, unsteady state H_2O profile

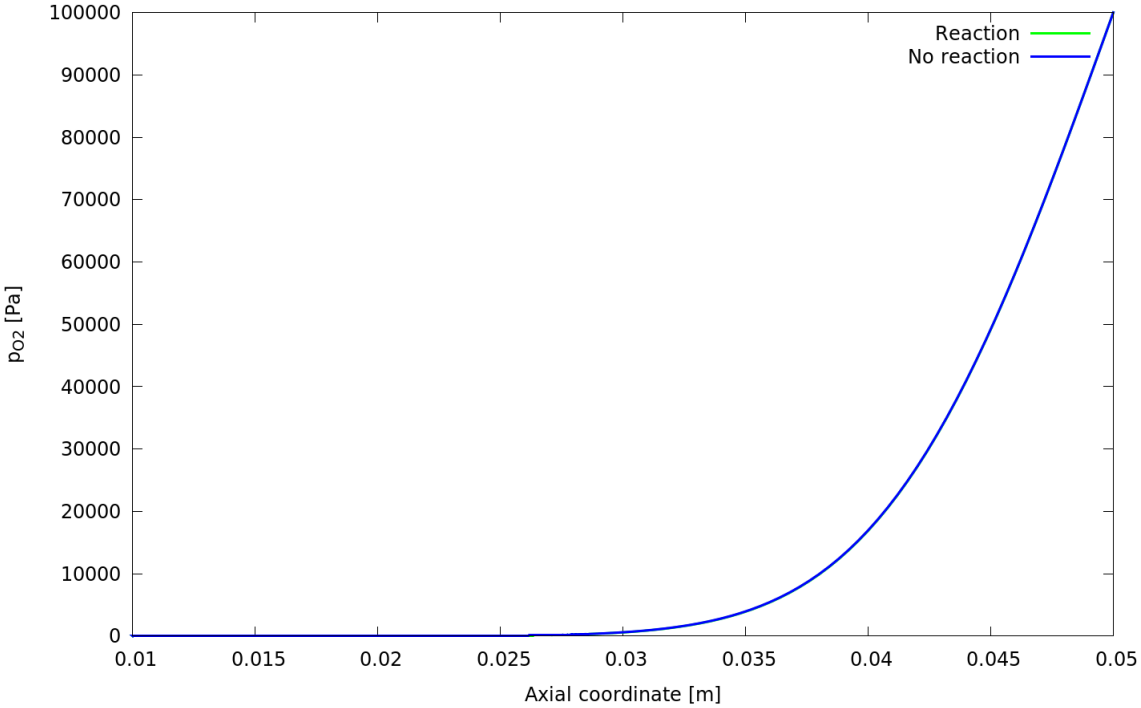

Figure 4.4.3: Opposite sides reagents, unsteady state O_2 profile

molecules to pass through the whole slab than for O_2 ones. In Figure (4.4.3), only few O_2 molecules manage to get through half of the slab while, In Figure (4.4.4), it is easy to

notice how H_2, differently with respect to the other reactant, crosses the slab more easily, thus showing higher partial pressure. The partial pressure profiles of the reactants show

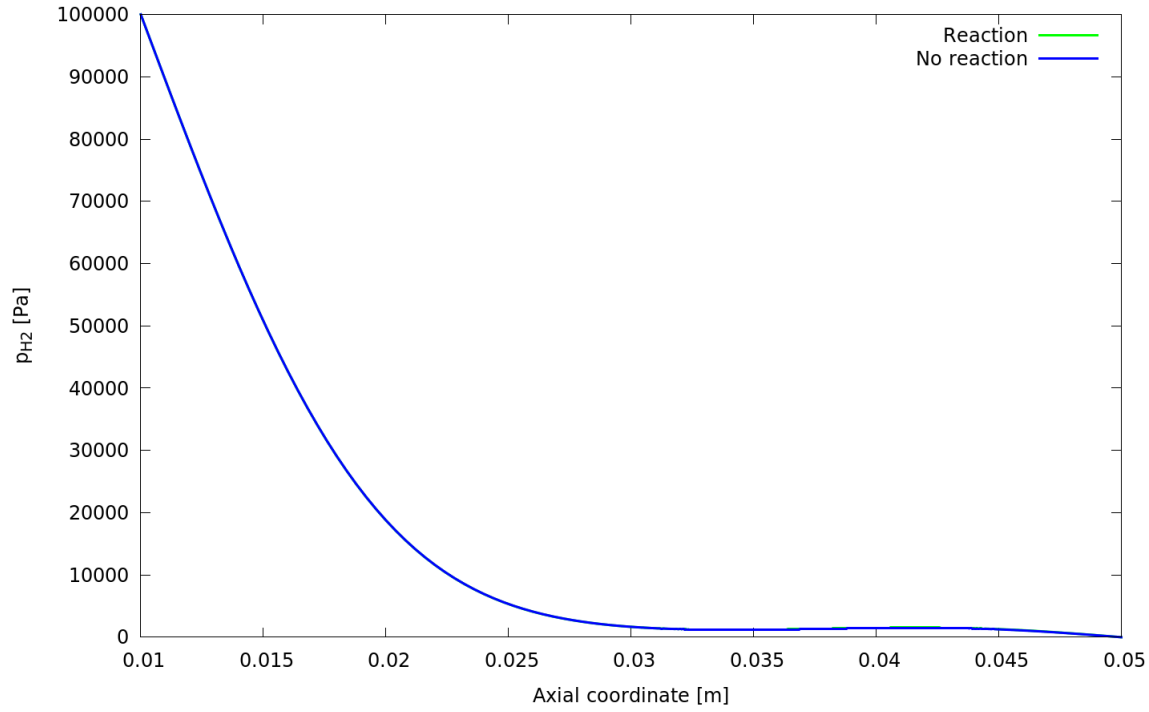

Figure 4.4.4: Opposite sides reagents, unsteady state H_2 profile

that the reaction rate is so low that no noticeable effect is present on their scale.

4.4.2 Mixed reactants on each side of the slab

The boundary and initial conditions are listed in Table (4.4.2).

	Left side [Pa]	Right side [Pa]	Initial profile [Pa]
O_2	25000	25000	0
H_2O	0	0	0
H_2	75000	75000	0
N_2	0	0	0
p	100000	100000	100000

Table 4.4.2: Conditions for the current case. The temperature is set to 773.15 K

The case of reactant mix inlet shows greater reaction effects with respect to the pure diffusive case than the case where the reactants are at the opposite sides of the slab.

Greater differences can be noticed on reactant profiles and on pressure drop. These differences are due to the fact that reactants are already mixed and they do not need to diffuse to reach each other.

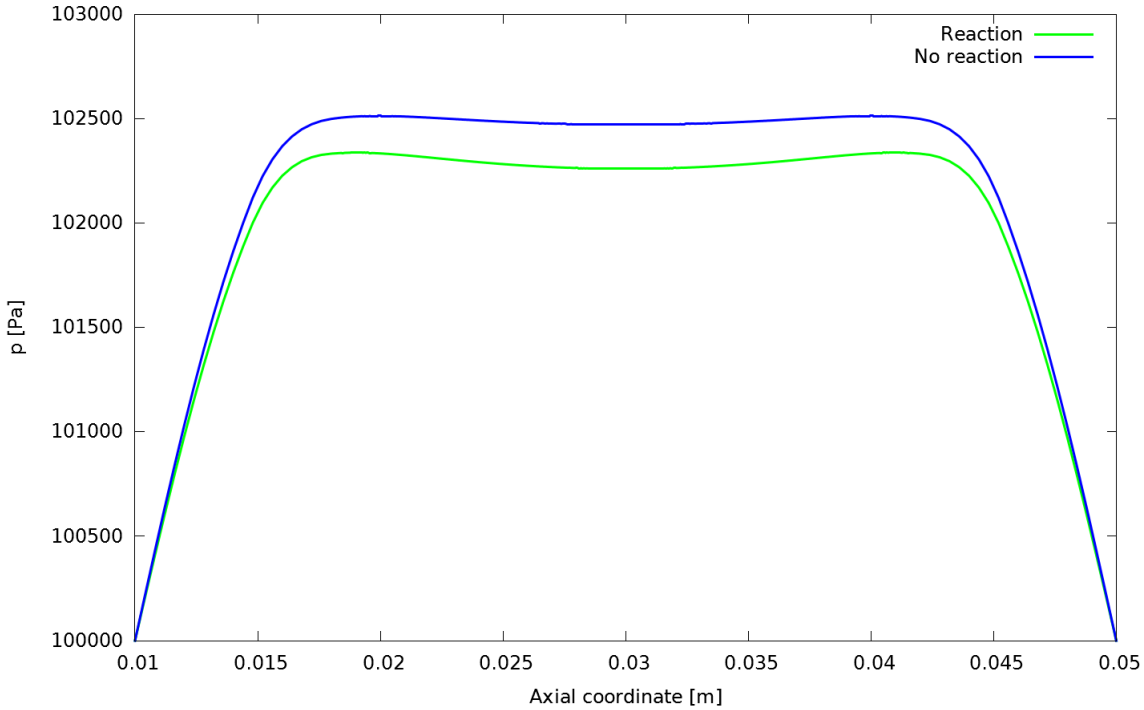

Figure 4.4.5: Mixed reagents, pressure profile

In Figure (4.4.5), the pressure drop due to the loss of moles after only 1 s is noticeable.

In Figure (4.4.6), it can be seen as a small percentage of H_2 is consumed by the reaction. However, in Figure (4.4.7), a higher O_2 partial pressure appears. This happens because, even if O_2 is converted, its contribution to the pressure drop is half of the H_2 contribution due to stoichiometry.

4.5 Conclusions

In this chapter the general structure and purpose of catalyticFOAM has been discussed. An object oriented class implementing the dusty gas formulation (*dustyGas*) has been described in detail, connected to the pre-existing catalyticFOAM layer, with the creation of a new equation set, and tested in reacting and not reacting cases. The agreement with MATLAB® results is very good, if same operating conditions are used, thus

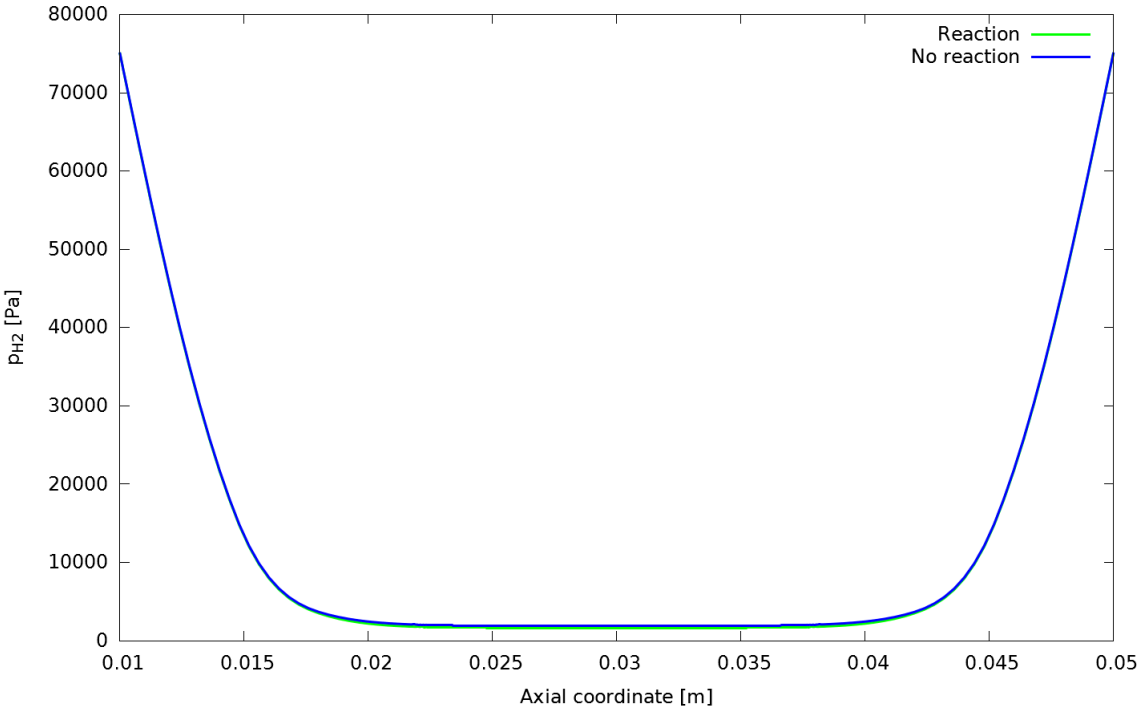

Figure 4.4.6: Mixed reagents, H_2 profile

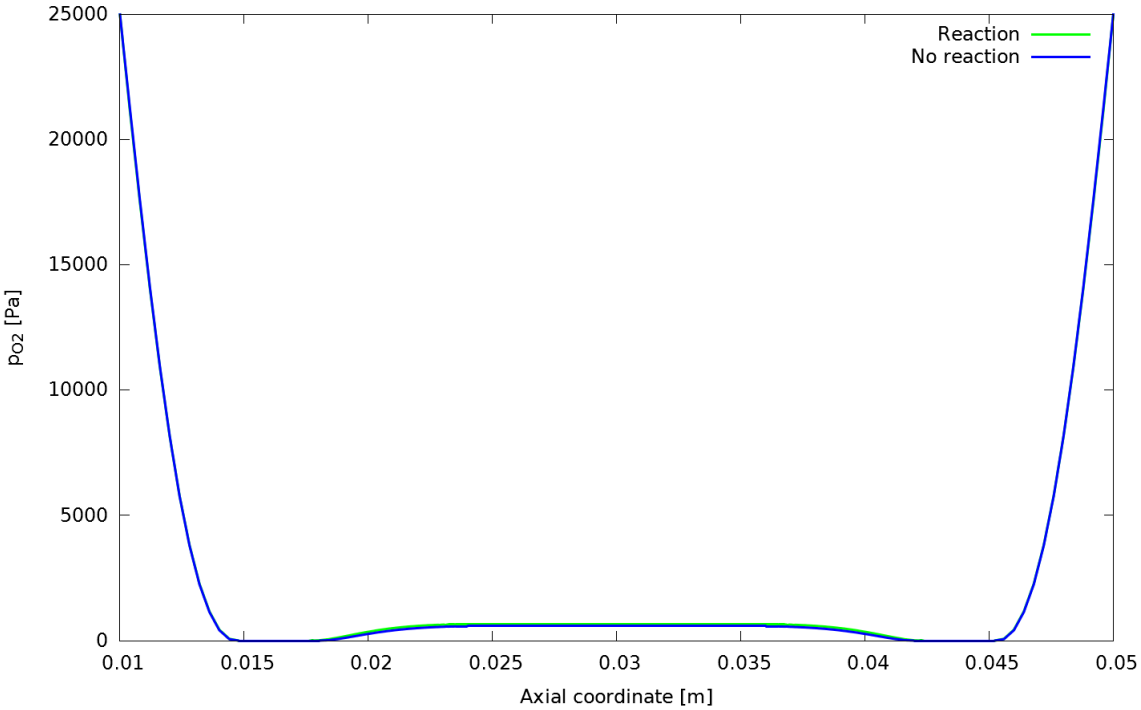

Figure 4.4.7: Mixed reagents, O_2 profile

suggesting a correct implementation within catalyticFOAM. The differences between the two simulators have also been pointed out. Simulations show that pressure is no more

constant as it follows stoichiometry of reactions within the solid phase and differences in diffusion abilities of the species. This is a major innovation with respect to the previous solver formulation. Consistency of the effects of heterogenous reactions and diffusion coefficient variation has been also checked. The PIMPLE loop had to be modified to account for pressure convergence at interphase surface to allow to solve multiregion cases. Thus, the resulting solver grants the possibility to analyze cases with different phases and complex geometries, accounting for pressure variations and viscous flows.

Chapter 5

Conclusions

The aim of the present work was the numerically implementation of the dusty gas diffusion approach for modelling diffusion with reaction in porous media coupled computational fluid dynamics. It has been discussed the set of equation needed to solve this kind of problem and the notable differences with Fickian approaches, both in implementation and in results. Parametrical analysis were made to check the consistency of the numerical algorithm and the result dependency over the values of the kinetic constant, the diffusivity values and the stoichiometry of the reaction, alongside with the comparison with Fickian model solution profiles. Convergence tests for the discretization were also conducted. It has been found that the pressure gradient estimation according to the standard Fick formulation was, in each case, higher or at least equal to the dusty gas estimation. The reason underlying this aspect is that Fickian fluxes are always lower than dusty gas fluxes since the Fickian approach does not take into account viscous flows. It has been also pointed out that, since higher pressure implies higher reaction rate, the catalyst efficiency estimation changes according to the model (standard Fick, extended Fick, dusty gas) used. Higher pressure estimation, as a consequence, leads to lower catalyst efficiency. With attention to the dusty gas model, the efficiency topic has been further analyzed taking into account variations of the stoichiometric coefficient ratio in binary reactions. The dependency of reaction rate on pressure, and thus on mole variations due to stoichiometry, have been analysed: the higher the increase in the number of moles was, the lower was the catalyst efficiency while, on the contrary, the higher the descrease in the number of moles was, the higher the catalyst efficiency was. Therefore,

parametrical analysis on diffusion coefficients showed how, regarding bicomponent cases, the standard Fick model, in contrast to the other models, accounts almost only for the lowest between Knudsen diffusivity and material diffusivity. This is proved by the overlap of profiles when the diffusion coefficient used has a value orders of magnitude higher than the Knudsen one. Hence, the goal to account for variations of pressure and fluxes caused by its gradient inside the catalyst was achieved. Afterwards, the dusty gas model was implemented, according to the operator-splitting algorithm, into catalyticFOAM. The correctness of the inclusion of the former implementation work into catalyticFOAM code has been tested, along with coupling of the chemistry reaction equation set with the diffusion one. The analysis was done simulating diffusion involving four different species (N_2, O_2, H_2 and H_2O) and H_2 combustion. A comparison of diffusive case results between MATLAB® fully coupled and operator-splitting catalyticFOAM approaches was used as test. After validation the purpose was to employ the dusty gas diffusion approach inside multiregion CFD simulations with complex catalyst geometries and microkinetic models.

Appendices

Appendix A

C++ code of *dustyGas* class

In this appendix the C++ code implementing the dusty gas model is presented. The code relies heavily on OpenSMOKE++ library for the calculation of thermochemical data.

```
#ifndef DUSTYGAS_H
#define DUSTYGAS_H

/*#include <iostream>

// OpenSMOKE++ Definitions
#include "OpenSMOKEpp"

// CHEMKIN Preprocessor
#include "preprocessing/PreProcessor_CHEMKIN"

// CHEMKIN maps
#include "maps/Maps_CHEMKIN"

// Reactor utilities
#include "reactors/utilities/Utilities"

// Eigen
#include <Eigen/Dense>

// Boost
#include <boost/program_options.hpp>
#include <boost/filesystem.hpp>

// RapidXML
#include "rapidxml.hpp"
*/

class dustyGas
{
    public:

        /**
        *Default constructor
        */
        dustyGas(OpenSMOKE::ThermodynamicsMap_CHEMKIN<double>& thermodynamicsMap,
                 OpenSMOKE::KineticsMap_CHEMKIN<double>& kineticsMap,
                 OpenSMOKE::TransportPropertiesMap_CHEMKIN<double>& transportMap,
                 OpenSMOKE::ThermodynamicsMap_Surface_CHEMKIN<double>& thermodynamicsSurfaceMap,
```

```
        OpenSMOKE::KineticsMap_Surface_CHEMKIN<double>& kineticsSurfaceMap);
/**
*Copy constructor
*/
dustyGas(const double temperature, const double pressure,
        OpenSMOKE::ThermodynamicsMap_CHEMKIN<double>& thermodynamicsMap,
        OpenSMOKE::KineticsMap_CHEMKIN<double>& kineticsMap,
        OpenSMOKE::TransportPropertiesMap_CHEMKIN<double>& transportMap,
        OpenSMOKE::ThermodynamicsMap_Surface_CHEMKIN<double>& thermodynamicsSurfaceMap,
        OpenSMOKE::KineticsMap_Surface_CHEMKIN<double>& kineticsSurfaceMap);

/**
*Default destructor
*/
virtual ~dustyGas();

/**
*@brief Resizes all matrixes and vectors
*/
void resizeAll();

/**
*@brief Reads and sets mass fractions plus calculates mole fractions
*/
void setMassFractions(const OpenSMOKE::OpenSMOKEVectorDouble &massFractions);

/**
*@brief Sets mole fractions and pressure gradients
*/
void setGradients(const OpenSMOKE::OpenSMOKEMatrixDouble &moleFractionGradient, const OpenSMOKE::OpenSMOKEVectorDouble &pressureGradient);

/**
*@brief Sets catalyst porosity, tortuosity and pore radius
*/
void setCatalystProperties(const double porosity,const double tortuosity,const double poreRadius);

/**
*@brief Sets catalyst permeability coefficient: choose which correlation to use by changing flag
*/
void setPermeability(const unsigned int flag);

/**
*@brief Sets Knudsen coefficient
*/
void setKnudsenCoefficient();

/**
*@brief Calculates binary diffusion coefficients
*/
void getBinaryGamma();

/**
*@brief Calculates Knudsen diffusion coefficients according to kinetic theory
*/
void calculateKnudsenDiffusionCoefficients();

/**
*@brief Sets temperature
*/
void setTemperature(const double temperature);

/**
*@brief Sets pressure
*/
```

```
        void setPressure(const double pressure);

        /**
        *@brief Sets dynamic viscosity
        */
        void setDynamicViscosity();

        /**
        *@brief Solves DG linear system
        */
        void dustyGasFluxes();

        /**
        *@brief Returns fluxes
        */
        const Eigen::MatrixXd& fluxes() const {return fluxes_;}

        /**
        *@brief Simply shows variables
        */
        void showValues();


    private:

        //OpenSMOKE objects
        OpenSMOKE::ThermodynamicsMap_CHEMKIN<double>& thermodynamicsMap_;                                   //!< thermodynamic map
        OpenSMOKE::KineticsMap_CHEMKIN<double>& kineticsMap_;                                               //!< kinetic map
        OpenSMOKE::TransportPropertiesMap_CHEMKIN<double>& transportMap_;                                       //!< transport map
        OpenSMOKE::ThermodynamicsMap_Surface_CHEMKIN<double>& thermodynamicsSurfaceMap_;    //!< thermodynamic map
        OpenSMOKE::KineticsMap_Surface_CHEMKIN<double>& kineticsSurfaceMap_;                        //!< kinetic map

        Eigen::MatrixXd A_; //matrix to store coefficients for DG linear system
        Eigen::MatrixXd b_; //matrix to store known terms for DG linear system
        Eigen::MatrixXd fluxes_;// DGM fluxes

        //General properties
        OpenSMOKE::OpenSMOKEVectorDouble massFractions_; //mass fractions
        OpenSMOKE::OpenSMOKEVectorDouble moleFractions_; //mole fractions
        unsigned int numberOfSpecies_; //number of components
        double temperature_; //temperature [K]
        double pressure_; //pressure [Pa]


        //Catalyst properties
        double porosity_; //catalyst porosity [-]
        double tortuosity_; //catalyst tortuosity [-]
        double correctionFactor_; //porosity/tortuosity [-]
        double poreRadius_; //catalyst pore radius [m]
        double K0_; //Knudsen coefficient [m]
        double B0_; //Permeability coefficient [m^2]

        //Transport properties
        double viscosityMix_; //mixture viscosity [Pa*s]
        OpenSMOKE::OpenSMOKEVectorDouble binaryDiffusionCoefficients_; //Binary diffusion coefficients [m^2/s]
        Eigen::VectorXd gammaBinary_; //Binary diffusion coefficients vector [m^2/s]
        Eigen::VectorXd knudsenDiffusionCoefficients_; //Knudsen coefficients [m^2/s]
        Eigen::MatrixXd D_; //Diffusion matrix


        //Gradients
        OpenSMOKE::OpenSMOKEMatrixDouble moleFractionGradient_; //Molar fraction gradient [1/m]
        OpenSMOKE::OpenSMOKEVectorDouble pressureGradient_; //Pressure gradients [Pa/m]
};
```

```
//Class implementation
dustyGas::dustyGas(OpenSMOKE::ThermodynamicsMap_CHEMKIN<double>& thermodynamicsMap,
                   OpenSMOKE::KineticsMap_CHEMKIN<double>& kineticsMap,
                   OpenSMOKE::TransportPropertiesMap_CHEMKIN<double>& transportMap,
                   OpenSMOKE::ThermodynamicsMap_Surface_CHEMKIN<double>& thermodynamicsSurfaceMap,
                   OpenSMOKE::KineticsMap_Surface_CHEMKIN<double>& kineticsSurfaceMap) :
        thermodynamicsMap_(thermodynamicsMap),
        kineticsMap_(kineticsMap),
        transportMap_(transportMap),
        thermodynamicsSurfaceMap_(thermodynamicsSurfaceMap),
        kineticsSurfaceMap_(kineticsSurfaceMap)
{

        numberOfSpecies_ = thermodynamicsMap_.NumberOfSpecies();
}

dustyGas::dustyGas(const double temperature, const double pressure,
                   OpenSMOKE::ThermodynamicsMap_CHEMKIN<double>& thermodynamicsMap,
                   OpenSMOKE::KineticsMap_CHEMKIN<double>& kineticsMap,
                   OpenSMOKE::TransportPropertiesMap_CHEMKIN<double>& transportMap,
                   OpenSMOKE::ThermodynamicsMap_Surface_CHEMKIN<double>& thermodynamicsSurfaceMap,
                   OpenSMOKE::KineticsMap_Surface_CHEMKIN<double>& kineticsSurfaceMap) :
        thermodynamicsMap_(thermodynamicsMap),
        kineticsMap_(kineticsMap),
        transportMap_(transportMap),
        thermodynamicsSurfaceMap_(thermodynamicsSurfaceMap),
        kineticsSurfaceMap_(kineticsSurfaceMap)
{

        numberOfSpecies_ = thermodynamicsMap_.NumberOfSpecies();
        temperature_=temperature;
        pressure_=pressure;
        transportMap_.SetTemperature(temperature_);
        transportMap_.SetPressure(pressure_);
}


void dustyGas::resizeAll()
{

    D_.resize(numberOfSpecies_,numberOfSpecies_);
    A_.resize(numberOfSpecies_,numberOfSpecies_);
    b_.resize(numberOfSpecies_,3);
    knudsenDiffusionCoefficients_.resize(numberOfSpecies_);
    fluxes_.resize(numberOfSpecies_,3);
    ChangeDimensions(numberOfSpecies_,&massFractions_,true);
    ChangeDimensions(numberOfSpecies_,&moleFractions_,true);
    ChangeDimensions(numberOfSpecies_,3,&moleFractionGradient_,true);
    ChangeDimensions(3,&pressureGradient_,true);
}

void dustyGas::setMassFractions(const OpenSMOKE::OpenSMOKEVectorDouble &massFractions_)
{
    // Assign mass fractions
    double MW;
    thermodynamicsMap_.MoleFractions_From_MassFractions(moleFractions_,MW,massFractions_);

}

void dustyGas::setGradients(const OpenSMOKE::OpenSMOKEMatrixDouble &moleFractionGradient,const OpenSMOKE::OpenSMOKEVectorDouble &pressureGradient)
{

    moleFractionGradient_= moleFractionGradient;
```

```
    pressureGradient_= pressureGradient;

}

void dustyGas::getBinaryGamma()
{

    //Assign binary diffusion coefficients
    transportMap_.getGammaBinary(binaryDiffusionCoefficients_); //see TransportPropertiesMap.h and TransportPropertiesMap.hpp
    gammaBinary_.resize(binaryDiffusionCoefficients_.Size());

    for(unsigned int i=0;i<binaryDiffusionCoefficients_.Size();i++)
    {

        gammaBinary_(i)=(pressure_/100000.)/binaryDiffusionCoefficients_[i+1]; //Pressure must be in [Pa]!
    }

    unsigned int counter=0;

    for(unsigned int i=0;i<numberOfSpecies_;i++)
    {
        D_(i,i)=0;

        for(unsigned int j=1+i;j<numberOfSpecies_;j++)
        {

            D_(i,j)=gammaBinary_(counter);
            D_(j,i)=D_(i,j);
            counter++;
        }
    }
}

void dustyGas::setCatalystProperties(const double porosity,const double tortuosity,const double poreRadius)
{

    porosity_ = porosity;
    tortuosity_ = tortuosity;
    correctionFactor_= porosity_/tortuosity_;
    poreRadius_ = poreRadius;

}

void dustyGas::setKnudsenCoefficient()
{

    K0_ = (porosity_*poreRadius_)/(2.*tortuosity_);
    //(ref. J.W. Veldsink,
    "A␣catalytically␣active,␣non-permselective,␣membrane␣reactor␣for␣kinetically␣fast,␣strongly␣exothermic,␣heterogeneous␣reactions")
}

void dustyGas::setTemperature(const double temperature)
{

    temperature_= temperature;
    transportMap_.SetTemperature(temperature_);
}

void dustyGas::setPressure(const double pressure)
{

    pressure_= pressure;
    transportMap_.SetPressure(pressure_);
}
```

```
void dustyGas::setDynamicViscosity()
{

    transportMap_.DynamicViscosity(viscosityMix_,moleFractions_);
}

void dustyGas::calculateKnudsenDiffusionCoefficients()
{

    for(unsigned int i=0;i<numberOfSpecies_;i++)
    {

knudsenDiffusionCoefficients_(i)=
(4./3.)*K0_*std::sqrt((8.*PhysicalConstants::R_J_mol*temperature_)/(PhysicalConstants::pi*thermodynamicsMap_.MW()[i+1]));
    }


}

void dustyGas::setPermeability(const unsigned int flag)
{

    if (flag == 1)
    {

        B0_ = std::pow(porosity_*(poreRadius_),2.)/(8.*tortuosity_); //Veldsink correlation for B0
        //(ref. J.W. Veldsink,
        "A catalytically active, non-permselective, membrane reactor for kinetically fast, strongly exothermic, heterogeneous reactions")
    }

    else if (flag == 2)
    {

        B0_ = std::pow(poreRadius_,2.)/(32.); //Poiseuille correlation for cylindrical pore
        //(ref. R. Krishna, J.A. Wesseling, "The Maxwell-Stefan approach to mass transfer")
    }

    else if (flag == 3)
    {

        B0_ = std::pow((poreRadius_),2.)/(180.)*std::pow(porosity_/(1.-porosity_),2.); //Carman-Kozeny correlation for aggregated bed of spheres
        //(ref. R. Krishna, J.A. Wesseling, "The Maxwell-Stefan approach to mass transfer")
    }

    else

    {

        std::cout<<"Setting permeability coefficient..."<<std::endl;
        std::cout<<"NO CORRELATION FOUND!"<<std::endl;
        std::cout<<"Setting permeability coefficient to 0!"<<std::endl;
        B0_ = 0.;
    }
}


void dustyGas::dustyGasFluxes()
{

    for(unsigned int i=0;i<numberOfSpecies_;i++)
    {

        for(unsigned int j=0;j<3;j++)
```

```
        {

b_(i,j) =
-((1./(PhysicalConstants::R_J_mol*temperature_))*(moleFractionGradient_[i+1][j+1]+(moleFractions_[i+1]/pressure_)...
...*(1.+(B0_*pressure_)/(viscosityMix_*knudsenDiffusionCoefficients_(i)))*pressureGradient_[j+1]));
        }
    }

    Eigen::VectorXd sum(numberOfSpecies_);

    for(unsigned int i=0;i<numberOfSpecies_;i++)
    {

        sum(i)=0;
    }

    for(unsigned int i=0;i<numberOfSpecies_;i++)
    {

        for(unsigned int j=0;j<numberOfSpecies_;j++)
        {

            if(i!=j)
            {

                sum(i) += moleFractions_[j+1]/(pressure_*D_(i,j)*correctionFactor_);
            }
        }
    }

    for(unsigned int i=0;i<numberOfSpecies_;i++)
    {

        for(unsigned int j=0;j<numberOfSpecies_;j++)
        {
            if(i!=j)
            {

                A_(i,j) = -(moleFractions_[i+1])/(pressure_*D_(i,j)*correctionFactor_);
            }

            else
            {

                A_(i,j) = (1./(pressure_*knudsenDiffusionCoefficients_(i)))+sum(i);
            }

        }

    }

    Eigen::PartialPivLU<Eigen::MatrixXd> luDec(A_);
    fluxes_ = luDec.solve(b_); //see Eigen documentation: http://eigen.tuxfamily.org/index.php?title=API_Showcase
}

void dustyGas::showValues()
{
    std::cout<<"-----------------------------------------------------------------------------------------" <<std::endl;
    std::cout<<"Species: "<<numberOfSpecies_<<" [-]"<<std::endl;
    std::cout<<"-----------------------------------------------------------------------------------------" <<std::endl;
    std::cout<<"Temperature: "<<temperature_<<" [K]"<<std::endl;
    std::cout<<"-----------------------------------------------------------------------------------------" <<std::endl;
    std::cout<<"Pressure: "<<pressure_<<" [Pa]"<<std::endl;
    std::cout<<"-----------------------------------------------------------------------------------------" <<std::endl;
```

```
    std::cout<<"Viscosity: "<<viscosityMix_<<" [Pa*s]"<<std::endl;
    std::cout<<"-------------------------------------------------------------------------------------------" <<std::endl;
    std::cout<<"Porosity: "<<porosity_<<" [-]"<<std::endl;
    std::cout<<"-------------------------------------------------------------------------------------------" <<std::endl;
    std::cout<<"Tortuosity: "<<tortuosity_<<" [-]"<<std::endl;
    std::cout<<"-------------------------------------------------------------------------------------------" <<std::endl;
    std::cout<<"Pore radius: "<<poreRadius_<<" [m]"<<std::endl;
    std::cout<<"-------------------------------------------------------------------------------------------" <<std::endl;
    std::cout<<"Knudsen coefficient: "<<K0_<<" [m]"<<std::endl;
    std::cout<<"-------------------------------------------------------------------------------------------" <<std::endl;
    std::cout<<"Knudsen diffusion coefficients [m^2/s]: "<<std::endl;
    std::cout<<knudsenDiffusionCoefficients_<<std::endl;
    std::cout<<"-------------------------------------------------------------------------------------------" <<std::endl;
    std::cout<<"Permeability coefficient: "<<B0_<<" [m^2]"<<std::endl;
    std::cout<<"-------------------------------------------------------------------------------------------" <<std::endl;
    std::cout<<"Coefficient matrix: "<<std::endl;
    std::cout<<A_<<std::endl;
    std::cout<<"-------------------------------------------------------------------------------------------" <<std::endl;
    std::cout<<"Right side: "<<b_<<std::endl;
    std::cout<<"-------------------------------------------------------------------------------------------" <<std::endl;
    std::cout<<"Fluxes: "<<fluxes_<<std::endl;
    std::cout<<"-------------------------------------------------------------------------------------------" <<std::endl;
}

dustyGas::~dustyGas()
{

}


#endif // DUSTYGAS_H
```

Bibliography

[1] Bischoff, K. B., Froment, G. F. *Chemical Reactor Analysis and Design*. 1979.

[2] Blunt, M. J. et al. Pore-scale imaging and modelling. *Advances in Water Resources* 51 (2013), pp. 197–216.

[3] Boudin, L., Grec, B., Salvarani, F. A mathematical and numerical analysis of the Maxwell-Stefan diffusion equations. *Discrete and continuous dynamical systems Series B* 17.5 (2012), pp. 1427–1440.

[4] Calderbank, P. H., Moo-Young, M. B. *Chemical Engineering Science* 16.39 (1961).

[5] Calonaci, M., Furnari, F. *A computational framework for the simulation of gas-solid catalytic reactors based on a multiregion approach*. Politecnico di Milano, 2011.

[6] Cuoci, A., Maestri, M. Coupling CFD with detailed microkinetic modeling in heterogeneous catalysis. *Chemical Engineering Science* 96 (2013), pp. 106–117.

[7] Cybulski, A., Moulijn, A. J. *Structured Catalysts and Reactors*. Taylor & Francis Group, 2006.

[8] Deutschmann, O. et al. *Proceedings of the Combustion Institute* 26 (1996), pp. 1747–1754.

[9] Dreyer, J. A. H. et al. Modelling of gas diffusion in highly porous nanostructures by direct simulation Monte Carlo. *Chemical Engineering Science* 105 (2014), pp. 69–76.

[10] Ferrero, A., Gazzola, F., Zanotti, M. *Elementi di analisi superiore per la fisica e l'ingegneria*. Esculapio, 2013, p. 103.

[11] Ferziger, J. H., Peric, M. *Computational Methods for Fluid Dynamics*. Springer, 2002.

[12] Gentile, G., Manelli, F. *An efficient computational framework for the advanced modeling and design of industrial catalytic reactors*. Politecnico di Milano, 2013.

[13] Goisis, S., Osio, A. *Computational fluid dynamics of gas-solid catalytic reactors based on microkinetic description of surface chemistry*. Politecnico di Milano, 2011.

[14] *http://www.detchem.com/*.

[15] Keil, F. J. Modelling of phenomena wiwith catalyst particles. *Chemical Engineering Science* 51.10 (1996), pp. 1543–1567.

[16] Krishna, R. Multicomponent gaseous diffusion in porous media in the transition region. A matrix method for calculation of steady-state transport rates. *Industrial Engineering Chemistry Fundamentals* 16.2 (1977), pp. 228–232.

[17] Krishna, R., Van Den Broeke, L. J. P. Experimental verificiation of the Maxwell-Stefan theory for micropore diffusion. *Chemical Engineering Science* 50.16 (1995), pp. 2507–2522.

[18] Krishna, R., Wesselingh, J. A. The Maxwell-Stefan approach to mass transfer. *Chemical Engineering Science* 52.6 (1997), pp. 861–911.

[19] Maestri, M., Reuter, K. Semiempirical rate constants for complex chemical kinetics: First-principles assessment and rational refinement. *Angewandte Chemie - International Edition* 50.5 (2011), pp. 1194–1197.

[20] Maffei, T., Rebughini, S., et al. CFD analysis of the channel shape effect in monolith catalysts for the CH_4 partial oxidation on Rh. *Chemical Engineering and Technology* 86 (2014), pp. 1099–1106.

[21] Maffei, T., Gentile, G., et al. A multiregion operator-splitting CFD approach for coupling microkinetic modeling with internal porous transport in heterogeneous catalytic reactors. *Chemical Engineering Journal* 283 (2016), pp. 1392–1404.

[22] Malinauskas, A. P., Mason, E. A. *Gas transport in porous media: The dusty gas model*. Elsevier, 1983.

[23] Manca, D. *Calcolo numerico applicato*. Pitagora, 2007, p. 68.

[24] Novak, V. et al. Understanding the gas transport in porous catalyst layers by using digital reconstruction techniques. *Current Opinion in Chemical Engineering* 9 (2015), pp. 16–26.

[25] Rieckmann, C., Keil, F. J. Multicomponent Diffusion and Reaction in Three-Dimensional Networks: General Kinetics. *Industrial and Engineering Chemistry Research* 36 (1997), pp. 3275–3281.

[26] Rota, R. *Fondamenti di Termodinamica dell'Ingegneria Chimica*. 2004.

[27] Salciccioli, M. et al. A review of multiscale modeling of metal-catalyzed reactions: Mechanism development for complexity and emergent behavior. *Chemical Engineering Science* 66.19 (2011), pp. 4319–4355.

[28] Solsvik, J., Jakobsen, H. A. A numerical study of a two property catalyst/sorbent pellet design for the sorption-enhanced steam-methane reforming process: Modeling complexity and parameter sensitivity study. *Chemical Engineering Journal* 178 (2011), pp. 407–422.

[29] Thiele, E. W. Relation between catalytic activity and size of particle. *Industrial and Engineering Chemistry* 31.7 (1939), pp. 916–920.

[30] Troupel, M. A. *CFD study of the intra and inter particles transport phenomena in a fixed-bed reactor*. Worcester Polytechnic Institute, 2009.

[31] Veldsink, J. W. *A catalytically active, non-permselective membrane reactor for kinetically fast, strongly exothermic, heterogeneous reactions*. University of Twente, 1993.

[32] Veldsink, J. W. et al. The use of the dusty-gas model for the description of mass transport with chemical reaction in porous media. *Chemical Engineering Journal* 57 (1995), pp. 115–125.

[33] Yoshida, F., Y., M. *Industrial and Engineering Chemical Process Design and Development* 2.263 (1963).